Master degree (M. Sc.) in Engineering Physics
Scuola di Ingegneria Industriale e dell'Informazione
Politecnico di Milano

Years 2018-2019

POLITECNICO
MILANO 1863

Design and fabrication of an integrated photonic circuit for producing a maximally-entangled three-photon state.

Candidate: **Gouriou Clement**
Student id: *894410*

Supervisor: **Prof. Roberto Osellame**
Co-supervisors: **Dr. Andrea Crespi**
Dr. Giacomo Corrielli

December 6, 2019

Abstract

In this thesis we will present the work that has been done toward the implementation of an integrated photonic device, capable of generating maximally entangled three photon states. To achieve this goal, we make use of the femtosecond laser micromachining technology, widely used in the group of Roberto Osellame at the Physics Department in Politecnico di Milano, where this work was carried out.

Firstly, we will present an overview of the field of quantum computing in the restricted domain of the optical implementation, that will provide a useful background as well as the motivation behind this activity. We will then present the femtosecond laser micromachining process and its multiple application. After which we will describe the several setups used for fabricating and characterising the several prototype made during the thesis.

The last three chapters develop in detail the work performed for the development of the project. We will start by a theoretical description of the quantum operation we aim to implement. For the circuit design, we take inspiration from an other work of very recent publication (Varnava et al., 2008), which propose a scheme for the generation of 3-photons maximally entangled state in the polarisation basis. We further elaborate on this scheme by first introducing simplification in the circuit topology using photon path-encoding, and by extending the initial 3-photons maximally entangle state generation to an arbitrary number of photons. Then, we present the different steps followed to optimize and fabricate the optical circuit, and we detail our optimisation protocol. The final chapter will be devoted to the characterisation of the fabricated prototype, as well as the discussion around the issues encountered.

Sommario

In questo lavoro di tesi si presenta l'attività di realizzazione di un dispositivo fotonico integrato per la generazione di stati quantistici a tre fotoni massimamente *entangled*. La tecnica sperimentale impiegata per il raggiungimento di tale obbiettivo consiste nella microlavorazione di substrati vetrosi tramite laser a femtosecondi. Tale tecnica è ampiamente utilizzata nel gruppo guidato dal Dr. Roberto Osellame presso il Dipartimento di Fisica del Politecnico di Milano, dove questa attività di tesi è stata svolta.

Innanzitutto verrà presentata una panoramica generale sulla computazione quantistica, con particolare accento alle implementazioni ottiche, con lo scopo di spiegare le motivazioni di questa attività. Successivamente verrà presentata la tecnica di fabbricazione e le sue applicazioni, assieme ad una descrizione dei setup sperimentali utilizzati sia per la realizzazione dei dispositivi, che per la loro caratterizzazione.

I capitoli successivi sono dedicati alla discussione dell'attività sperimentale condotta durante lo sviluppo del progetto. Si parte dalla descrizione del dispositivo fotonico in oggetto e della sua funzionalità quantistica da un punto di vista teorico. Il punto di partenza è uno schema proposto in un articolo di recente pubblicazione (Varnava et al., 2008) per la generazione di entanglement a tre fotoni basato sui modi di polarizzazione. Verrà mostrato come questo schema possa essere ulteriormente semplificato, generalizzato ad un numero arbitrario di fotoni, e tradotto nella codifica di modi spaziali. Verrà poi discussa l'implementazione sperimentale del dispositivo proposto e la sua ottimizzazione. Infine, verranno mostrate tutte le caratterizzazioni eseguite sui prototipi realizzati, assieme ad una descrizione delle problematiche incontrate.

Contents

List of Figures

Chapter 1

Entangled states in quantum information

Contents

Introduction

Quantum information processing has been an active field of research in the past three decades, and is still getting a large amount of investment. Indeed, this field holds many promises such as efficient quantum simulation [16],

fast search algorithm [39], polynomial factorisation [99] and fraud-fee cryptography [7] among others. For a rather complete overview on quantum algorithms, see Ref [72]. As its classical counterpart, the information in a quantum computer is stored in quantum bits, a.k.a. qubits, and is processed by mean of quantum gates. Although quantum computers outperform the classical ones in specific algorithms, we should emphasise that they do not aim to replace them but instead exploit their synergy. Very recently, quantum supremacy was demonstrated in the superconducting platform [4], using a quantum processor of 53 coherent qubits. This proof of concept is however restricted to an algorithm that has no practical application and have low fidelity. It contrast with the theoretical minimum number of qubits for implementing the Shor algorithm, which would require thousands of qubits, not accounting for error correction. Nonetheless, theoretical breakthroughs let the community be confident about the feasibility of this revolutionary technology. For instance, it has been demonstrated that a minimal set of two gate types - one-qubit and two-qubit gates - are needed for universal quantum computing [5]. Likewise, quantum error correction [60] lead to the demonstration of fault-tolerant quantum computers, at a cost of a coherence time threshold for qubits. Still, as long as quantum error correction has not been experimentally achieved, conjectures such as the extended Church Turing [1] challenge the whole enterprise. Consequently, most of the effort in this field has been to attain this threshold experimentally by designing qubits and gates with low decoherence, while in the mean time lower the threshold theoretically by improving error correction schemes.

[1] The extended Church Turing conjecture states there always exist an algorithm that simulate any physical system using statistical and classic computers.

There is a great number of explored ways to physically implement qubits and quantum gates. Among them, superconducting [59], trapped-ions [15] and linear optic [58] platforms are the front-runners. Each of them have their pros & cons, in term of quantum coherence life-time, scalability and interaction, crucial to implement two-qubit gates. Over the past decades, all three approaches show promising results, and the final architecture is likely to be an hybrid version of multiple approaches.

Concerning this thesis work, we follow the linear optics approach where qubits are encoded using quantum states of light. Photons are lowly coupled to the environment, retain their coherence for long periods [2] and travel fast. This

[2] Stability against thermal decoherence scales up to 11.5×10^9yr, which is the time for light to retain its polarization from its emission at Lyman-α blob LAB-1 to its arrival in earth.

makes them ideal for quantum communication applications [32] but the difficulty to realize photon-photon interactions poses serious challenges to realize deterministic photonic two-qubit gates. Nevertheless, the coherence properties of photons make the photonic platform appealing for quantum computing. Within that platform, several architectures are explored. Among them: quantum circuit/network, adiabatic quantum computers, quantum Turing machine and the measurement-based quantum computer (MQC). The latter being popular in the linear optics approach.

In the following sections we will focus on introducing the linear optical quantum computing (LOQC) approach, while having a quick remainder on the formalism that is used in this domain. A complete description of quantum computation and quantum information can be found in Ref [75]. Then I will describe the working principle of the most recently pursued architecture for LOQC computers. This first chapter aim to answer some fundamental questions: How light is processed in LOQC? What are the current challenges that LOQC is facing? How current architecture for LOQC systems differs from matter-based ones? What are the important concepts in use for LOQC? How is it related to the subject of this thesis?

1.1 Circuit-based architecture for quantum computing

The circuit-based approach is very similar to how classical computers works: an input state, saved on a register of qubits, is processed by an ordered sequence of logic gates after which the resulting state is measured in the output register. Although more commonly developed in matter-based platform, this architecture is compatible with the photonic approach. The complexity of this architecture arises from the realization of the intricate quantum gates operations while keeping the coherence of the qubits along the computation process.

1.1.1 Need for qubits

The most standard encoding of quantum information is using qubits. A qubit is a two-level quantum system that can

be represented by a vector in a two dimensional Hilbert space. In the Dirac braket notation, the two state of a qubit are represented by: $|0\rangle_L$, $|1\rangle_L$ [3]. Mathematically it is a system that holds a $SU(2)$ symmetry, which is isomorphic to a sphere $S(3)$.

[3] The subscript L, standing for *L*ogical, is used to refer as the computational basis as we foresee possible confusion when we will introduce the Fock states basis of photon number 0 and 1.

Representation of a qubit: the Bloch sphere

In the computational basis, any single-qubit state can be represented by the state,

$$|\psi\rangle = \alpha\,|0\rangle_L + \beta\,|1\rangle_L\,, \tag{1.1}$$

where α, β are complex scalars such that $|\alpha|^2 + |\beta|^2 = 1$ due to the normalisation principle. Up to a global phase, the qubit state can be equivalently expressed by,

$$|\psi\rangle = \cos\frac{\theta}{2}\,|0\rangle_L + e^{i\varphi}\sin\frac{\theta}{2}\,|1\rangle_L\,. \tag{1.2}$$

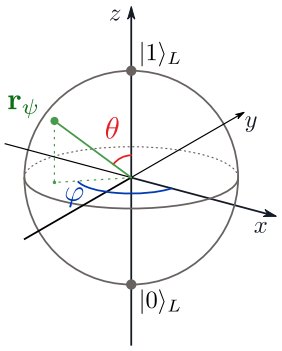

Figure 1.1: Bloch sphere representation of a qubit state.

The state can be represented by a vector, $\mathbf{r}_\psi$, on a sphere, also known as the Bloch sphere. By convention the poles of the sphere are along the z-axis, and represent the two computational states, $|0\rangle_L$ and $|1\rangle_L$ see Fig 1.1.

Operations on the qubit state can be understood as rotations in the Bloch sphere. It is then best to switch to the density representation of a qubit state to highlight the properties of those operations. The density matrix associated to a pure qubit state $|\psi\rangle$ is,

$$\rho \triangleq |\psi\rangle\langle\psi|\,, \tag{1.3}$$

$$= \begin{pmatrix} \cos^2\frac{\theta}{2} & e^{-i\varphi}\cos\frac{\theta}{2}\sin\frac{\theta}{2} \\ e^{i\varphi}\cos\frac{\theta}{2}\sin\frac{\theta}{2} & \sin^2\frac{\theta}{2} \end{pmatrix}, \tag{1.4}$$

$$= \frac{1}{2}\left(\hat{\mathbb{1}} + \mathbf{r}_\psi\hat{\sigma}\right), \tag{1.5}$$

where $\mathbb{1}$ is the identity operator, and $\hat{\sigma}$ is the zero-trace Pauli matrices vector. The latter is defined with respect to the unit vectors of the 3D sphere such that, $\hat{\sigma} = \hat{\sigma}_x\mathbf{u}_x + \hat{\sigma}_y\mathbf{u}_y + \hat{\sigma}_z\mathbf{u}_z$ with,c

$$\hat{\sigma}_x = \begin{pmatrix} 0 & 1 \\ 1 & 0 \end{pmatrix} \quad , \quad \hat{\sigma}_y = \begin{pmatrix} 0 & -i \\ i & 0 \end{pmatrix} \quad , \quad \hat{\sigma}_z = \begin{pmatrix} 1 & 0 \\ 0 & -1 \end{pmatrix}. \tag{1.6}$$

Introducing the operator, $\hat{R}_j(\alpha) = e^{i\frac{\alpha}{2}\hat{\sigma}_j}$, one can deduce this is the rotation operator around axis $j = x, y, z$, of angle

α. Indeed, using the matrix relations, $\hat{\sigma}_j^2 = -i\hat{\sigma}_x\hat{\sigma}_y\hat{\sigma}_z = \mathbb{1}$, for $j = x, y, z$, and the lemma: if an operator, $\hat{A}$, as the property $\hat{A}^2 = \mathbb{1}$ then we have $e^{i\theta\,\hat{A}} = \cos\theta\mathbb{1} + i\sin\theta\hat{A}$. From those relations, one can compute for instance $\rho' = \hat{R}_z(\theta)\rho\hat{R}_z^\dagger(\theta) = 1/2(\mathbb{1} + \mathbf{r}'_\psi\vec{\hat{\sigma}})$. Finally we show that,

$$\mathbf{r}'_\psi = \begin{pmatrix} \cos\theta & -\sin\theta & 0 \\ \sin\theta & \cos\theta & 0 \\ 0 & 0 & 1 \end{pmatrix} \mathbf{r}_\psi$$

which is a rotation of θ around the z-axis. Likwise for the other operators.

Physical implementation

We have seen how qubit states can be represented in the computational basis, $|0\rangle_L$, $|1\rangle_L$, but we still need a physical system that can support them. In regard to photonic implementation, there are many properties of light that can be exploited, some being: propagation mode in a fiber, angular momentum, time-bin, Fock state, polarization. However, not all are adapted for quantum computation. As an example, the vector space of time-bin encoding does not posses the natural symmetries of $SU(2)$ [58], that is to say realizing single qubit operation is difficult. The two most practical encoding fall into the so-called *dual-rail* encoding, as it make use of two distinct optical modes. This encoding is usually bear by *polarization* or *spatial* modes, although other more exotic degrees of freedom can be explored. The former uses the orthogonal linear polarization to encode the information: $|0,1\rangle_L = |V,H\rangle$, where V, H refer to the vertical and horizontal polarisation, respectively. While the latter uses two separated spatial modes, where one photon is in one of them: $|0\rangle_L = |0\rangle_a \otimes |1\rangle_b$ and $|1\rangle_L = |1\rangle_a \otimes |0\rangle_b$, where the subscript a, b refer to the two spatial modes (different waveguides for instance). The two encodings can vary depending on the convention in use but are mathematically equivalent - one can pass from polarization to spatial encoding using simple linear optical elements such as waveplates, beam splitters and polarizing beam splitters.

1.1.2 Need for gate operation

Universal quantum computing can be achieve by a minimal set of one- and two-qubits gates [5]. We already showed that one can imprint any state on the qubit by means of multiple rotations, using the Euler representation for instance: $\hat{U}(\alpha,\beta,\gamma) = \hat{R}_x(\gamma)\hat{R}_z(\beta)\hat{R}_x(\alpha)$. This constitutes a one-qubit gate. Such class of transformations can be built using beam-splitters, wave plates and phase shifters depending on the encoding in use.

On the other hand, it is not possible to use linear components to implement deterministic two-qubits gates. Let us illustrate this property by trying to obtain the Bell state $1/\sqrt{2}(|01\rangle_L + |10\rangle_L)$ from an initial two qubit state $|00\rangle_L$. If one uses only linear operations, that is transformation that only generate a superposition of the basis states, we can write the transformation of the qubit in the initial 0-state as,

$$|0\rangle_L \rightarrow \alpha_i |0\rangle_L + \beta_i |1\rangle_L , \tag{1.7}$$

with α_i and β_i complex numbers associated to the qubit $i = 1, 2$. Doing so to the two-qubits state, we get the two conditions on the coefficients:

$$\alpha_1\alpha_2 = \beta_1\beta_2 = 0 \qquad \text{and} \qquad \begin{cases} \alpha_1\beta_2 \neq 0 \\ \beta_1\beta_2 \neq 0 \end{cases} . \tag{1.8}$$

There is not combination of coefficients that satisfy both conditions.

In matter-based platforms, there exist several non-linear components allowing for two-qubits gate operation (*e.g.* Josephson junction in superconducting qubits). Concerning optical implementation of quantum computers, one can use non-linear effects arising from light-matter interaction. Using Kerr non-linearities, it is possible to induce a phase shift in one mode conditioned by the presence of a photon in an other mode. Those Kerr-based gates [71] have been demonstrated as proof of concept, but the interaction of this kind being very weak in the single-photon regime, there are still challenges to overcome in order to implement them in practical architectures. In the following sections we will present the main ideas to circumvent the need for non-linearities in the linear optical approach.

Hadamard gate

We will now present some examples of quantum gates, starting with the Hadamard one. It is often convenient to represent the gate action in the qubit basis. The Hadamard gate is important as it allows the superposition of well defined basis states, and the retrieval of the basis states from a balanced superposition. From the truth table one get,

$$H|0\rangle_L = \frac{1}{\sqrt{2}}(|0\rangle_L + |1\rangle_L) \tag{1.9}$$

$$H|1\rangle_L = \frac{1}{\sqrt{2}}(|0\rangle_L - |1\rangle_L) \tag{1.10}$$

$$H = \frac{1}{\sqrt{2}}\begin{pmatrix} 1 & 1 \\ 1 & -1 \end{pmatrix}, \tag{1.11}$$

and thus $H\frac{1}{\sqrt{2}}(|0\rangle_L + |1\rangle_L) = |0\rangle_L$.

$\frac{\pi}{8}$ phase-shift gate

This one-qubit gate introduces a relative phase between the two states of the qubit.

$$R = \begin{pmatrix} 1 & 0 \\ 0 & e^{i\frac{\pi}{4}} \end{pmatrix} = e^{i\frac{\pi}{8}}\begin{pmatrix} e^{-i\frac{\pi}{8}} & 0 \\ 0 & e^{i\frac{\pi}{8}} \end{pmatrix} \tag{1.12}$$

Which can be simply implemented using phase shifters in the path-encoding and birefringent element in polarisation.

Controlled-NOT gate

The Controlled-NOT gate, or CNOT gate, is a two-qubit gate that flips the state of a *target* qubit, conditioned by the state of a *control* qubit. Similarly to the single-qubit state, see eq (1.1), in the two-qubit basis, the state of the system is represented by a vector of four elements,

$$|\psi\rangle = \alpha|00\rangle_L + \beta|01\rangle_L + \gamma|10\rangle_L + \delta|11\rangle_L \equiv \begin{pmatrix} \alpha \\ \beta \\ \gamma \\ \delta \end{pmatrix} \tag{1.13}$$

The action of the gate is then given by,

$$\text{CNOT} = \begin{pmatrix} 1 & 0 & 0 & 0 \\ 0 & 1 & 0 & 0 \\ 0 & 0 & 0 & 1 \\ 0 & 0 & 1 & 0 \end{pmatrix}. \tag{1.14}$$

CZ-gate

Another important two-qubit gate is the controlled sign-flip gate, also CZ-gate, that is used in cluster state fabrication and processing protocol. Its representation is,

$$\text{CZ} = \begin{pmatrix} 1 & 0 & 0 & 0 \\ 0 & 1 & 0 & 0 \\ 0 & 0 & 1 & 0 \\ 0 & 0 & 0 & -1 \end{pmatrix}. \tag{1.15}$$

The CZ and the CNOT gate are equivalent as one can transform one to the other using local operations on each individual qubits, *e.g.* with the Hadamard gate. The CZ gate is also an important gate that is involved in the description of cluster states.

1.2 The One-Way Quantum Computer

In 2001, Raussendorf and Briegel introduced the field of quantum computing with a new paradigm: the one-way quantum computer [87, 88]. This measurement-based architecture relies on the cluster state [12], a multi-qubits maximally entangled state. The implementation complexity for the computational part is greatly reduced in this approach, since algorithms are *imprinted* on the cluster state by a sequence of single qubit measurement. However, the difficulty in building those kind of quantum computer, stems from the generation such cluster states.

Initially devised for matter-based platform (trapped-ion), this scheme has attracted a lot of interest and is now considered as the state of the art approach for the optical quantum computation approach. Indeed improvement were made from the initial idea, making the approach robust to photon losses [108], alternatively, using surface code for error

correction [30, 89]. Furthermore, this architecture is predicted to be realisable even without the need for quantum memory elements, which implementation is nowadays still challenging from the technological point of view.

1.2.1 Cluster states

A cluster state is a highly entangled multi-particle quantum state. However not all such states can be used for universal computation. The subset of cluster states used in universal one-way computation are the *graph states* [43]. A graph state is a multi-particle entangled state corresponding to a mathematical graph. Formally a graph $G = (V, E)$is a collection of vertices $V \in \mathbb{N}$, which are played by spin-like systems, or qubits, associated to a description of how those vertices are connected by edges $E \subseteq [V]^2$, which are similar to Ising-like interactions. Those states are also the building blocks for various error correcting codes [96].

Formally a graph state $|G\rangle$ is a pure quantum state on the Hilbert space $\mathcal{H}_V = (\mathbb{C}^2)^{\otimes V}$. Given a graph $G = (V, E)$ and considering a vertex, a, with its set of neighbours, N_a, *i.e.* all other vertices connected to a by an edge, we define the hermitian correlation operator $\hat{K}_G^{(a)} \triangleq \hat{\sigma}_x^{(a)} \bigotimes_{b \in N_a} \hat{\sigma}_z^{(b)}$. Thus a graph state $|G\rangle$ is the common eigenvector of all the vertex operator,

$$\forall a,\ \hat{K}_G^{(a)} |G\rangle = \pm |G\rangle \,. \tag{1.16}$$

In other word, $|G\rangle$ is a fixed point of the correlation operators, and one can choose by convention the eigenvalue $+1$. Alternatively, starting from the empty graph, $|\text{empty}\rangle = |x, +\rangle^{\otimes V}$, a set of disconnected vertices all in the Bell state $|x, +\rangle = 1/\sqrt{2}\ (|0\rangle + |1\rangle)$, we can build up the graph state by making the connection between vertices. We define the connection operator [4] between vertex a and b,

[4] Note that $U^{(a,b)}$ is the sign-flip two-qubit gate, also known as the CZ-gate.

$$U^{(a,b)} = P_{z,+}^{(a)} \otimes \mathbb{1}^{(b)} + P_{z,-}^{(a)} \otimes \sigma_z^{(b)} = \begin{pmatrix} 1 & 0 & 0 & 0 \\ 0 & 1 & 0 & 0 \\ 0 & 0 & 1 & 0 \\ 0 & 0 & 0 & -1 \end{pmatrix}, \tag{1.17}$$

where

$$P_{z,\pm}^{(a)} = \frac{\mathbb{1} \pm \sigma_z^{(a)}}{2}, \tag{1.18}$$

and the graph state is finally given by

$$|G\rangle = \bigotimes_{(a,b)\in E)} U^{(a,b)} |\text{empty}\rangle . \tag{1.19}$$

All in all, a cluster state is a complicated graph state that allows quantum information processing. It has been shown that two-qubits gate can be implemented with cluster states of dimensionality greater or equal to 2[74]. Fault-tolerant architectures make use of 3D clusters [90], using redundant encoding.

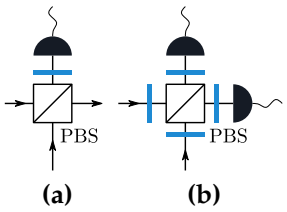

Figure 1.2: Fusion gates type I (a), and type II (b) for polarisation qubit encoding. Those gates are used to perform Bell-measurement and connect vertices in optically implemented graph states.

1.2.2 Growing a cluster

As mentioned before, the generation of cluster state is an intricate problem. The main challenge in the different platforms for quantum computing is then to grow efficiently a 3D cluster. A full description can be found in Ref [61], as we will summarize the approach.

Building a cluster state boils down to entangle many qubits together. In graph states, edges represent entanglement between qubits but two-qubit entanglement are achieved using two-qubit gates. When connecting vertices together, it is then important that the cost of failure does not overcome the rate of success. Using *micro-cluster* [76], Nielsen demonstrated than any two-qubit gate with arbitrary success probability, p, can be used to make cluster states. On the other hand, the lower p is, the bigger the starting micro-cluster must be.

Following the reasoning in Ref [6], suppose we already have a cluster of n vertex and want to increase its size. We look forward to attach a chain of size m, *i.e.* a graph state of m vertices, using a connection operation with a success probability of p. In the process we lose n_s qubits of the original cluster if the operation is successful, but we lose

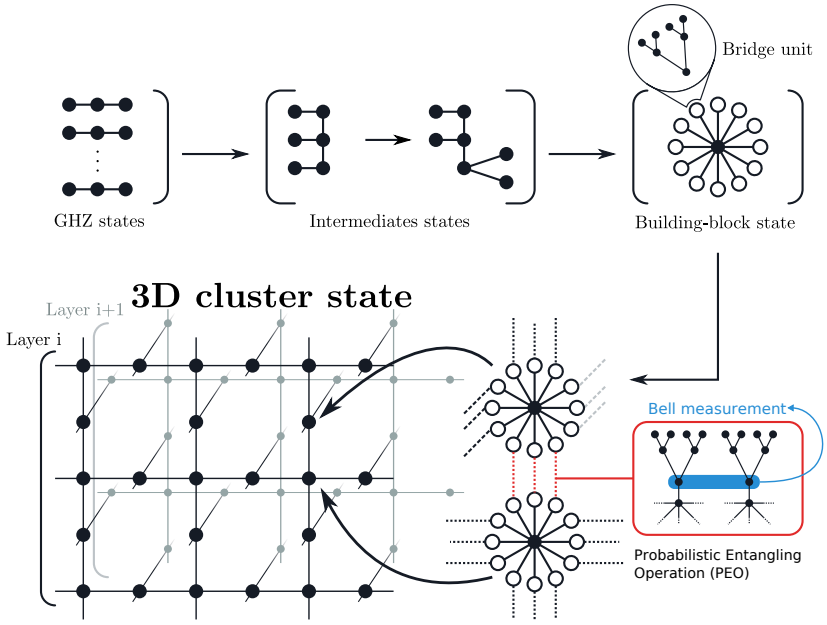

Figure 1.3: Synthesis of a 3D cluster state, redrawn from Ref [61]. Starting from several GHZ states, a series of Bell measurements connect them into an intermediary state that will be used for the building-block graph state. This tree-like state has several branches allowing to connect the central qubit to others following the edges pattern of the wanted cluster state that can be a 3D lattice. The repetition account for possible failure in the connection operation.

n_f qubits if it fails. Thus to observe a positive growth we need,

$$p(n+m-n_s)+(1-p)(n-n_f) > N \quad \Leftrightarrow \quad m > \frac{pn_s+(1-p)n_f}{p}. \tag{1.20}$$

Brown and Rudolph introduced type-I and type-II fusion gates [14], in order to perform vertex connection operation in optical quantum computing. Although both type of gates can be used, the failure cost of type-I is greater. Using redundant encoding, it is possible to only use type-II fusion gate to grow clusters. Successful type-II fusion gates operate a *Bell measurement* [5] on the two qubits involved. Under this strategy we have $p = 1/2$, $n_s = 2$, $n_f = 1$, and the minimal size of the added chain must be $m \geq 3$.

As a result, it has been shown that the minimal graph state that allows the growth of any cluster state is the *3-qubit maximally entangled state*, also known as the *Greenberger-Horne-Zeilinger (GHZ)* state [6]. Although not sufficiently complex to directly be the building blocks of universal cluster states, GHZ graph states are the fundamental resource to build the needed building-block graph states. Without

[5] A Bell measurement is a projective measurement of a generic two-qubit state in the maximally entangled Bell state basis.

[6] The GHZ state is a quantum state that can be seen as the generalisation to three qubits of the two qubits Bell state $|\Psi\rangle = 1/\sqrt{2}(|00\rangle + |11\rangle)$, and will be further introduce in sec. 1.4.

going into the detail, Fig 1.3 summarizes the full scheme for building arbitrary cluster states from initial GHZ states.

1.2.3 Principles of one-way quantum computation

To simplify the description, we illustrate the functioning principles on a 2D cluster state, see Fig 1.4, based on Ref [13, 87, 88].

As explained previously, information in one-way quantum computers is processed by a sequence of one-qubit measurements. In the graph representation, the quantum information is carried along one axis (often defined as the time axis), while the measurements occur along the others. There are five principle that demonstrate the functioning of the architecture:

(a) Since the linked vertices are entangled, information encoding in one qubit is delocalised along the paths made by the connections. It is thus possible to teleport and propagate information using a string of five-connected qubits.

(b) Any arbitrary rotation operation, *i.e.* one-qubit gate, can be achieved using a sequence of measurement on a five long qubit string.

(c) Two-qubit gates needs to use vertical connections, *i.e.* not in the time direction, see in Fig 1.4.

(d) Single step and multi-step measurement are both equivalent. In addition, the randomness of the results in the measurements is integrated in the scheme, as the next sequence of measurements can account for the result of the previous one to correct any phase shifting. This implies the time-ordering of the sequence of measurement.

(e) There is no need for having specific input qubits. Indeed, if we know the initial state of the cluster vertices (usually the $|+\rangle$ of the Bell state in x-axis), we can prepare the starting qubits in any states using (a).

Since the information circulates in one direction, flowing through the link between vertices of the cluster state, the connectivity of the cluster is related to a percolation problem. Depending on the topology of the cluster graph state,

the percolation threshold gives the scalability potential for the architecture.

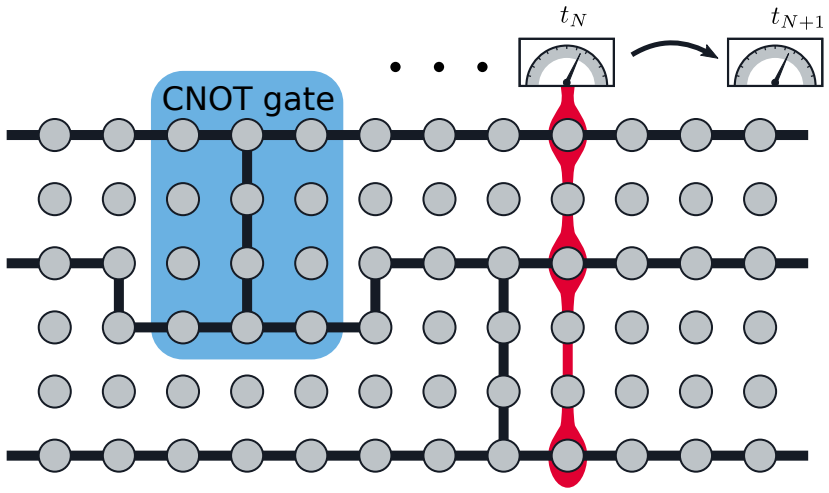

Figure 1.4: Example of a 2D cluster processing. Each circle represent a qubit, and each black line a entanglement connection. In the blue square is shown a connection configuration that implements a CNOT gate. The information is processed along the time direction from left to right by several single qubits measurement (red highlighted) and the information is given for the following measurement. Redrawn from Ref [13].

The most remarkable consequence of the one-way computation scheme, is that the cluster state does not depends on the algorithm to be implemented. Making it a universal resource state, while the computation power of the architecture depends on its size.

1.2.4 Current implementation, the limits

The one-way quantum computer was initially though to be implemented in matter-based platform. There are already examples of such implementation in the superconducting platform [117], as well as the generation of cluster states: superconducting qubits [104], using quantum dots [10, 116].

The optical implementation of the one-way quantum computer requires sophisticated tools that are still under development, such as single photon sources, number resolving detectors, low loss optical elements and high fidelity qubit gates. Not only one needs to consider the probabilistic success of two-qubit gates, but also photon loss and thermal noises for the phases.

Another important feature about the one-way architecture is that even though the generation of entangled qubits is probabilistic in the LOQC approach, once the cluster state is prepared, all the computation is deterministic. There has been already experimental proof of concept of this architecture, where clusters state up to six photons has been demonstrated [54, 64] and used for simulating quantum gates [113].

1.3 Quantum Computing with Photons

Linear optical quantum computing (LOQC) makes use of photons as carriers of quantum information. In order to manipulate the light state, passive components are used: beam splitters, phase-shifters, half-wave plates and quarter-wave plates. They are the building blocks for LOQC systems. As mentioned before it is not possible to make two-qubit gates using only linear components. The use of measurement as a source of non-linearity was introduced to overcome this issue, but the resource in terms of photon to counter-balance the probabilistic losses made the method not scalable.

Not until Knill, Laflamme and Milburn proposed a new efficient scheme [57] that make use of a *teleportation trick* [36], rendering LOQC a feasible approach. Since then, new architectures emerged, and less resource demanding alternative were developed. The leading approach in LOQC systems being the measurement-based quantum computing (MQC), represented by the one-way quantum computer.

1.3.1 Quick reminder on quantum optics

Representation of a photon mode

From any textbook [112], one can find the basic premises used in this section. Thus starting from the quantization of the electromagnetic field, it results that light-radiation can be expressed in terms of annihilation and creation operators, $\hat{a}_j(k)$ and $\hat{a}_j(k)^\dagger$ respectively, where $j = 1, 2$ denotes the two orthogonal types of polarization due to the Coulomb gauge choice, and $k = |\mathbf{k}|$ is the modulus of the considered radiation wave-vector, also called momentum or mode. We

omitted the consideration of squeezed states of light for simplification.

For clarity, we will omit the dependency on the polarization and momentum when there will be no confusion. Likewise concerning the operator hat. The annihilation and creation operators are defined by their specific action on the Fock states, $|n\rangle$, and their canonical commutation relations,

$$\hat{a}\,|n\rangle = \sqrt{n}\,|n-1\rangle \quad [\hat{a}_i(k),\, \hat{a}_j^\dagger(k')] = \delta(k-k')\delta i, j \tag{1.21}$$

$$\hat{a}^\dagger\,|n\rangle = \sqrt{n+1}\,|n+1\rangle \quad [\,\hat{a}_i(k),\, \hat{a}_j(k')] = [\hat{a}_i^\dagger(k),\, \hat{a}_j^\dagger(k')] = 0 \tag{1.22}$$

A Fock state is a identical non-interacting multi-particle state, which describe the number of such particle in a given mode. Fock states define a complete basis to describe any state of light. The annihilation and creation operators act directly on the Fock states, as they remove or add a particle in the given mode, respectively.

We introduce the number operator, $\hat{n} = \hat{a}^\dagger\hat{a}$, of which the Fock state are by definition its eigenvectors: $\hat{n}\,|n\rangle = n\,|n\rangle$, with n is the number of photon in the state mode $|n\rangle$.

We raise the attention on the absence of the subscript L in the kets, refering to the Fock state and not the state of logical qubits.

What does linear optic mean?

In quantum mechanics, one can treat the evolution of a system using different pictures: the Schrödinger picture, the Heisenberg one and the interaction picture. In the following we will use the Heisenberg picture where the evolution of a system is given by the evolution of the operator acting on the system state. We will thus express the action of the fundamental components in LOQC as how they act on the operators of the optical states.

Let us consider a single mode state[7], $|\psi\rangle_{\text{in}} = \left(\sum_j^\infty c_j \hat{a}_{\text{in}}^\dagger\right)|0\rangle$, entering an optical system. It is possible to desribe the action of the system only by considering the action performed on the creation-annihilation operators. The output state is then given by, $|\psi\rangle_{\text{out}} = \left(\sum_j^\infty c'_j \hat{a}_{\text{out}}^\dagger\right)|0\rangle$.

[7] Light state of one define frequency, and one polarisation.

The term *linear optic* denotes elements whose Hamiltonian is bilinear in terms of creation-annihilation operators,

i.e. in the form of $H = \sum_{i,j} m_{i,j} \hat{a}_i^\dagger \hat{a}_j$ with $m_{i,j}$ a complex-valued coefficient. Such Hamiltonian H commutes with the total number operator, meaning that the optical element is lossless. The optical component can thus be represented by the matrix M of coefficients $m_{i,j}$. Moreover, any combination of optical elements only acts on the matrix M, but does not introduce higher order terms in creation-annihilation operators. For more detail, see Ref [58].

(a) Phase shifter

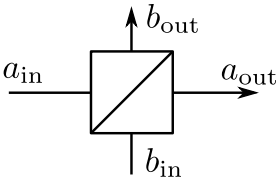

(b) Beam Splitter

Figure 1.5: Schematic of a phase shifter (a) and a beam splitter (b).

1.3.2 Mathematical description of components

We can now use the matrix formalism to express the action of optical components in the creation-annihilation basis of the considered optical system.

Phase shifters

A phase-shifters is a component that changes the phase of the electromagnetic field of a given mode. Its action is given by the Hamiltonian $H_\phi = \phi(t)\, \hat{a}_{\text{in}}^\dagger \hat{a}_{\text{in}}$, where we use the convention $\hbar = 1$. Then output mode transformation is,

$$\hat{a}_{\text{out}}^\dagger = \left(e^{i\phi(t)\, \hat{a}_{\text{in}}^\dagger \hat{a}_{\text{in}}}\right) \hat{a}_{\text{in}}^\dagger \left(e^{i\phi(t)\, \hat{a}_{\text{in}}^\dagger \hat{a}_{\text{in}}}\right)^\dagger = e^{i\phi(t)}\, \hat{a}_{\text{in}}^\dagger \tag{1.23}$$

Beam-splitters

The beam splitter is a passive element that mixes two modes together and distributes them in two outputs. We will only consider the lossless beam splitter scheme [119], and disregard the polarization - foreseeing that in this thesis we will only use path-encoded modes.

A beam splitter, see Fig 1.5b, transforms the input mode, $\hat{a}_{\text{in}}^\dagger, \hat{b}_{\text{in}}^\dagger$, as,

$$\hat{a}_{\text{out}}^\dagger = t\hat{a}_{\text{in}}^\dagger + r'\hat{b}_{\text{in}}^\dagger, \tag{1.24}$$
$$\hat{b}_{\text{out}}^\dagger = r\hat{a}_{\text{in}}^\dagger + t'\hat{b}_{\text{in}}^\dagger, \tag{1.25}$$

where, r, t, r', t' are complex scalars.

From the energy conservation and commutation rules (eq.(1.21) and (1.22)), one can parametrize the lossless beam splitter with θ, ϕ, such as $r = r' = \cos\theta$ and $t = -t^* = ie^{i\phi} \sin\theta$, where the relative phase ϕ ensures that the transformation is unitary. In the following we will deal meanly

with the balanced beam splitter, also known as 50:50 beam splitter, and choose the convention $\phi = 0$. It follows,

$$\hat{a}^\dagger_{\text{out}} = \frac{1}{\sqrt{2}}\left(\hat{a}^\dagger_{\text{in}} + i\hat{b}^\dagger_{\text{in}}\right), \qquad \hat{b}^\dagger_{\text{out}} = \frac{1}{\sqrt{2}}\left(i\hat{a}^\dagger_{\text{in}} + \hat{b}^\dagger_{\text{in}}\right). \tag{1.26}$$

With the operators as column vector, the matrix representation of a beam splitter is given by,

$$BS = \frac{1}{\sqrt{2}}\begin{pmatrix} 1 & -i \\ -i & 1 \end{pmatrix}. \tag{1.27}$$

1.3.3 Linear optical networks

It has been shown that any arbitrary quantum unitary operator acting on a discrete Hilbert space, can be modeled using a linear optical network made solely by beam-splitters, phase shifters and mirrors [91].

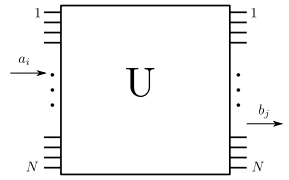

Figure 1.6: Linear optical network of N ports, represented by a matrix U.

Unitary representation

A linear optical network can be modeled in terms of its linear transformation over the creation-annihilation operators. The N-port optical network is represented by a $N \times N$ matrix U such that,

$$\hat{a}^\dagger_{\text{in},j} = \sum_{k=1}^{N} \mathrm{U}_{j,k}\hat{a}^\dagger_{\text{out},k}. \tag{1.28}$$

The network matrix is a complex-valued matrix and we write its coefficients $u_{i,j} = r_{i,j}e^{i\theta_{i,j}}$, where $r_{i,j}$ is the amplitude, while $\theta_{i,j}$ the phase of the complex coefficient.

The several ways to characterise a quantum optical network

In reality, the actual realisation of an optical circuit leads to variation from its theoretical design. It is then important to characterise how much the fabricated device differs from its ideal functioning, so as to correct the defects with tunable elements (*e.g.* tunable phase shifter to correct spurious phases added during fabrication).

There exist several techniques to characterise quantum operations and know as quantum process tomography (QPT) [50, 84]. Method using two-photon interference [] or

coherent quantum light state [], become rapidly inefficient with the growing complexity of the optical network.

In Ref [86], the authors use classical coherent light interference to measure the complex coefficient of a fully connected optical network. This technique has the advantage of being practical when dealing with photonic device of high number of modes. In terms of coherent state of light, the expression of the unitary operator is similar to the previously seen one. Since coherent light is by definition the eigenvector of the annihilation operator, $\hat{a}\,|\alpha\rangle = \alpha\,|\alpha\rangle$, where α is a complex scalar such that $|\alpha| = 1$. The output coherent state is thus given by,

$$\beta_j = \sum_{k=1}^{N} \mathrm{U}_{j,k}\alpha_k, \tag{1.29}$$

where $|\alpha_1, \ldots, \alpha_N\rangle$ and $|\beta_1, \ldots, \beta_N\rangle$ or the input and output coherent state, respectively.

Unitary representation of lossy optical networks

Introducing losses to an optical network render the process non conservative of the Hilbert space, and thus making the network matrix no longer unitary. Following the development in Ref [86], the network can still be describe by embedding the matrix U_{lossy} of the lossy network in a bigger unitary matrix, V, that account for the losses. While losses can always be modeled by a beam splitter connected to a virtual loss channel where the transmissivity of that channel is given by the power loss, there is no general method to determine the bigger matrix V. However, in the particular case of *path-independent* losses, V can be obtain straight forwardly.

For each channel, the beam-splitter that model the loss is,

$$S_j = \begin{pmatrix} \eta_j & -\sqrt{1-\eta_j^2} \\ \sqrt{1-\eta_j^2} & \eta_j \end{pmatrix}, \tag{1.30}$$

where $\eta_j \in [0, 1]$ is the beam-splitter transmissivity, *i.e.* the loss rate of the channel. We can estimate it with the insertion losses, $\eta_j = \sqrt{\frac{1}{I_{\text{in}}}\sum_k I_{\text{out},k}} = 10^{-\frac{IL_{dB}}{2}}$. We introduce the

total loss matrix,

$$S_{\text{tot}} = \begin{pmatrix} \boldsymbol{\eta} & -\tilde{\boldsymbol{\eta}} \\ \tilde{\boldsymbol{\eta}} & \boldsymbol{\eta} \end{pmatrix}, \tag{1.31}$$

with $\boldsymbol{\eta} = \text{diag}(\eta_1, \ldots, \eta_N)$ and $\tilde{\boldsymbol{\eta}} = \text{diag}(\sqrt{1-\eta_1^2}, \ldots, \sqrt{1-\eta_N^2}$. The general $N \times N$ lossy network matrix U_{lossy}, is then embedded in a larger $2N \times 2N$ unitary matrix V. The unitary matrix V is then given by,

$$V = S_{\text{tot}} \cdot \begin{pmatrix} U_{\text{no-loss}} & \mathbb{O} \\ \mathbb{O} & \mathbb{1} \end{pmatrix} = \begin{pmatrix} \boldsymbol{\eta} U_{\text{no-loss}} & -\tilde{\boldsymbol{\eta}} \\ \tilde{\boldsymbol{\eta}} U_{\text{no-loss}} & \boldsymbol{\eta} \end{pmatrix} = \begin{pmatrix} U_{\text{lossy}} & -\tilde{\boldsymbol{\eta}} \\ \tilde{\boldsymbol{\eta}} U_{\text{no-loss}} & \boldsymbol{\eta} \end{pmatrix}, \tag{1.32}$$

where $\mathbb{O}$, $\mathbb{1}$ and U_{noloss} are the null, identity and the lossless optical network matrices respectively. The real lossy network matrix, related to our design, is then given by,

$$U_{\text{lossy}} = \boldsymbol{\eta} \cdot U_{\text{no-loss}}. \tag{1.33}$$

1.3.4 Important concepts

Quantum mechanics is a vast subject already covered by a tremendous number of excellent textbooks. It might nonetheless be interesting to overview the important concepts that will be in use for this thesis work.

The theory of quantum mechanic states that a quantum system $|\psi\rangle$ is represented by a wave function, ψ, that can depend on many parameters. The dominant interpretation - Copenhagen interpretation - associate the wave function as a probability distribution. The particularity of the wave function is that it is complex-valued and normalised. The wave description of a quantum state, make interference phenomena possible, leading to a range of new phenomena such as single particle interference, photon bunching, quantum teleportation.

Mach-Zehnder interferometer

A Mach-Zehnder (MZ) interferometer is an interferometric device that separates incoming light in two path and allow to measure phase difference between the two paths, as depicted in Fig 1.7. In quantum optics, it is most interesting to study the effect of such interferometer in the single photon regime, *i.e.* with Fock states.

Figure 1.7: Mach-Zehnder interferometer schematic. The two input modes (a,b) are split and acquire a relative phase shift $\Delta\phi$ before being recombined and output in modes (c,d).

Mathematically the two modes $\hat{a}_a^\dagger$ and $\hat{a}_b^\dagger$ transform into $\hat{a}_c^\dagger$ and $\hat{a}_d^\dagger$, such that,

$$\begin{pmatrix} \hat{a}_c^\dagger \\ \hat{a}_d^\dagger \end{pmatrix} = BS^\dagger \cdot \begin{pmatrix} 1 & 0 \\ 0 & e^{i\varphi} \end{pmatrix} \cdot BS^\dagger \begin{pmatrix} \hat{a}_a^\dagger \\ \hat{a}_b^\dagger \end{pmatrix} \tag{1.34}$$

$$= ie^{i\frac{\varphi}{2}} \begin{pmatrix} -\sin\frac{\varphi}{2} & \cos\frac{\varphi}{2} \\ \cos\frac{\varphi}{2} & \sin\frac{\varphi}{2} \end{pmatrix} \begin{pmatrix} \hat{a}_a^\dagger \\ \hat{a}_b^\dagger \end{pmatrix} \tag{1.35}$$

$$\begin{pmatrix} \hat{a}_a^\dagger \\ \hat{a}_b^\dagger \end{pmatrix} = ie^{-i\frac{\varphi}{2}} \begin{pmatrix} \sin\frac{\varphi}{2} & \cos\frac{\varphi}{2} \\ \cos\frac{\varphi}{2} & -\sin\frac{\varphi}{2} \end{pmatrix} \begin{pmatrix} \hat{a}_c^\dagger \\ \hat{a}_d^\dagger \end{pmatrix} \tag{1.36}$$

Let a single photon inputs in mode a, the output state is given by,

$$|1\rangle_a |0\rangle_b = \hat{a}_a^\dagger |0\rangle_a |0\rangle_b \tag{1.37}$$

$$\downarrow$$

$$(\sin\frac{\varphi}{2}\hat{a}_c^\dagger + \cos\frac{\varphi}{2}\hat{a}_d^\dagger) |0\rangle_c |0\rangle_d = \sin\frac{\varphi}{2} |1\rangle_c |0\rangle_d + \cos\frac{\varphi}{2} |0\rangle_c |1\rangle_d \tag{1.38}$$

where we discarded the global phase.

We see that the photon self-interference in the MZ is constructive in channel c when the MZ is balanced (*i.e.* $\varphi = 0$), while destructive in the output channel d. The situation is reversed when $\varphi = \pi$.

Photon bunching

If we now consider two identical photon that input on two different channels of a beam splitter, we have,

$$|1\rangle_a |1\rangle_b = \hat{a}_a^\dagger \hat{a}_b^\dagger |00\rangle \tag{1.39}$$

$$\downarrow$$

$$\frac{1}{2}(\hat{a}_c^\dagger + i\hat{a}_d^\dagger)(i\hat{a}_c^\dagger + \hat{a}_d^\dagger) |00\rangle = \frac{i}{2}(\hat{a}_c^\dagger \hat{a}_c^\dagger + \hat{a}_d^\dagger \hat{a}_d^\dagger) |00\rangle \tag{1.40}$$

$$= \frac{i}{2}(|20\rangle + |02\rangle). \tag{1.41}$$

Surprisingly, we do not have a statistical superposition of two single photon splitting. The quantum state of having one photon in each output channel was suppressed due to destructive interference of the two identical photons. They come out together, in bunch. This is the *photon bunching*, also known as Hong-Ou-Mendel effect [46].

It is important to note that this happens only because the photons are identical, *i.e.* non distinguishable. The historical Hong-Ou-Mendel experiment [46], shows that introducing a delay between the two photon, thus making them distinguishable, we suppressed the bunching effect. The 2nd order correlation of the Hong-Ou-Mendel interferometer, is a direct characterisation of how close are the two photon to be identical, *i.e.* how well they wave function overlap. The shape of the 2nd order correlation versus delay being related to the power spectrum of each individual photon. It is then used to measurement how well a identical single photon source performs.

Projective vs indirect measurements and herald scheme

In the Copenhagen interpretation, one of the postulate that lies at the foundations of quantum mechanics states that the action of measuring a quantum system causes the collapse of the system wave function into one of the eigenstate of the measurement setup. This collapsing is yet not fully understood.

When a quantum system is directly measured, the initial state is projected on the measurement basis vectors, also called observables. This is called *projective measurement*. The downside is that the initial quantum system is greatly perturbed by the measurement, and any superposition of states is cancelled.

One can devise a scheme where, instead of measuring the system, a probe state is introduced so that it interacts with the unknown quantum system in such a way that measuring the probe will gives information on the interaction and thus gives information on the studied system. This general scheme is the *indirect measurement* The probe state, also called *ancilla* or *meter*, will endure a projective measurement. Consequently the system that is entangled with the ancilla will collapse in the corresponding state that was correlated with the measured ancilla state.

It is this indirect measurement scheme that is used in the so called *heralded gates*, as the ancilla measurement will herald the success or not of the gate operation.

1.4 Generation of GHZ state with photons: state of the art

There have been several protocols proposed to generate GHZ-state with photons, following different approaches: using direct generation by non-linear effect a parametric down conversion, or using probabilistic generation associated to post-selection or heralded scheme.

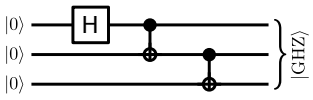

Figure 1.8: Quantum Logic Information protocol to generate a three qubits GHZ state. One can identify a succession of three quantum gates: the first one being the 1-qubit Hadamard gate, the latter two being 2-qubit CNOT gates.

1.4.1 The Greenberger-Horne-Zeilinger (GHZ) state

In the theoretical framework, one can define two distinct classes of equivalent three qubits entangled states [8]: the Greenberger-Horne-Zeilinger states [37] and the W states. In the qubit basis, the GHZ state is:

$$|\mathrm{GHZ}\rangle = \frac{1}{\sqrt{2}}\left(|000\rangle_L + |111\rangle_L\right). \tag{1.42}$$

In quantum information, the generation of such a state using qubits needs at least three quantum gates, see Fig 1.8. However, as explained in the introduction, linear optics does not allow to perform efficient two-qubit gates. Thus such circuit-based protocol are often discarded and other approaches are pursued.

The GHZ state has the intrinsic property of maximising the entanglement of its qubits [8] [31], as well as being robust to phase noise. This makes the state useful for many other application that just for cluster state growth.

GHZ states can be used in entanglement swapping protocols [80], leading to the development of quantum repeaters [11, 24].They are useful in the field of quantum communication and quantum cryptography [33]. In a more fundamental way, one can use GHZ states to disprove the 'elements of reality' advanced in the EPR paradox [38].

[8] Maximally entangled states are states that attain the maximum value in the Bell's inequality. As there is virtually an infinity of Bell's inequality, maximal entanglement is defined *w.r.t* the Bell-Klyshko inequality.

1.4.2 Direct generation

Spontaneous Parametric Downconversion (SPDC) is a well known method to produce pairs of entangled photons. It is often used as a single photon source, since the detection of

one of the photon in the pair heralds the necessary presence of the second photon in the optical apparatus.

Direct generation of GHZ three-photon state uses a cascaded version of the SPDC generation protocol [40, 48, 49], see Fig 1.9.

Using the SPDC technique, GHZ states up to ten photons have been experimentally demonstrated [47, 114]. However the efficiency is limited due to the weakness of the nonlinear effect needed in the downconversion. One of the highest detection rate of the entangled triplet is about seven GHZ states per hour [].

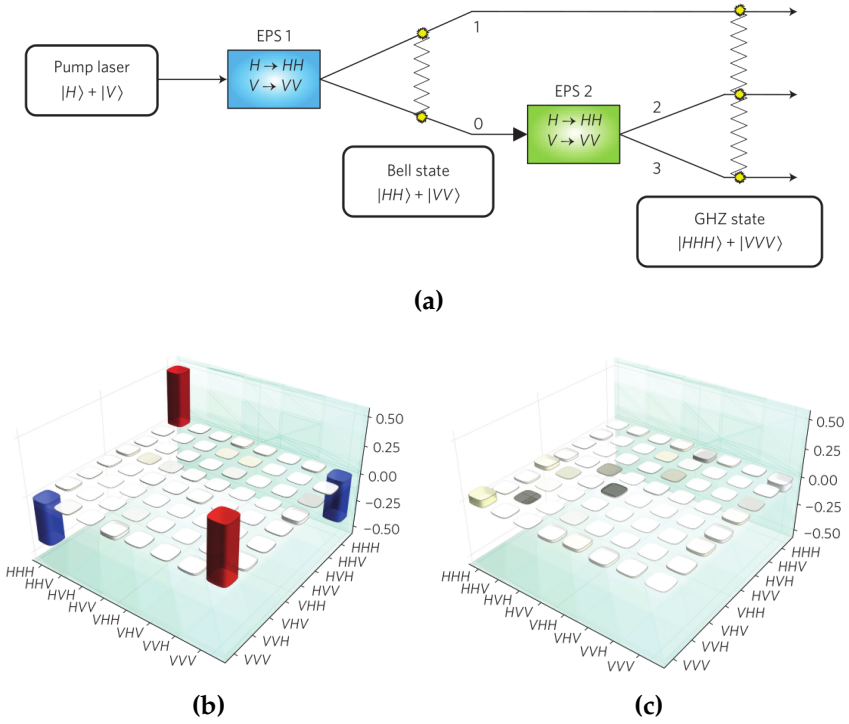

Figure 1.9: (a) Schematic of a cascaded SPDC leading to the direct generation of a three entangled photons in a GHZ state for polarization encoding. In the experiment, they make use of a periodically poled potassium titanyl phosphate (PPKTP) crystal in EPS1 for the first generation of entangle photon pair, then they use periodically poled lithium niobate (PPLN) waveguides in EPS2 to generate the GHZ state. (b) and (c) show the reconstructed density matrix coefficients real and imaginary, respectively. Figures from Ref [40].

1.4.3 Probabilistic generation of GHZ state: using linear optics

Generation of a maximally entangle multi-photon state can be achieve using linear optical elements associated with appropriate measurement protocol.

Efficient protocols to generate maximally entangled photon states are already available in polarization [109], and a similar schematic in path-encoding [61]. There are already several experimental demonstration of generation of GHZ state in polarization [107]

However, most of the protocol and almost all experimental demonstration are made using bulk optics [107]. Some design account for lithographic techniques [9], but relies on bulk parametric sources.

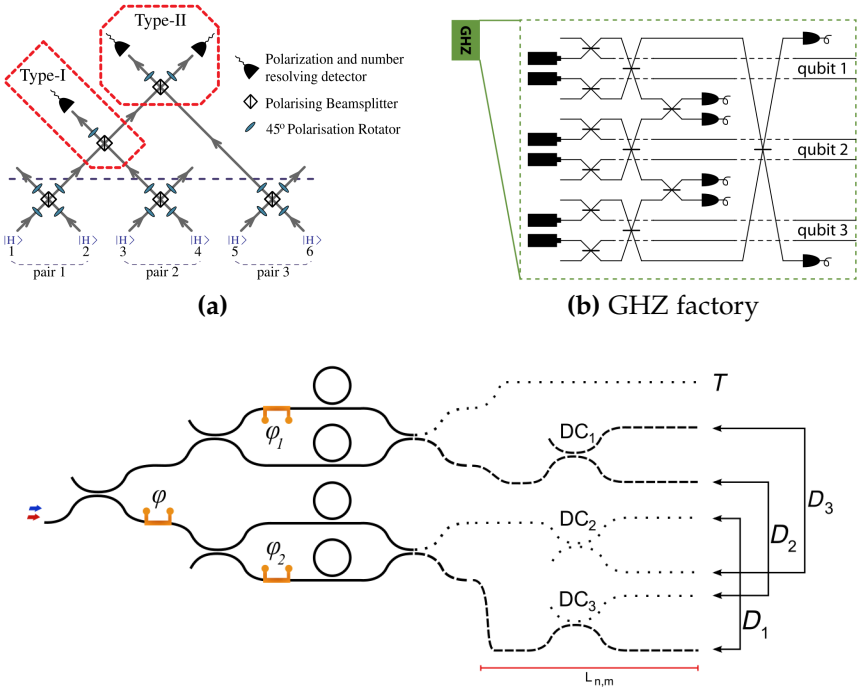

(a) **(b)** GHZ factory

(c)

Figure 1.10: Example of optical implementation for Greenberger-Horne-Zeilinger state generation using polarization encoding (a) or path encoding (b,c). In (a) and (b) use only six identical single photons. The photons are injected in the square box on the left of the design and suffer several beam splitting, while the detectors allow the heralding for the success of the GHZ generation. Scheme in (c) uses a pair of photon generated by spontaneous parametric conversion. Figures (a), (b), (c) from [9, 61, 109] respectively.

In this thesis, we will later present our version of the path-encoded GHZ factory directly translated from the scheme in Fig 1.10a.

Chapter 2

Femtosecond Laser Micromachining

Contents

Introduction

Since Hirao's group first explored femtosecond laser to produce permanent change in transparent dielectric as a new tool for integrated optics in 1996 [22], the variety of application increased tremendously ranging from astrophotonics to integrated quantum optics [69]. The technology uses the non-linear effects induced by TW/cm^2 intensities focused in a micro-scale volume to produce a modification of the refractive index. By continuously translating the focal

point inside the sample, one manages to produces waveguides. Contrary to the lithographic process, femtosecond laser micromachining (FLM) does not require a clean-room facility to be carried out. It is a single-step maskless process which allows 3D writing, but in a limited range in the depth direction [63]. This technique is convenient for rapid circuit prototyping that uses complex geometries in waveguide networks. It has been shown that ultrafast laser irradiation can be used to modify locally the selectivity of chemical etching of glasses, e.g. using hydrofluoridric acid or potassium hydroxide. This enables the creation of buried microchannels integrated within laser-written photonic circuits, which find multiple applications in the field of micro-fluidics. This is especially true for fused-silica [65]. This demonstrates the versatility FLM, in term of material processing (glass, crystals, transparent polymers) as well as the combination of those techniques (*e.g.* lab-on-chip [110, 118]).

2.1 Permanent modification of dielectrics with femtosecond laser irradiation.

Focusing femtosecond laser pulse allows to achieve intensity of 10 TW/cm^2, in transparent dielectric materials. Those intensities are sufficient to trigger optical breakdown processes and induce permanent modification in the substrate structure. Linear absorption occurs when the photon energy is equal or higher than the gap energy E_g, of the irradiated material, see Fig 2.1a. However, this is not the case of the femtosecond laser used for irradiating the substrate. Thus only non-linear interaction occurs at the focal spot of the laser beam, see 2.1b.

2.1.1 Light-matter interaction

The non-linear absorption leading to free-electron plasma formation, can be separated in three contributions, see Fig 2.2.

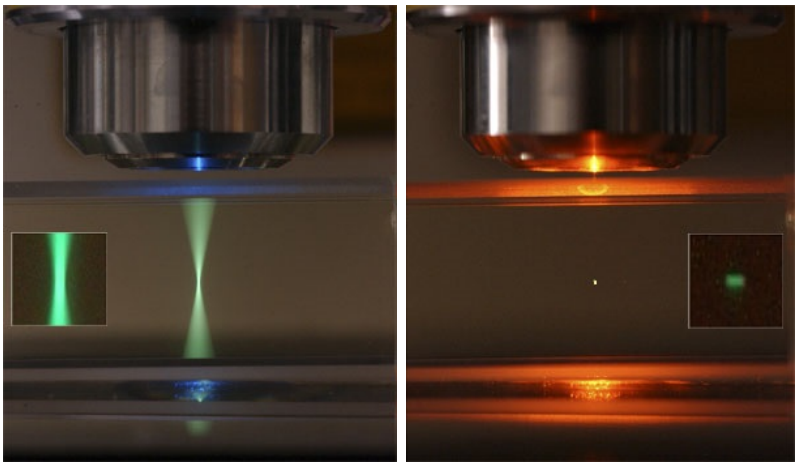

(a) Linear absorption **(b)** Non-linear absorption

Figure 2.1: The two figures show the difference between the linear fluorescent absorption (a) and the non-linear absorption leading to plasma generation in the focal spot of the laser (b). Picture taken by UC Berkeley.

Multi-photon absorption

Multi-photon absorption occurs when m photons interact with an electron in the valence band promoting it in the conduction band, on the condition that the total energy is greater than the bandgap: $mh\nu \geq E_g$, with h the Planck constant and ν the photon frequency. This phenomena is predominant for low intensity but high energetic photon, *i.e.* high frequency.

Tunneling ionization

When the electric field amplitude is high enough, the local band structure of the material is highly disrupted. It can lead to configuration where the valence and conduction become degenerated.In this configuration, an electron in the valence band can tunnel into the conduction band. This is the main process for regimes of high intensities but rather low photon frequency.

The Keldish parameter [53], gives a criterion to distinguish the two regimes,

$$\gamma = \frac{\omega}{e}\sqrt{\frac{m_e c \epsilon_0 n E_g}{I}}, \tag{2.1}$$

with ω, the photon pulsation, e the elementary electric charge, m_e the effective electron mass, c the speed of light,

ϵ_0 the vacuum dielectric constant, n the substrate refractive index, E_g the gap energy and I the laser intensity. For $\gamma \ll 1.5$ tunneling ionization dominates, while for $\gamma \gg 1.5$ multi-photon absorption is the main source for free electron.

Avalanche photoionization

This last phenomenon is due to the duration of the irradiation pulse. At sub-picosecond pulse, the absorption phenomena and dissipation ones are decoupled. It occurs when an electron is already present in the conduction band (from either of the two previous phenomena, or defect states). The absorption mechanism being much faster than the relaxation mechanisms, the free electrons accumulate energies until they transfer their energy to valence electron by impact ionization, promoting them into the conduction band. The number of free electrons then increases forming a plasma. When the plasma frequency $\omega_p = \sqrt{n_e e^2 / m_e \epsilon_0}$ reaches the laser pulsation ω, the plasma becomes strongly absorbing reducing the production rate of free electrons. Avalanche photoionization occurs for long pulse duration in material with great bandgap energy.

This last process is highly important in FLM since it is rather independent on the laser frequency. Because of this, FLM can be applied in a variety of materials as plasma generation strongly depends on the timescale of the laser pulse, but only linearly on the frequency and the intensity of the laser beam.

On the other hand avalanche photoionization initiate by impurities is highly undeterministic as it depends on the defect distribution in the substrate, as opposed to multi-photon ionization and tunneling ionization.

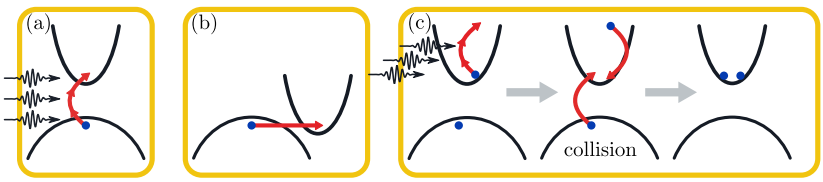

Figure 2.2: Schematic of the non-linear photoionization processes occurring during a femtosecond laser pulse. In (a) the multi-photon absorption mechanism, (b) shows the tunneling ionization and in (c) the process of avalanche photoionization.

2.1.2 Relaxation phenomena

There are several mechanism that can transfer energy from the free electron plasma to lattice deformation. While the interactions of the free electrons with themselves (carrier-carrier scattering) and with the lattice (carrier-phonon scattering) are in the same scale as the pulse duration, the dissipation mechanism are slower. The lattice heating diffusion, occurs at scale of several pico-second, while shock waves emission is a slower process that occurs at time scale of the nano-second. As a result the absorption and relaxation processes are decoupled in FLM, allowing for more precise machining of the material. The time scale of the different process occurring in FLM are summarized in Fig 2.3.

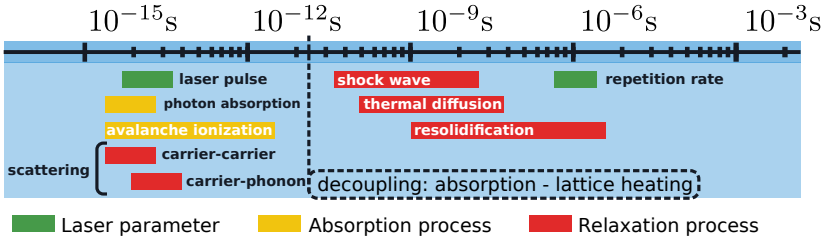

Figure 2.3: Time scale of the different processes involved in femtosecond laser irradiation of transparent materials.

Although all the physical mechanisms involved in the material modification are not fully understood, one can distinguish three main type of structural changes depending on the exposure parameters. The main parameters being: the beam average power, the pulse duration, the repetition rate and the scan speed. The structural changes are as follow.

Smooth Refractive Index Change

When the energy fluence of the irradiating beam is low, but still above the modification threshold, the material endures smooth permanent refractive index change. There are several mechanism that are involved all localised at the focal spot, among which: rapid quenching of the melted glass, formation of color centers, effects due to ion migration and shock waves [79]. Depending on the used substrate, the weights of those effects varies. In this regime the dielectric material, typically glass, retains its transparency properties, rendering it the best choice for waveguide writing.

Birefringent Refractive Index Change

At higher fluence, the formation of nanogratings in fused silica was observed [62, 92] which renders the modified region birefringent. In this regime, the polarization of the writing beam directly determine the nanograting orientation [45]. The commonly accepted explanation is given in a three step process: 1) inhomogeneous dielectric breakdown and formation of nanoplasmas, 2) modification of the material on the nanoscale to create which accumulate into nanoplanes, and 3) self-organization of the nanoplanes.

Void Formation

For high pulse energy, great pressure is generated by scattering of the free electron energy to the ions and a shockwave leaves a hollow core region surrounded by higher refractive index. Although not suited for waveguide writing, those voids can be exploited for 3D memory storage [34], or photonic bandgap material [51].

2.2 Writing waveguides: important parameters

2.2.1 Laser source

High intensity is generated thanks to the ultra short duration of the laser pulses. The main influence of this parameter is to determinate which non-linear process is triggered while writing. Contrary to fuse-silica, it was reported that the pulse duration has little influence on borosilicate glasses between 300 to 700 fs [79].

The laser wavelength determines mainly the weight between multi-photon absorption and electron tunneling ionization mechanisms. In some cases, it might be preferable to write with lower wavelength [98].

Because the absorption and relaxation mechanisms are decoupled in time (see Fig 2.3), if the time between laser pulses is short, it can results in an accumulation of heat at the focal volume. This is called the *accumulation regime* [26]. Indeed, when the repetition rate is low (1-100kHz) each laser pulse can be considered independent as the thermal diffusion has time to spread the energy away from the

focal spot. In this regime the waveguides cross section is highly asymmetric as the modified region is directly related to the shape of the focal volume. However, the writing speed has to be low in order to have a continuous modified region. This regime is typically exploited to write waveguides in fused silica. On the other hand at high frequency (>300kHz) the heat is accumulated at the focal spot. As a result, the modified region is more symmetric. The drawback is that at a given power and high repetition rate, the pulse energy is lower. The increased repetition rate allows to use increased scanning speed (20-100mm/s) rendering the process faster. This regime is used with borosilicate and aluminosilicate glasses. [25] At moderate accumulation regime, around 100kHz, effects of both regime combine [77]. The energy of the pulse is still high enough to trigger modification, and the repetition rate allow thermal heat accumulation to render the waveguide cross-section more symmetric.

As previously mentioned, the polarization is mainly involved with nanograting formation. In linearly polarized writing laser beam, the nano-planes are formed perpendicular to the polarization. While fused silica is strongly dependent on the writing polarization, borosilicate glasses seems to be insensitive in the heat accumulation regime

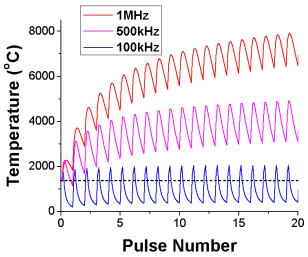

Figure 2.4: Using a finite difference thermal diffusion model, the temperature in the focal volume. Image from [25].

2.2.2 Beam focusing

The deposition of energy is highly dependent on the size and shape of the focal spot. We use microscope objective that are already compensated for chromatic and spherical aberrations. Using high numerical aperture objective allow to focus the beam into smaller region and thus increase both irradiation intensity and locality at the modified volume.

Shape of the focal spot

In the linear propagation approximation, Considering the incoming writing beam as a Gaussian beam, the waist and depth of the focal spot is given by,

$$w_0 = \frac{M^2\lambda}{\pi NA} \qquad z_0 = \frac{M^2 n\lambda}{\pi NA^2}, \tag{2.2}$$

with M the Gaussian beam propagation factor, λ the wavelength of the laser source, NA the numerical aperture of the lens, n the refrecative index of the medium, w_0 the waste of the beam at the focal spot and z_0 the elongation of the focal spot.

Spherical aberations

Even though compensated, spherical aberrations are still present when a focused beam pass through the interface of a different refractive index material. They render the writing process highly dependent from the depth of focusing. The effects lower the peak intensity inside the focal point and modify its shape. Those phenomena become more significant for increasing numerical aperture of the lens as well as for increasing refractive index difference [44]. Using water- or oil-immersed objective, one can reduce the aberration and write directly at the bottom of a sample.

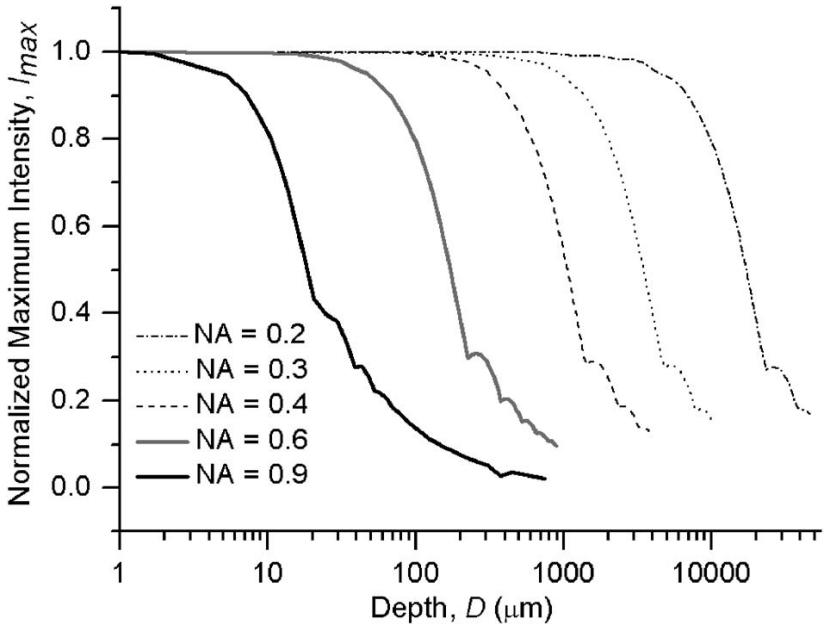

Figure 2.5: Simulation of the evolution of the peak intensity with the focusing depth for different Numerical Aperture. The beam is focused from the air $n_1 \simeq 1$ into the substrate is fused silica of refractive index $n_2 = 1.453$.

2.2.3 Writing geometry and post treatment

Longitudinal VS transversal

Moving the substrate longitudinally with respect to the incident laser beam, see Fig 2.6a, leads to obtaining waveguides with circular cross-section. However, the writing is limited by the working distance of the lens.

Translating the substrate perpendicularly with respect to the laser beam, see Fig 2.6b, the length of the waveguide is no longer limited by the working distance of the lens. The drawback is that the cross-section becomes asymmetric due to the elongated shape of the focal volume. The elliptic cross-section can lead to non-negligible birefringence. Although undesired for polarisation insensitive propagation, this feature can be useful in some cases, such as to make polarising beam splitter [83]. There exists several techniques to render the cross-section more symmetric in the transverse writing configuration. Some of them being: beam shaping [18], multiscan writing [105].

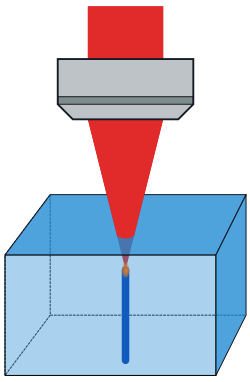

(a) Longitudinal writing

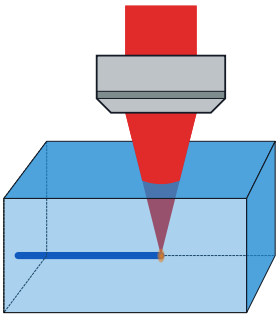

(b) Transverse writing

Figure 2.6

Shape of the index profile

The modified region, induced by the light-matter interaction in the femtosecond laser writing, has a resulting higher refractive index than the bulk glass substrate one, n. This creates a core-cladding situation (see Fig 2.7) that can guide light as in an optical fiber. In this case, the core region has a higher refractive index $n_{core} = n(\mathbf{r}) + \Delta n(\mathbf{r})$ than the cladding region with $n_{cladding} = n(\mathbf{r})$, which is a necessary condition to observe self propagating modes in the system.

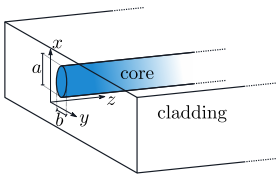

Figure 2.7: Figure of a general elliptic refractive index cross-section.

To understand the effect of the cross-section shape of the refractive index, we recall in the following the basics of light propagation in optical waveguide.

Starting from Maxwell's equations, one can show that the electro-magnetic field propagates in a dielectric follow the equation [101],

$$\nabla^2 \mathbf{E}(\mathbf{r}, t) - \left(\frac{n^2(\mathbf{r})}{c^2}\right) \frac{\partial^2 \mathbf{E}(\mathbf{r}, t)}{\partial t^2} = 0, \qquad (2.3)$$

where $\mathbf{E}$ is the electric-field, n the refractive index of the medium, c the speed of light in vacuum. Given the continuity of the fields at the core-cladding interface and the

continuous translational invariance in the propagation direction along the z-axis, there is only a limited number of solution that are eigenstates of eq (2.3). Those solutions are called *modes* and describe the spatial distribution of the energy in the cross-section of the waveguide.

The typical refractive index difference induced by the FLM technique is of order of $\frac{\Delta n}{n} \sim 10^{-3}$. Such low relative refractive index correspond to the case of *weakly guiding dielectric waveguides*. In this case, the EM-field can be described by a plane-wave in the propagating direction, with an intensity only spatially varying in the cross-section plane. We can write the electric field as,

$$\mathbf{E}(\mathbf{r}, t) = E(x, y)e^{i(\beta z - \omega t)}, \tag{2.4}$$

where β is the propagation constant, ω the optical frequency and E the transverse scalar spatial field profile. This lead to the Helmholtz equation,

$$\boldsymbol{\nabla}^2 E(x, y) + k^2 n^2(x, y)\, E(x, y) = \beta^2 E(x, y), \tag{2.5}$$

which is formally identical to the Schrödinger equation, where the refractive index plays the role of the potential energy. In the case of a circular step index profile, the eigenstates of eq (2.5) are the Linearly Polarised modes, LP_{ml}, denoted by the index m and l (see Fig 2.8a). LP_{01} is often called the *fundamental mode*. The number of modes supported by a waveguide is given by the number,

$$V = \frac{2\pi}{\lambda} a \sqrt{n_{core}^2 - n_{cladding}^2}, \tag{2.6}$$

where a is the core radius, λ the free-space wavelength.

Because it allows to discard inter-modal power transfers, single mode waveguiding is a crucial feature for a majority of integrated optics application. As eq (2.6) and Fig 2.8b show, the fundamental properties of the guided modes depends on the shape of the refractive index profile. A typical shape of the refractive index after femtosecond laser writing in borosilicate is shown in Fig 2.9.

The symmetry of the refractive index profile around the center also determine the polarisation dependency of the

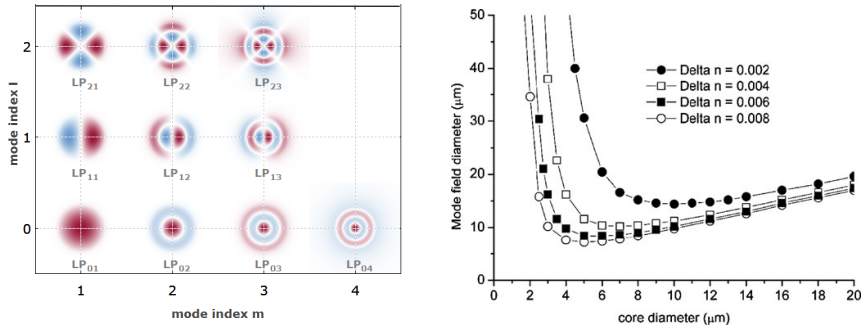

(a) **(b)**

Figure 2.8: In (a) a subset of the E-field profile of the modes solution for a waveguide of circular step refractive index profile (image from https://www.rp-photonics.com/lp_modes.html). (b) Mode field diameter evolution with respect to the core diameter of a waveguide with a step index profile (image from Ref [79]).

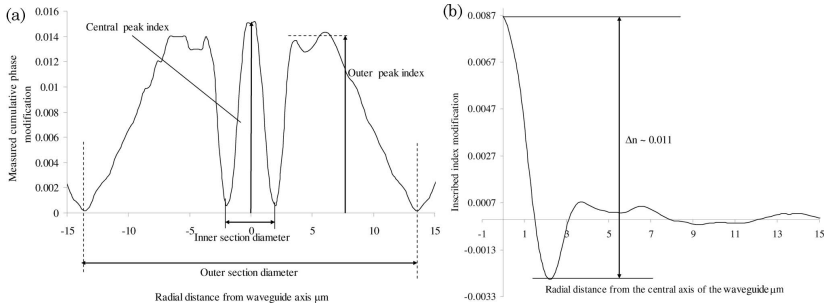

Figure 2.9: Figures (a) sows a typical cumulative phase profile obtained with the quantitative phase microscopy method on a waveguide written in borosilicate with X-polarized light, an energy of 19,6 nJ, scanning velocity of 55 mms -1 , and at an approximate depth of 55 μm. From this measurement, one can compute the radial index profile (b) of the waveguides. Images taken from Ref [2]

propagating mode. If there is a high birefringence, the polarized modes TE and TM are highly uncoupled but become too different, introducing polarization decoherence. On the other hand, this elliptical shape can be helpful and used in order to tune the birefringence of the waveguide.

Annealing

The writing process with femtosecond laser can introduce some defects, color centers and stresses in the modified region of the glass. A thermal treatment of glass, also known as annealing, can be used to suppress internal stresses [106] and reduce the number of color center in the glass substrate. Indeed, the melted glass formed during fabrication has to cool quickly enough to avoid crystallisation, but if too quick, the modified region can accumulate strong mechanical stresses as the bulk and modified region cool down and shrink at different rates.

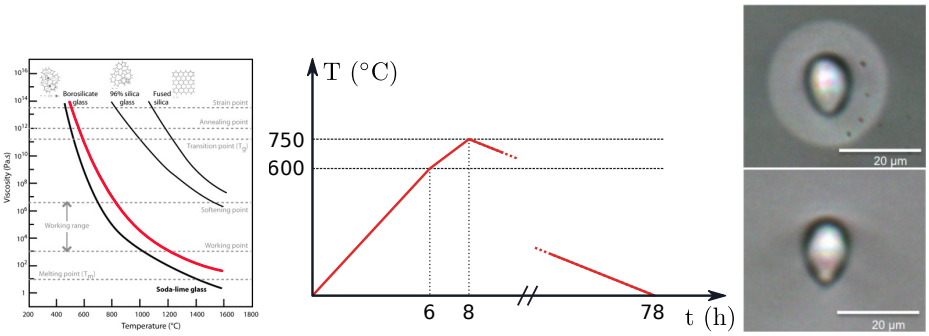

(a) Viscosity VS Temperature

(b) Annealing diagram

(c)

Figure 2.10: Figure (a) shows the evolution of the viscosity with the temperature of a glass material (from [93]). The red curve corresponds to borosilicate material, and the horizontal dotted lines are the levels associated to the characteristic temperature definition. In (b) we show a typical annealing protocol for thermal treatment of waveguides. In (c) a pictures from a microscope of the cross-section of a waveguide before (top picture) and after (bottom) annealing post-treatment. Images taken from [3].

The annealing process consists of playing with the different characteristic temperatures of a glass material, as well as with the heating speed (deg/h). The different characteristic temperature are related to the viscosity of the glass [111] and are defined as: (see Fig 2.10a)

- *Strain point*: corresponds to the temperature where the

glass release its internal stresses while remaining solid and keeping its shape. Note that below this temperature, it is not possible to relieve the stresses in the glass.

- *Annealing point*: corresponds to the temperature where stresses are released in few minutes due to viscous relaxation.
- *Softening point*: at this temperature, the glass is viscous enough to loose its form against its own weight. The deformation rate scale is around 1 mm/min.
- *Working point*: it is the temperature from which the glass can be shaped using glassforming techniques such as blowing or pressure. It is at this temperature that gaffers work the glass material.
- *Melting point*: contrary to crystal material, glasses have no well defined melting point as there is no actual phase transition. Nonetheless, one can define a temperature to discriminate between a soft form and a liquid form which is the melting point.

In the context of waveguide post-irradiation, a typical annealing process presented in Fig 2.10b heat the sample until it reaches the annealing point, then let the sample slowly cooling down thus avoiding the re-accumulation of additional strain.

The main consequence of annealing on the waveguides is to modify the index profile, reducing the modified refractive index to the modified glass volume, see Fig 2.10c. Moreover, it decrease the birefringence and can reduce the propagation losses. Using this thermal treatment it has been possible to render multi-mode waveguides to single mode after annealing [3].

2.2.4 Other engineering techniques

In designing waveguide with FLM technology, there are many approach to fabricate waveguides and tune their properties. We already explain the main contributions in the guiding properties of waveguides, but different treatments can be used and are only limited by the imagination of engineers.

As an example, birefringence can be tuned using the shape of the refractive index profile and rotating it, see

Fig 2.11a, but can also be shaped by writing structures next to the guiding waveguide, see Fig 2.11c.

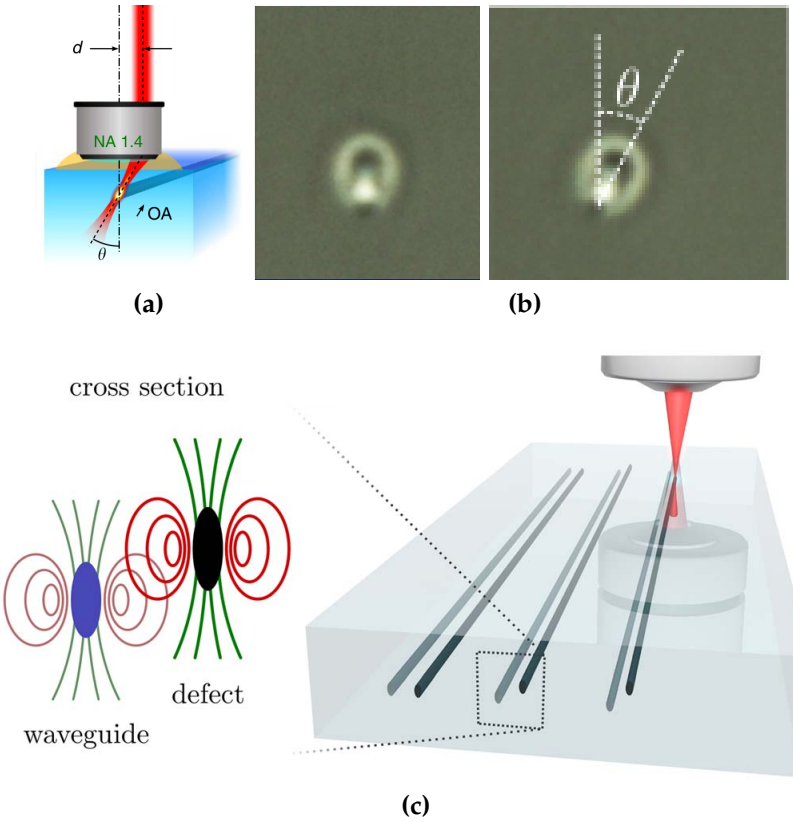

Figure 2.11: Image (a), (b) from Ref [19]. Image (c) from Ref [41].

2.3 Application for quantum photonic circuit

Femtosecond laser micromachining is a very versatile technology that finds applications in micro-fluidics, astrophotonics and in the case of this thesis in quantum photonic. We will present in this section the direct application of the FLM toward the fabrication of quantum integrated circuits.

2.3.1 Fundamental building blocks for quantum linear optics

The fundamental components of integrated electronics for classical computing are the transistors, inductances and capacitances. Likewise, in integrated photonic the main components are the directional couplers (that play the role

of beam splitters), phase shifters, Mach-Zehnder elements, ring resonators, grating couplers and others used in more specific cases.

The advantage of integrated optics is that it allows the circuit to achieve subwavelength stability for the phase shifts. It has been shown that every linear quantum operator can be simulated in quantum optics by a linear network made of beam splitters, phase shifters and mirrors [91]. We will thus presents how FLM successfully implement those elements as well as other useful components for making photonic processors.

Phase shifters

Apart from the single mode waveguide itself, the simplest element for quantum integrated photonic is the phase shifter. One can introduce phase shifting by elongating the path of a waveguide. However to control the phase, one can make use of electro-optical effects or thermo-optic effects as in Ref [17].

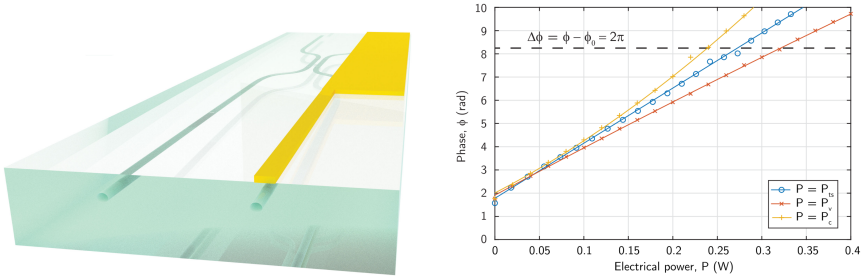

(a) Thermal phase shifter.

(b) Phase shift with electrical power.

Figure 2.12: In (a) is shown a sketch of a waveguide above which is deposited a layer of gold. By making circulating a current through this layer, the gold is heated from Joule effects as well as the material just below. This changes the refractive index of the heated region. On figures (b) we is displayed the phase shift acquired with respect to the electrical power that is applied to the golden layer. Images from [17].

Variety of techniques has been developed to make those phase shifters and often the waveguides need to be written at the surface of the sample. Phase shifters can be used for correcting the phase of an optical network after its fabrication and characterisation. On the other hand, they are integrated in Mach-Zehnder to implement optical switches.

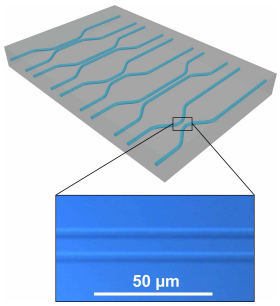

Figure 2.13: Directional couplers of different shape, showing the multiple parameters that can be varied to tune the splitting properties of the integrated beam splitters. Images from Ref [68].

Directional couplers

A directional coupler is a component that makes use of the evanescent coupling between two waveguides to split the power. It is though strongly wavelength dependent. This property has been used for multi- and demultipling devices [27], mostly used in optical networks. Because of the parameter range available when using FLM, it is possible to tune the directional couplers to achieve a continuous range of splitting ratio.

The first demonstration of building directional couplers with the FLM technique was achieved in 2001 by Streltsov et.al [103]. Since then directional couplers have been a fundamental component in integrated quantum optic for multi-photon interference, beginning with the two photons interferene of the Hong-Ou-Mandel configuration (see Fig 2.14b).

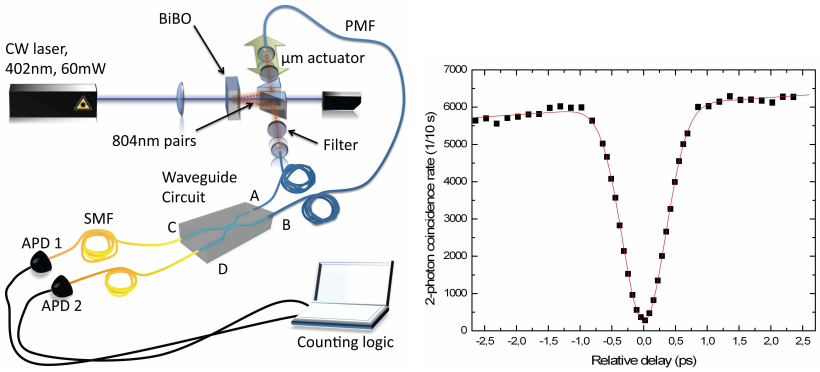

(a) **(b)**

Figure 2.14: Figure (a) shows the experimental setup to measure the two photons coincidence in a Hong-Ou-Mandel configuration, where the indistinguishable single photons are produced by Parametric Down Conversion in a BiBO crystal. Figure (b) shows the second order correlation from the experiment in (a), versus the relative delay between the two interfering photons. Images from Ref [68].

Polarisation dependent waveguides can be used to build integrated polarising beam splitters. Those devices have been used to demonstrates the integrated photonic implement of a C-NOT gate in plarization encoding [20, 120].

Directional couplers are not limited to planar geometry, as illustrated in Fig 2.15. The 3D feature of FLM can be use to tune the polarisation sensitivity of the couplers, but also to couple more than two modes.

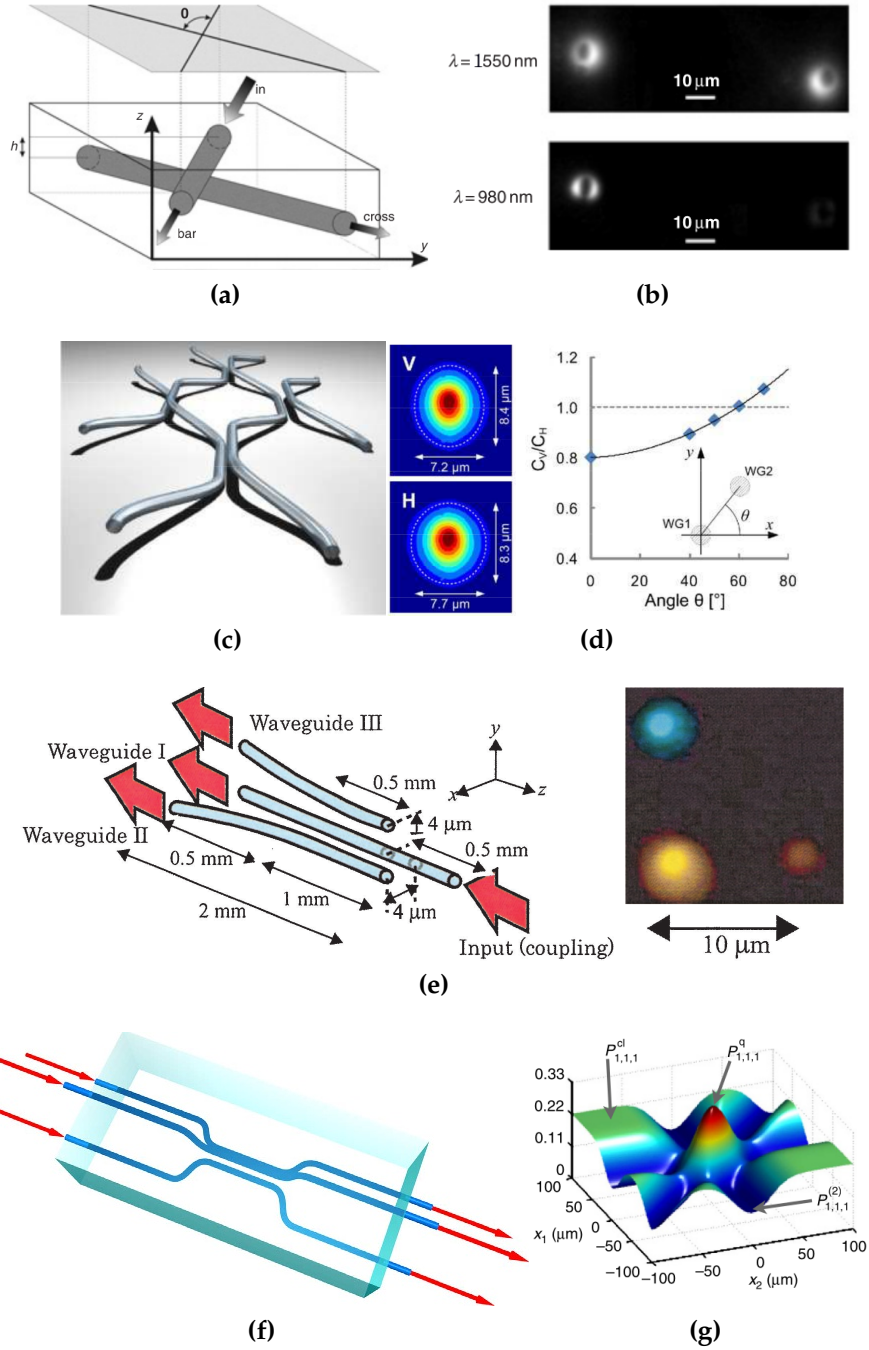

Figure 2.15: Figure (a) shows a X-coupler in which the coupling ratio is tuned by the angle α between the waveguides [78]. The splitting is still wavelength depends, as shown in (b). Figure (c) shows the schematic of 3D directional coupler to render the splitting polarisation insensitive [95]. The graph in (d) display the ratio of the coupling constant for the two polarisations k_V/k_H as a function of the coupling angle. Figures in (e) display a three-mode directional coupler (tritter) and a picture of the near field profile of the output modes [115]. This tritter configuration can be used to observe three-photon interference as shown (f) with a simulated $P_{1,1,1}$ coincidence counting in the Hong-Ou-Mandel configuration [102].

Mach-Zehnder as switche and one-qubit gate

A Mach-Zehnder is an interferometric component. It comprises two beam splitters (one at the beginning to split an incoming mode, and one at the end for recombining the separated modes). Between those, the two modes accumulate a relative phase, $\Delta\phi$. The transfer matrix of a two modes Mach-Zehnder Interferometer (MZI) is given by,

$$MZ(\Delta\phi) = \begin{pmatrix} 1 & -i \\ -i & 1 \end{pmatrix} \cdot \begin{pmatrix} e^{i\Delta\phi} & 0 \\ 0 & 1 \end{pmatrix} \cdot \begin{pmatrix} 1 & -i \\ -i & 1 \end{pmatrix} \tag{2.7}$$

$$= e^{i\frac{\Delta\phi}{2}} \begin{pmatrix} \sin\left(\frac{\Delta\phi}{2}\right) & \cos\left(\frac{\Delta\phi}{2}\right) \\ \cos\left(\frac{\Delta\phi}{2}\right) & -\sin\left(\frac{\Delta\phi}{2}\right) \end{pmatrix}. \tag{2.8}$$

Figure 2.16: Scheme of a generic Mach-Zehnder interferometer.

From this, one can see that sending light in input mode a of total power P_0, will lead to a power in output mode c and d of $P_c = \sin^2(\frac{\Delta\phi}{2})P_0$ and $P_d = \cos^2(\frac{\Delta\phi}{2})P_0$, respectively. Thus the transmitted power in mode c depends strongly on the relative phase between the modes. Because of this, MZI have a large range of application such as highly sensitive thermal detectors (thermal-optical effect) or more related to quantum optics, they can be used as optical switches. Indeed, tuning $\Delta\phi = 0$ we have a total extinction of P_c, while tuning $\Delta\phi = \pi$ we have a total transmission in P_c.

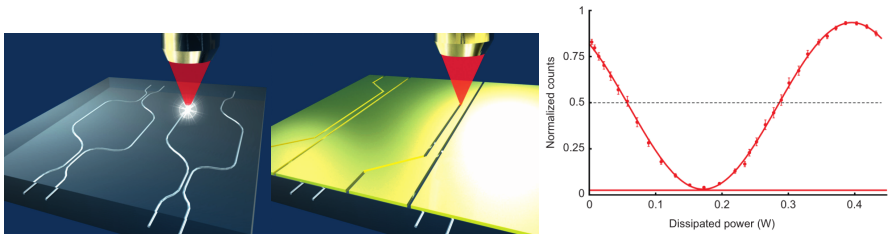

(a) **(b)** **(c)**

Figure 2.17: Two steps process to build a thermally reconfigurable MZI. The waveguides are written first in (a), then the sample is coated with a thin golden layer which is ablated using the same FLM technique. In (c) is displayed the normalised count rate resulting of a single photon input. The unbalanced phase is proportional to the dissipated power due to Joule effect, with $\phi = \Phi_0 + \alpha\mathcal{P}$ where $\mathcal{P}$ is the dissipated power, α a constant and Φ_0 an initial relative phase. Images from Ref [29].

In addition, configurable Mach-Zehnder components are useful in quantum processing protocols. For instance, we

will show how a MZI allows to perform an arbitrary rotation on a qubit in path encoding.

As mention in sec 1.1.1, a rotation along the axis $j = x, y, z$ is given by the operator $\hat{R}_j(\phi) = e^{i\hat{\sigma}_j} = \cos\left(\frac{\phi}{2}\right)\mathbb{1} + i\sin\left(\frac{\phi}{2}\right)\hat{\sigma}_j$. Considering the rotation around the z-axis of the Bloch sphere,

$$\hat{R}_z(\phi) = e^{i\phi/2}\begin{pmatrix} e^{i\phi} & 0 \\ 0 & 1 \end{pmatrix} = e^{i\phi/2}\hat{P}_1(\phi), \tag{2.9}$$

where $\hat{P}_1(\phi)$ is the operator for a phase shift in mode 1. Now, for a rotation around the y-axis of the Bloch sphere, the matrix representation of the rotation operation becomes,

$$\hat{R}_y(\phi) = \begin{pmatrix} \cos\left(\frac{\phi}{2}\right) & \sin\left(\frac{\phi}{2}\right) \\ -\sin\left(\frac{\phi}{2}\right) & \cos\left(\frac{\phi}{2}\right) \end{pmatrix}. \tag{2.10}$$

The same matrix operation is achieved when we consider a MZ with a pre-phase shift of π and an internal phase unbalanced phase shift between the two mode of $\theta = \phi - \pi$,

$$\begin{pmatrix} e^{i\pi} & 0 \\ 0 & 1 \end{pmatrix} \cdot MZ(\theta) = ie^{i\theta/2}\begin{pmatrix} -\sin\left(\frac{\theta}{2}\right) & -\cos\left(\frac{\theta}{2}\right) \\ -\cos\left(\frac{\theta}{2}\right) & \sin\left(\frac{\theta}{2}\right) \end{pmatrix} \tag{2.11}$$

$$= ie^{i\theta/2}\begin{pmatrix} \cos\left(\frac{\phi}{2}\right) & \sin\left(\frac{\phi}{2}\right) \\ -\sin\left(\frac{\phi}{2}\right) & \cos\left(\frac{\phi}{2}\right) \end{pmatrix}. \tag{2.12}$$

All in all the MZ presented in Fig 2.18, is mathematically equivalent to perform a Bloch rotation on the path encoded qubit state if we choose the phase shifts to be $\phi_1 = \theta_z + \pi$ and $\phi_2 = \theta_y - \pi$.

2.3.2 Integrated photonic gates

Previously, we have already shown that Mach-Zehnder interferometers can be used to implement single qubit quantum gates in a path encoding. However, two qubits gates are a necessary feature for achieving universal quantum computing. Using polarisation encoding, a FLM written integrated photonic CNOT gate has already been demonstrated, see Fig 2.19a. An other important multi-qubit gate

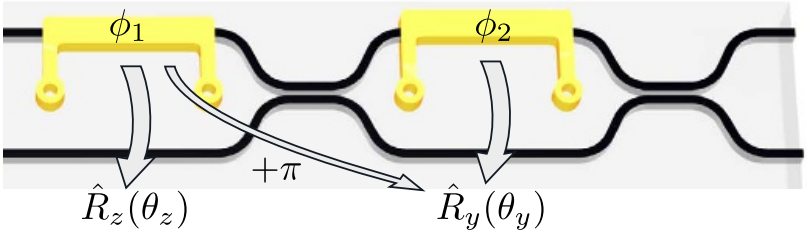

Figure 2.18: Mach-Zehnder with phase shifter, implementing rotation operation around z and y-axis in the Bloch sphere representation of a path encoded qubit. Image redrawn from Ref [100].

is the C-Z gate (see Fig 2.19b), that operates a conditional sign-flip in one of the qubit state. It has been shown that C-Z and C-NOT gates are equivalent, up to a single qubit Hadamar gate.

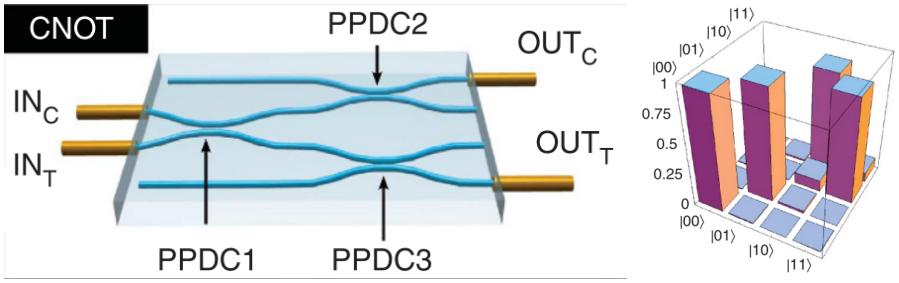

(a)

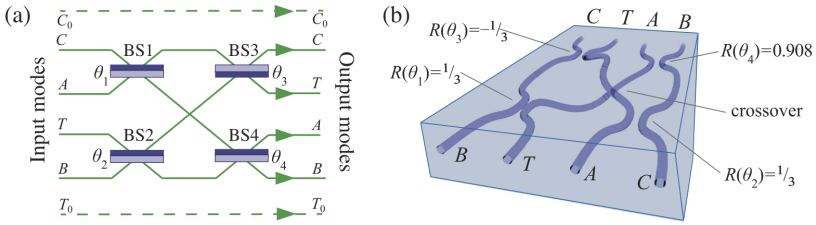

(b)

Figure 2.19: (a) Integrated implementation of a C-NOT gate in polarisation encoding, using partially polarising directional couplers [20]. Next to it the measured truth table of the circuit operation. (b) Implementation of a C-Z gate for path encoding using a heralding scheme [70]. On the left is the schematic of the circuit with A and B the path of the ancillary qubit. The control and target photon are encoded in the path C_0 and T_0 for qubit state $|0\rangle$, and in path C and T for qubit state $|1\rangle$.

Chapter 3

Experimental setup and methods

Contents

Introduction

There are a variety of femtosecond lasers used for micromachining waveguides in glass substrates, we will thus only present the fabrication setup used in the present thesis. Likewise for the characterisation, although there are several way to measure the same quantity (*e.g.* propagation losses), we will explain the measurement setups that were used in our work.

3.1 Fabrication setup

As displayed in Fig 3.1, the fabrication setup consists on delivering a laser beam to lens, which focuses the beam in

the glass sample glued on a motion stage.

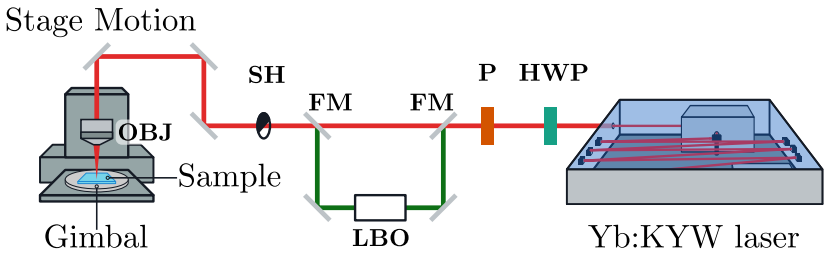

Figure 3.1: Fabrication setup used for writing waveguides: the femtosecond laser beam is firstly attenuated by passing through a half-wave plate (HWP) and a Glan-Thompson polarizer (P). It is then either focused with an objective (OBJ) on a glass sample mounted on the motion system, or deviated into a temperature controlled lithium triborate crystal (LBO) for second harmonic generation, using flip mirrors (FM). In both cases the beam passes through the mechanical shutter (SH).

In this setup, a Yb-based cavity-dumped mode-locked oscillator laser produces a femtosecond laser beam at 1030nm. The average power of the beam is controlled with a half wave-plate (HWP) followed by a Glan-Thompson polariser. The polariser also allows to fix the writing polarization.

Using flip mirrors (FM), the laser beam can pass through a lithium triborate crystal (LBO) generating the second harmonic at 515nm. The conversion efficiency of power from the input 1030nm to the output 515nm beam, serves as a reference for reproducibility. If not flip, the 1030nm laser beam is directly focus to the sample using a microscope objective (OBJ) 50X with a 0.6 numerical aperture. In either cases, a mechanical shutter synchronized with the stage motion is used to switch the beam ON and OFF during fabrication with a millisecond switch time.

The sample is mounted on a precise motion stage that can move linearly in the three dimension. A gimbal adjuster (Thorlabs GM100) allows to finely tune the alignment of the sample with the beam. This alignment is carried out with a CCD camera able to collect the back-reflection of the laser beam when focused on the sample surface.

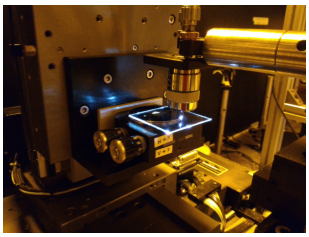

Figure 3.2: The picture shows a 25×25mm glass sample during femtosecond laser waveguide writing. The bright spot is the visible plasma, generated by the high intensity light-matter non-linear interaction.

3.1.1 Laser source

The laser used to generate the writing beam is a diode-pumped Yb:KY$(WO_4)_2$ laser oscillator with cavity dumping [55]. This laser produces 350fs pulses at wavelength 1030nm with maximum energy of 1μJ.

A pump diode is used to excite a 1 mm-long crystal rod made of $KY(WO_4)_2$ (Potassium Yttrium Tungstate) doped with Yb (Ytterbium) at 5% in concentration. The diode provides an optical power of 15W at a wavelength of 981 nm to the active material, whist the latter emits at 1030 nm. The 8.9 m long resonant cavity is folded to a 90 cm$\times$50 cm square by a set of curved and highly-reflecting mirrors. Mode-locking [1] is achieved using SEmiconductor Saturable Absorber Mirror (SESAM) placed at extremity of the resonant cavity. The internal repetition rate of the mode-locked regime is 17MHz. A β-barium borate Pockels cell (BBO PC) and a thin-film polariser are used for the cavity dumping. Together, they act as a switch which modulates the pulse generation at a wanted repetition rate in the submultiples range of the internal 17MHz. With this model, the repetition rate spans from few kHz to 1.1MHz. In our case, the repetition rate is set to be 1MHz during the waveguide writing. An external high voltage signal drives the Pockels cell, and is synchronized with the internal pulses propagating inside the cavity due to mode-locking.

[1] Mode-locking or phase-locking, refers to the lasing state where a sufficient numbers of internal laser modes have a constant fixed dephasing (referred as locked modes). As a result, a periodic burst is produced with a pulse duration inversely proportional to the number of locked modes.

3.1.2 Stage motion

To move the glass substrate, we use a precise stage motion that is controlled with a software, which reads a file written in G-code programming language that gives the movement instructions. The motion system (Aerotech FIBERGlide 3D) is comprised of three independently controlled linear translation stages. Fully-preloaded air bearing provides an ultra-smooth velocity control using linear brushless servomotor, while a linear encoder feedback provides up to 2 nm resolution. The motion system is completely noncontact designed, which allows to achieve velocities up to 100 $mm.s^{-1}$, with positional precision of 100nm, in a range of 10 cm$\times$15 cm$\times$5 mm in the X$\times$Y$\times$Z directions respectively.

3.1.3 Post fabrication treatment

After direct laser writing fabrication, the sample is thermally treated in a oven from room temperature to 750°C. In a different step, to prepare the sample for characterisation, the input/output faces of the glass substrate are pol-

ished so as to minimize the losses by scattering. We use a motorised polishing machine with a succession of sand paper discs, starting from 30 to 0.3 μm grain roughness. The process is repeated for each faces.

3.2 Characterisation setup

When the sample is fabricated and polished, we characterize a number of properties of the optical circuit. We will only present the measurement setup related to this thesis.

3.2.1 Microscope inspection

The first measurement carried on the written samples is a visual inspection by a microscope. Although small, the refractive index change is sufficient to render the waveguides visible. Looking at the top surface, we can check if the fabrication geometry mismatches the one specified in the G-code, that could possibly result from misalignment. More importantly we control the uniformity of the written waveguide as well as the possible presence of defects such as interruptions or burnings. Those defects can stem from dust on the surface after cleaning. Regarding the lateral facets, we can check the cross-section of the waveguide and their actual depth.

The equipment used is a Nikon ME600 microscope. The accrued visibility of the waveguides is provided by a Differential Interference Contrast (DIC) module. Pictures are taken by the installed CCD camera (PixeLINK B871).

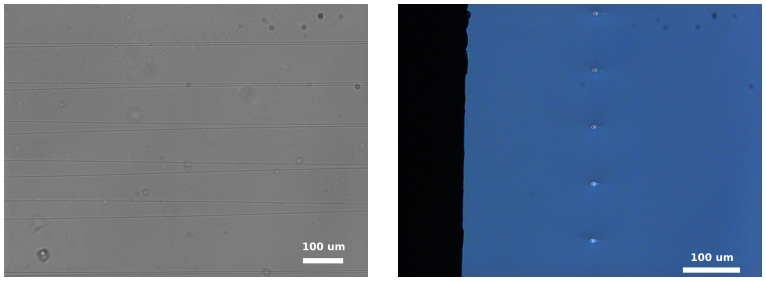

(a) **(b)**

Figure 3.3: (a) Top picture with a microscope of parts of directional couplers. The dark lines are the region of modified refractive index, *i.e.* the waveguides. In (b) we show the cross section of waveguides before annealing and after polishing. The picture is taken under polarisation light, highlighting the profile of the refractive index.

3.2.2 Device coupling

The guiding properties of the optical circuit are retrieved from classical light coupling characterisation. This includes the polarization response of the circuit, the mode profile and losses behaviour of the light propagating inside the written waveguides.

Light used for characterisation are coherent light produced by laser diodes and solid state lasers with wavelength ranging from 607 nm to 1550 nm. Depending on the property we want to study, there are two main configuration for coupling light in a waveguide: objective coupling, also called *end-fire* (see Fig 3.4b), and the fiber coupling, also known as *fiber-butt* coupling (see Fig 3.4a).

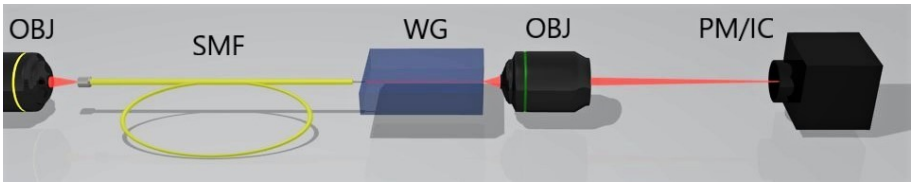

(a) Fiber coupling setup.

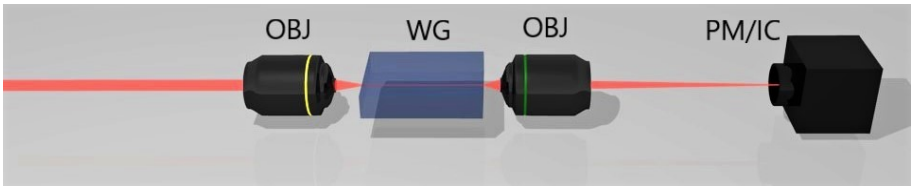

(b) Objective coupling setup.

Figure 3.4: In the fiber coupling setup (a), the laser beam is first coupled to a single mode fiber (SMF) with an objective (OBJ). The fiber is then couple to a waveguide by setting its tip as close as possible to the polished face of the sample, where the input of the waveguide (WG) is. We take advantage of the Fabry-Pérot effect to maximise transmission inside the glass sample. A second objective is used to collect the output light of the sample and focused on a power meter (PM) or an infrared camera (IC). Concerning the objective coupling (b), we superpose at best the focal point of the objective with the input of the waveguide. Both image are taken from Ref [82].

The end-fire coupling consists in focusing the incoming collimated laser beam onto the waveguide cross section by means of a microscope objective. The coupling efficiency is given by the matching of the focal spot size and the Numerical Aperture (NA) of the objective with the numerical aperture of the waveguide and its mode size. In practice, the typical NA of a waveguide is $\simeq 0.1$. Using this cou-

pling it is possible to control the polarization of the incoming light. The downside is that it is difficult to estimate the power losses due to the coupling.

In the fiber coupling configuration, the laser beam is first coupled to one end of a Single Mode Fiber (SMF) using an objective. The other end is peeled and cleaved to extract the cladding and core from the protecting wrapping. The bare fiber tip is then brought as close as possible to the waveguide cross section in order to maximise the superposition of the SMF and the waveguide modes. Since coupling efficiency can be well estimate by performing a numerical superposition of the intensity distribution of the modes, this configuration allows rapid measure of the power losses due to the waveguide. On the other hand, polarization propagation in fiber is unstable, thus rendering polarization characterisation of the waveguide less practical. Even though there are techniques to stabilise the polarisation propagation properties of fibers, it is then more convenient to turn to objective coupling.

The output light of the coupling apparatus is collected using a microscope objective. The light is then focused on a powermeter (Ophir NovaII and Anritsu ML9001A), or is imaged on a CCD camera (CCD camera Emdund OpticsEO-1312M for visible light, vidicon camera Hamamatsu C2400-03A and InGaAs camera Xenics Bobcat-640 for infrared light).

The different elements of the characterisation setup (objective, fiber-butt, sample) are aligned using a submicrometric position system. To optimize the positioning, the coupling objective and fiber are placed on a three-axis manual micropositioner (Melles Griot NanoMAX), where each knob provides a maximal precision of 50nm. Concering the sample, it is mounted on a tow translational-axis and two rotational-axis micropositioner (Thorlabs MBT40).

3.2.3 Mode profile

Part of the fiber coupling efficiency rapid estimation, relies on the measurement of the mode profile of both the single mode fiber and the waveguide modes profile. More generally, the measure of the mode profile gives information on the confinement properties of the waveguide, allowing to discriminate between single and multimode behaviour.

In many application, especially in quantum integrated

circuit, single mode waveguides are preferred. It simplifies greatly the study of the electric distribution $E(x, y)$, where the XY plane is the waveguide cross section. For the case of elliptic index profile waveguide, the fundamental mode does not suffer from sign inversion in its electric field distribution. It is thus possible to directly write,

$$E(x, y) = C\sqrt{I(x, y)}, \tag{3.1}$$

where $I(x, y)$ is the measurement intensity profile and C a real-valued constant. As we are only interested in the normalised electrical filed distribution, it is then sufficient to measure the intensity profile to obtain all the relevant information. However, we still have to take care of having the right scaling due to the collection objective magnification.

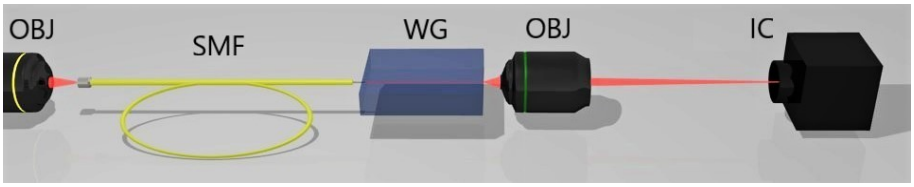

(a) Waveguide mode profile measurement.

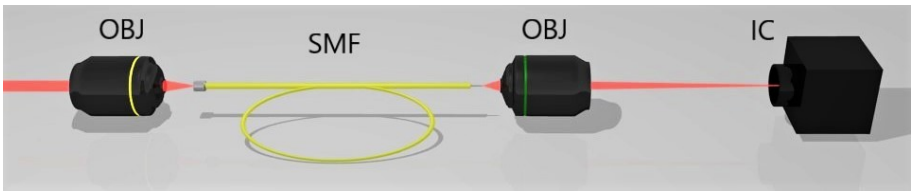

(b) Fiber mode profile measurement.

Figure 3.5: Protocol for mode profile measurement: (a) the input light is first objective (OBJ) coupled to the fiber (SMF), then to the waveguides (WG). The output light is collected and imaged on a CCD or Infrared camera (IC) depending on the characterisation wavelength in use. We then remove the sample and place the fiber tip near the collection objective, without changing the distance between the camera and the collection objective (b).

To carry out the measurement, we use the fiber coupling configuration. The output intensity of the waveguide is imaged on a CCD camera, see Fig 3.5a. A Matlab software is used to read and save the profile picture after we took care of not saturating the sensitive pixels. In order to get the scaling of the mode profile, we repeat the operation for the fiber tip, without changing the magnification of the objective-camera imaging, as shown in Fig 3.5b The size of the fiber being known, we can compare the two profile and

retrieve information on the waveguide mode as well as on the efficiency of the fiber coupling.

3.2.4 Characterising device losses

It is utterly important to characterise the losses of the fabricated optical circuit. This is especially true for quantum application where losses render the operation applied on the quantum state non-unitary.

However, measuring the output power only gives information on the total losses of the device, *insertion losses* (IL), defined as follow,

$$\mathrm{IL}_{dB} = 10 \log_{10} \left(\frac{P_{in}}{P_{out}} \right), \tag{3.2}$$

where P_{in} is the measured power of the output power of the fiber, while P_{out} is the output power of the waveguide when coupled to the fiber. Both power are measure after collection and focusing on the powermeter.

Insertion losses, positive by choice, can be decomposed into several different contributions:

- the *Fresnel losses* (FL), due to mismatching refractive index at the interface between two materials:

$$\mathrm{FL}_{dB} = -10 \log_{10} \left[1 - \left(\frac{n_2 - n_1}{n_2 + n_1} \right)^2 \right]. \tag{3.3}$$

- the *coupling losses* (CL), due to mismatch between the waveguide mode and the incoming mode,

$$\mathrm{CL}_{dB} = -10 \log_{10} \left(\frac{| \iint E_{wg} \, E_{in} \, \mathrm{d}x \, \mathrm{d}y \, |^2}{\iint |E_{wg}|^2 \, \mathrm{d}x \, \mathrm{d}y \iint |E_{fb}|^2 \, \mathrm{d}x \, \mathrm{d}y} \right). \tag{3.4}$$

  To retrieve the electric-field modes, we take a picture in the near field of both the fiber and the waveguide output intensity, using the same magnification. From the image, we fit the shape of the intensity with a 2D Gaussian, the typical profile of a single-mode in a waveguide. We retrieve the electric-fields, E_{wg}, E_{fb} of the waveguide and the fiber respectively, with: $I \propto |E|^2$.

- the *propagation losses* (PL), defined by the losses due to straight propagation in the waveguide per unit of length. It is given by:

$$\mathrm{PL}_{dB/cm} = \frac{-10}{l} \log_{10}\left(\frac{P(l)}{P(0)}\right), \tag{3.5}$$

  where l is the length of the straight waveguide, and $P(0)$, $P(l)$ are the power at the beginning and the end of the waveguide respectively.

- the *bending losses* (BL), are the extra-losses during propagation due to the curvature of the waveguide. A theoretical model is given in Ref [35], which gives an exponential dependency with respect to the curvature of the waveguide. For circular-bent waveguides,

$$\mathrm{BL}_{dB/cm} = C_1 e^{-C_2 R}, \tag{3.6}$$

  where C_1, C_2 are phenomenological constants, and R the radius of curvature.

  The insertion loss is thus given by,

$$\mathrm{IL}_{dB} = -10\log\left(\frac{P_{\mathrm{out}}}{P_{\mathrm{in}}}\right) = 2\mathrm{FL}_{dB} + \mathrm{CL}_{dB} + \mathrm{PL}_{dB/cm}\cdot l + \mathrm{BL}_{dB/cm}\cdot l_c, \tag{3.7}$$

with l_c the length of the curved path.

In the case of straight waveguides, we retrieve the propagation losses by subtracting all the other contributions to the insertion losses:

$$\mathrm{PL}_{dB/cm} = \frac{\mathrm{IL}_{dB} - 2\mathrm{FL}_{dB} - \mathrm{CL}_{dB}}{l}. \tag{3.8}$$

Coupling losses are estimated as mentioned and Fresnel losses computed from nominal values of the sample refractive index.

Our characterisation setup only allows for direct measurement of the insertion losses, and propagation losses are only obtain indirectly by estimating the losses at the input of the waveguide. For direct measurement of the propagation losses, one can measure the insertion losses of a straight waveguide of different length. However this process is longer and destructive, as one need to cut the same waveguide several time to perform the loss measurement.

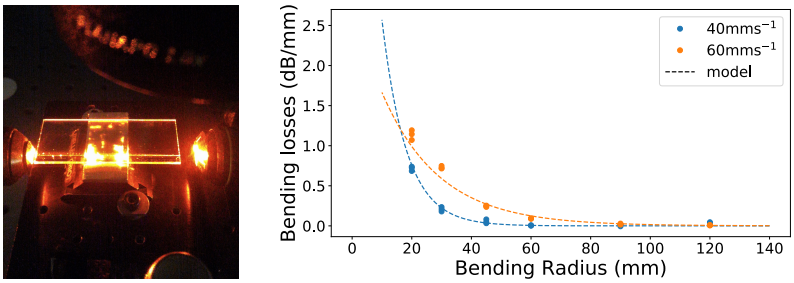

(a) **(b)**

Figure 3.6: In (a), an picture of the scattered visible light propagating in a straight waveguide. (b) Exponential fit of the calculated bending losses for different speed of stage motion.

To measure the bending losses, we compare the losses of waveguides with different radius of curvature but written with the same parameters. Thus the propagation losses are assumed to be comparable. We then fit the evolution of the bending losses with an exponential function.

Chapter 4

GHZ generation scheme

Contents

Introduction

4.1 GHZ states

4.1.1 Description and protocol

Ref [109] presents a complete description of a GHZ generation scheme in polarization encoding, including a discussion on photon loss effects as well as a discussion on the

source efficiency needed for high fidelity. From our side, we provide a path encoded interpretation of the theoretical demonstration.

In short, our scheme uses three photons for the encoding of the qubits in the GHZ state, and three other photons used as *ancillas* for the heralding of the operation sucess. The idea is to prepare the six photon state in a superposition of entangled states. We then measure the ancilla photons with several detectors. The preparation is such that the pattern of detection will herald if the remaining three photon state is successfully in the GHZ class [1]. The detection pattern that herald the success of the operation will be referred as the *heralding condition*.

[1] As explained in Ref [23], one can gather entangled states in groups that are equivalent through Stochastic Local Operation and Classical Communication (SLOCC). States belonging to the same class can undergo same protocols, as one can transform it to another state at a cost of a SLOCC.

However generating six identical photons is not an easy task. This is why our research is in collaboration with Pascale Senellart from Center for Nanosciences and Nanotechnology CNRS at University Paris-Saclay. Her team will provide the photon source based on quantum-dot technology [97].

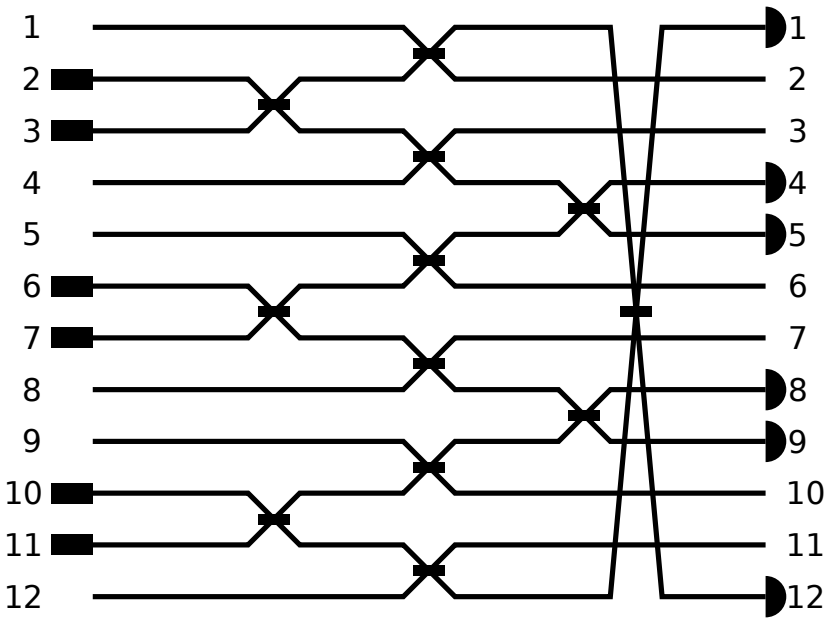

Figure 4.1: GHZ-factory device. Each black lines represents a waveguide, which we will refer as channels or modes. The crossed X parts represent 50:50 beam splitter. Boxes on the left of the figure are the input for the six identical photons, while semi-circles on the right represent the detectors used for the heralding.

Our design is presented in Fig 4.1, and will be implemented using Femtosecond Laser Micromachining (FLM) on borosilicate glass. The circuit presents twelve channels. On the left side of the device, the set of chan-

nels {2,3,6,7,10,11} corresponds to the input channels (black boxes). On the right side the same channels will define the output qubits. The output channels {1,4,5,8,9,12} are all terminated by a detection device (half-circles), which will allow post-selection of the state. Those channels will be referred as the *heralding channels*, since the detected photons herald the state one can expect in the other channels.

4.1.2 Qubits definition

As mentioned in the first chapter, the logical qubit encoding depends on the choice one makes. In our scheme, we choose to define the three logical qubits as follow,

$$|0\rangle_A = |0_2 1_3\rangle \qquad |1\rangle_A = |1_2 0_3\rangle\,, \tag{4.1}$$
$$|0\rangle_B = |0_6 1_7\rangle \qquad |1\rangle_B = |1_6 0_7\rangle\,, \tag{4.2}$$
$$|0\rangle_C = |0_{10} 1_{11}\rangle \qquad |1\rangle_C = |1_{10} 0_{11}\rangle\,, \tag{4.3}$$

where the subscripts A, B, C refer to three distinct parts of the device, foreseen from Fig 4.2. The kets $|0,1\rangle_X$ with $X = A, B, C$, are the logical qubits, while the kets $|0_i 1_j\rangle$, $|1_i 0_j\rangle$ with $i, j \in \{2, 3, 6, 7, 10, 11\}$ are the Fock state occupation of the i, j corresponding channels.

4.1.3 The heralding condition

As mentioned previously, three photons will be used to herald the success of the GHZ state generation. Considering all the possible detection patterns, the gaol of the following demonstration is to show that the heralding condition will lead to the generation of a state belonging to the GHZ class:

> Defining three subsets of heralding channels, $H_1 = \{1, 12\}$, $H_2 = \{4, 5\}$, $H_3 = \{8, 9\}$, the detection of **one and only one** photon in each subset leads to the generation of a 3-qubits entangled state belonging to the GHZ state class.

From this definition, there are eight possible detection patterns that satisfy the heralding condition. The heralding channels being $\{1, 4, 5, 8, 9, 12\}$, we can write the possible

states that satisfy our heralding condition:

$$|1_4 0_5 1_8 0_9 1_{12} 0_1\rangle = |h_1\rangle\,, \quad |0_4 1_5 1_8 0_9 1_{12} 0_1\rangle = |h_2\rangle\,, \tag{4.4}$$
$$|1_4 0_5 0_8 1_9 1_{12} 0_1\rangle = |h_3\rangle\,, \quad |0_4 1_5 0_8 1_9 1_{12} 0_1\rangle = |h_4\rangle\,, \tag{4.5}$$
$$|1_4 0_5 1_8 0_9 0_{12} 1_1\rangle = |h_5\rangle\,, \quad |0_4 1_5 1_8 0_9 0_{12} 1_1\rangle = |h_6\rangle\,, \tag{4.6}$$
$$|1_4 0_5 0_8 1_9 0_{12} 1_1\rangle = |h_7\rangle\,, \quad |0_4 1_5 0_8 1_9 0_{12} 1_1\rangle = |h_8\rangle\,. \tag{4.7}$$

Since we do not assume the detectors to be number resolving, there is a chance of undercounting the number of photon in the heralding channels. However, we will see that undercounting events leads necessarily to missing photons in the GHZ qubit channels. Thus one can discard those events by post-selecting the output state that have at least three photons.

4.2 Three-photon GHZ generation: the GHZ factory

We will now describe the evolution of a specific input state and, given the heralding detection pattern, show how one can recover a GHZ state. First we will briefly discuss the main assumption used for our demonstration. To carry out our analysis, we will break down the device in smaller parts, as shown in Fig 4.2. Along the calculation, we will discard the states that will not satisfy that heralding condition, leading to great simplifications. Finally we will show that the eight different good heralding patterns will lead to different output state that all belong to the GHZ class.

Throughout the demonstration, we assume that the circuit does not suffer from photon losses. In practice, this means that we will post-select all the states that conserve the photon number.

4.2.1 Circuit decomposition and notations

In Fig 4.2 we present an unfolded version of our design. One can notice the periodic symmetry of the device, since the channels 1 and 12 are linked together. We break down the device into several identical constitutive parts, which we will refer as *blending components* as they blend the two separated single identical photons together.

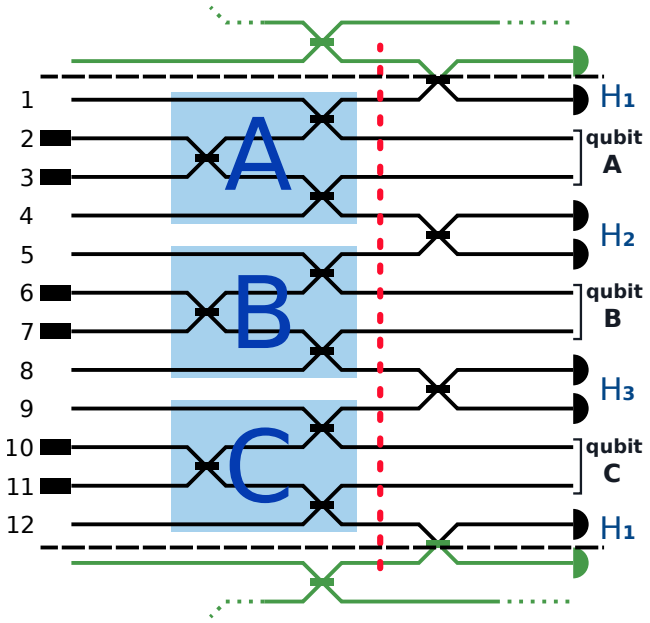

Figure 4.2: Representation of the GHZ-factory displaying the periodicity and the blending component decomposition. The three squared parts are the so-called blending components and are labelled A,B,C. We define the output qubit states A,B,C, such as $|0,1\rangle_X$, with X =A,B,C. The herald subsets of channels are referred as $H_{1,2,3}$, where H_1 = {1,12}, H_2 = {4,5}, H_3 = {8,9}. The dotted vertical line marks the place in the device where we define the middle state, $|\text{Middle}\rangle$, see sec. 4.2.3.

For the device to work, we must input the identical photons in channels {2,3,6,7,10,11}, and remind then definition of the output qubits:

$$|\text{Input}\rangle \quad : \quad |1_2 1_3 1_6 1_7 1_{10} 1_{11}\rangle$$

$$\begin{aligned} |\text{Output qubit}\rangle \quad : \quad & |0\rangle_A = |0_2 1_3\rangle\,, \quad |1\rangle_A = |1_2 0_3\rangle \\ & |0\rangle_B = |0_6 1_7\rangle\,, \quad |1\rangle_B = |1_6 0_7\rangle \\ & |0\rangle_C = |0_{10} 1_{11}\rangle\,, \quad |1\rangle_C = |1_{10} 0_{11}\rangle \end{aligned}$$

where the A,B,C indices correspond to qubit that outputs from the A,B,C blending components, see Fig 4.2.

4.2.2 Output state of a blending component

The input photon scheme for our device is $|\text{Input}\rangle = |11\rangle_{2,3} \otimes |11\rangle_{6,7} \otimes |11\rangle_{10,11} = |011001100110\rangle$. If we zoom-in at the scale of one blending component, we define the reduced input state,

$$|\text{Input}\rangle_{A,B,C} = |0110\rangle\,, \tag{4.8}$$

which enters the reduced device. We will then refer to a generic blending component as $X = A, B, C$, and we will number the channel $i = 1, 2, 3, 4$ relatively to the reduced device.

The evolution of the photon state is given by how the field operators $\hat{a}_i$, $\hat{a}_i^\dagger$ (respectively the annihilation and creation operator) transform throughout the device, where i is the considered spatial mode. For the four considered modes, we define the vector of operators, $\hat{\mathbf{a}} = (\hat{a}_1, \ldots, \hat{a}_4)$. As introduced in Chapter 1, the action of the blending component is the transformation performed by a 4×4 optical network on the creation/annihilation vector. Thus we have,

$$\hat{\mathbf{a}}_{in}^\dagger = U_{\mathrm{bc}}^t \, \hat{\mathbf{a}}_{out}^\dagger, \tag{4.9}$$

where t indicates the transposition of a matrix, and U_{bc} is the transformation matrix that the **b**lending **c**omponent operates on the field operators while $\hat{\mathbf{a}}^\dagger$ is a column vector. Then the crossed intersections in Fig 4.3 represent balanced beam splitter, already described in Chapter 1.

The full transformation matrix of the blending component reads:

$$U_{\mathrm{bc}}^t = \frac{1}{\sqrt{2}} \begin{pmatrix} 1 & 0 & 0 & 0 \\ 0 & 1 & i & 0 \\ 0 & i & 1 & 0 \\ 0 & 0 & 0 & 1 \end{pmatrix} \cdot \frac{1}{\sqrt{2}} \begin{pmatrix} 1 & i & 0 & 0 \\ i & 1 & 0 & 0 \\ 0 & 0 & 1 & i \\ 0 & 0 & i & 1 \end{pmatrix}, \tag{4.10}$$

$$= \frac{1}{2} \begin{pmatrix} \sqrt{2} & i\sqrt{2} & 0 & 0 \\ i & 1 & i & -1 \\ -1 & i & 1 & i \\ 0 & 0 & i\sqrt{2} & \sqrt{2} \end{pmatrix}. \tag{4.11}$$

Since we inject the photons in the input 2 and 3 of each blending device, see eq (4.8), let us then explicitly calculate the transformation of the creation operators $\hat{a}_{2,in}^\dagger$, $\hat{a}_{3,in}^\dagger$:

$$\hat{a}_{2,in}^\dagger \to \left(i\hat{a}_{1,out}^\dagger + \hat{a}_{2,out}^\dagger + i\hat{a}_{3,out}^\dagger - \hat{a}_{4,out}^\dagger \right), \tag{4.12}$$

$$\hat{a}_{3,in}^\dagger \to \left(-\hat{a}_{1,out}^\dagger + i\hat{a}_{2,out}^\dagger + \hat{a}_{3,out}^\dagger + i\hat{a}_{4,out}^\dagger \right). \tag{4.13}$$

Considering the input state of a blending component, we can write,

$$|\mathrm{In}\rangle_X = \hat{a}_{2,in}^\dagger \hat{a}_{3,in}^\dagger \, |0000\rangle \, . \tag{4.14}$$

Now, substituting eq.(4.12) and (4.13) into eq (4.14), developing the parenthesis and employing the definition of the creation operators (eq. 1.21), one can readily calculate the output state of each blending device:

$$|\text{Out}\rangle_X = \frac{i\sqrt{2}}{4}\Big(|0200\rangle - |2000\rangle + |0020\rangle - |0002\rangle\Big) - \frac{1}{2}\Big(|1100\rangle + |0011\rangle\Big). \tag{4.15}$$

In Fig 4.3, we illustrate the superposition of the output state and their associated coefficients.

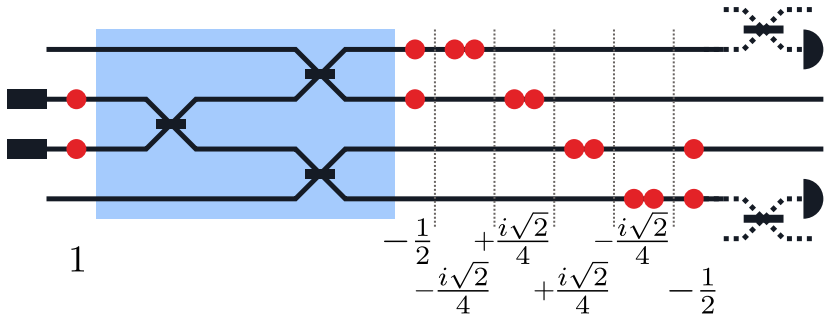

Figure 4.3: Zoom-in on a blending component of the GHZ-factory. The red dots represent the single photon states in the channel. Each vertical section represents a possible state, with its associated coefficient below.

4.2.3 Circuit middle state and post-selection

If we put together all the blending components, the middle output state is formally $|\text{Middle}\rangle = |\text{Out}\rangle_A \otimes |\text{Out}\rangle_B \otimes |\text{Out}\rangle_C$. Developing the previous expression leads to a very complicated state that is unpractical to deal with. Thus we discard the states that will not satisfy the heralding condition.

Concerning the states, $|2000\rangle_X$, $|0002\rangle_X$, they will necessarily produce two photons in the herald channels. As discussed in Sec 4.1.3, without number-resolving detectors, those states can produce a false positive of the heralding condition. However when this event happens, the number of photons in the output qubit X channels is zero. Therefore, discarding all output states with a photon number lower than three for the qubits, also discard false positive heraldings. Now regarding the states, $|0200\rangle_X$, $|0020\rangle_X$, there are no photons coming in the detection channels from

the blending component. Still, there may be a photon coming from the neighbouring sub-device. Nevertheless, one can check that there are no combinations of the other states that give a correct heralding condition. As an example,

$$|\not{0}200\rangle_A\,|1100\rangle_B\,|110\not{0}\rangle_C\,, \tag{4.16}$$
$$|0200\rangle_A\,|110\not{0}\rangle_B\,|\not{0}011\rangle_C\,. \tag{4.17}$$

where the green-colored numbers correspond to a good heralding [2] in the given channel, and red-crossed ones correspond to a wrong one. Having discarded all the non-heralding states, we are left with the middle state (red dotted line in Fig 4.2),

[2] We remind that a good heralding is when there is one and only one photon in the couples of measurement channels, {1,12},{4,5},{8,9}, as defined in sec. 4.1.3.

$$|\text{Middle}\rangle = \left(\frac{|1100\rangle + |0011\rangle}{2}\right)_A \otimes \left(\frac{|1100\rangle + |0011\rangle}{2}\right)_B \otimes \left(\frac{|1100\rangle + |0011\rangle}{2}\right)_C . \tag{4.18}$$

Using the channel labelling, reminded in Fig 4.2, we can write,

$$|\text{Middle}\rangle = \frac{1}{8}\Big(\,|1_1 1_2 0_3 0_4\rangle + |0_1 0_2 1_3 1_4\rangle\,\Big) \otimes \Big(\,|1_5 1_6 0_7 0_8\rangle + |0_5 0_6 1_7 1_8\rangle\,\Big) \otimes \Big(\,|1_9 1_{10} 0_{11} 0_{12}\rangle + |0_9 0_{10} 1_{11} 1_{12}\rangle\,\Big)\,. \tag{4.19}$$

To continue discarding un-needed states, let us consider for a moment the combination of the blending component A and B output states, *i.e.* we will focus on the development of the first two factors in eq (4.19). We get the four states:

$$\frac{1}{4}\Big(\,|1_1 1_2 0_3 0_4 1_5 1_6 0_7 0_8\rangle + |0_1 0_2 1_3 1_4 0_5 0_6 1_7 1_8\rangle + |0_1 0_2 1_3 1_4 1_5 1_6 0_7 0_8\rangle + |1_1 1_2 0_3 0_4 0_5 0_6 1_7 1_8\rangle\,\Big) \tag{4.20}$$

The two last terms can be discarded, as they don't satisfy the heralding condition, since they result in having either two photons in heralding channels 4,5 (H_2 in Fig 4.2) or they have none. In the case of two photons, we could still herald one and have a photon in the two qubit channels A

and B. However, taking into account the last blending component, there are again no combinations that leads either to a good heralding or to a three photons output. A similar procedure can be applied to the other terms of eq (4.19), resulting in:

$$|\text{Middle}\rangle = \frac{1}{8}\Big(|1_1 1_2 0_3 0_4 1_5 1_6 0_7 0_8 1_9 1_{10} 0_{11} 0_{12}\rangle + |0_1 0_2 1_3 1_4 0_5 0_6 1_7 1_8 0_9 0_{10} 1_{11} 1_{12}\rangle \Big) \tag{4.21}$$

4.2.4 Final output

We will now consider the effect of the last stage of the device. The action of the beam splitter, BS_{ij} in the middle state, *i.e.* a beam splitter between the channels i and j, is given by:

$$|1_i 0_j\rangle \xrightarrow{\text{BS}_{ij}} \frac{1}{\sqrt{2}}\left(|1_i 0_j\rangle + i\,|0_i 1_j\rangle\right), \tag{4.22}$$

$$|1_i 1_j\rangle \xrightarrow{\text{BS}_{ij}} \frac{i}{\sqrt{2}}\left(|2_i 0_j\rangle + |0_i 2_j\rangle\right). \tag{4.23}$$

Note that eq (4.23) is the photon bunching effect.

The last part of the device is then the direct application of the three beam splitters: $\text{BS}_{4,5}$, $\text{BS}_{8,9}$, $\text{BS}_{1,12}$. We thus get the expression for the final state:

$$\begin{aligned}|\text{Out}\rangle = \frac{1}{\mathcal{N}}\Big(& |1_2 0_3\rangle \Big[|0_4 1_5\rangle + i\,|1_4 0_5\rangle\Big] \\ & \otimes |1_6 0_7\rangle \Big[|0_8 1_9\rangle + i\,|1_8 0_9\rangle\Big] \\ & \otimes |1_{10} 0_{11}\rangle \Big[|0_{12} 1_1\rangle + i\,|1_{12} 0_1\rangle\Big] \\ + & |0_2 1_3\rangle \Big[|1_4 0_5\rangle + i\,|0_4 1_5\rangle\Big] \\ & \otimes |0_6 1_7\rangle \Big[|1_8 0_9\rangle + i\,|0_8 1_9\rangle\Big] \\ & \otimes |0_{10} 1_{11}\rangle \Big[|1_{12} 0_1\rangle + i\,|0_{12} 1_1\rangle\Big] \Big),\end{aligned} \tag{4.24}$$

where $\mathcal{N} = 8\sqrt{2}^3 = 16\sqrt{2}$, is the normalisation constant. One can identify the output qubit

states, $|1_2 0_3\rangle\,|1_6 0_7\rangle\,|1_{10} 0_{11}\rangle$ as $|10\rangle_A\,|10\rangle_B\,|10\rangle_C$, and $|0_2 1_3\rangle\,|0_6 1_7\rangle\,|0_{10} 1_{11}\rangle$ as $|01\rangle_A\,|01\rangle_B\,|01\rangle_C$, which are nothing else than the output logical qubit states: $|111\rangle_L$ and $|000\rangle_L$.

Re-arranging terms of the final heralded output state, we retrieve a more meaningful expression. First we write,

$$|\text{Out}\rangle = \frac{1}{\mathcal{N}}\Big(|111\rangle_L\Big[|0_4 1_5\rangle + i\,|1_4 0_5\rangle\Big]\Big[|0_8 1_9\rangle + i\,|1_8 0_9\rangle\Big]\Big[|0_{12} 1_1\rangle + i\,|1_{12} 0_1\rangle\Big] + |000\rangle_L\Big[|1_4 0_5\rangle + i\,|0_4 1_5\rangle\Big]\Big[|1_8 0_9\rangle + i\,|0_8 1_9\rangle\Big]\Big[|1_{12} 0_1\rangle + i\,|0_{12} 1_1\rangle\Big] \tag{4.25}$$

We then group each term with respect to the heralding patterns and use the notation already introduced in sec. 4.1.3, $|h_i\rangle_{i=1,\dots,8}$. Doing so, we now understand what we expect from each detection pattern.

$$\begin{aligned}|\text{Out}\rangle = \frac{1}{\mathcal{N}}\Big(&\Big[-i\,|111\rangle_L + |000\rangle_L\Big]|h_1\rangle + \Big[-|111\rangle_L + i\,|000\rangle_L\Big]|h_2\rangle \\ &+\Big[-|111\rangle_L + i\,|000\rangle_L\Big]|h_3\rangle + \Big[+i\,|111\rangle_L - |000\rangle_L\Big]|h_4\rangle \\ &+\Big[-|111\rangle_L + i\,|000\rangle_L\Big]|h_5\rangle + \Big[+i\,|111\rangle_L - |000\rangle_L\Big]|h_6\rangle \\ &+\Big[+i\,|111\rangle_L - |000\rangle_L\Big]|h_7\rangle + \Big[+|111\rangle_L - i\,|000\rangle_L\Big]|h_8\rangle\Big).\end{aligned} \tag{4.26}$$

At first glance, the output qubit state do not resemble the GHZ one. Nonetheless it still belongs to the same class. For instance, by applying a $\frac{\pi}{2}$-phase shift at the output of the even output channels {2,6,10}, we get that $|111\rangle_L$ transforms into $-i\,|111\rangle_L$, while $|000\rangle_L$ stays unchanged. We then have the following expression for the output state,

$$\begin{aligned}|\text{Out}\rangle = \frac{1}{16}\Big(&-|\text{GHZ}^-\rangle\,|h_1\rangle + |\text{GHZ}^-\rangle\Big[|h_4\rangle + |h_6\rangle + |h_7\rangle\Big] \\ &-i\,|\text{GHZ}^+\rangle\,|h_8\rangle + i\,|\text{GHZ}^+\rangle\Big[|h_2\rangle + |h_3\rangle + |h_5\rangle\Big]\Big),\end{aligned} \tag{4.27}$$

where we denoted, $|\text{GHZ}^\pm\rangle = \frac{1}{\sqrt{2}}(|111\rangle_L \pm |000\rangle_L)$. Therefore depending on the heralding measurement, one gets GHZ^+ or GHZ^- at the output. In principle, one can manipulate a GHZ state to go from $|\text{GHZ}^-\rangle$ to $|\text{GHZ}^+\rangle$, simply by adding a π-phase shift to the channels (in our case the {3,7,11} ones). However this should be implemented

dynamically as a post-processing scheme conditioned with respect to the detection pattern. This poses no fundamental issues regarding the theoretical feasibility as all the needed components already exist. Fig 4.4 shows what a final GHZ factory could look-like.

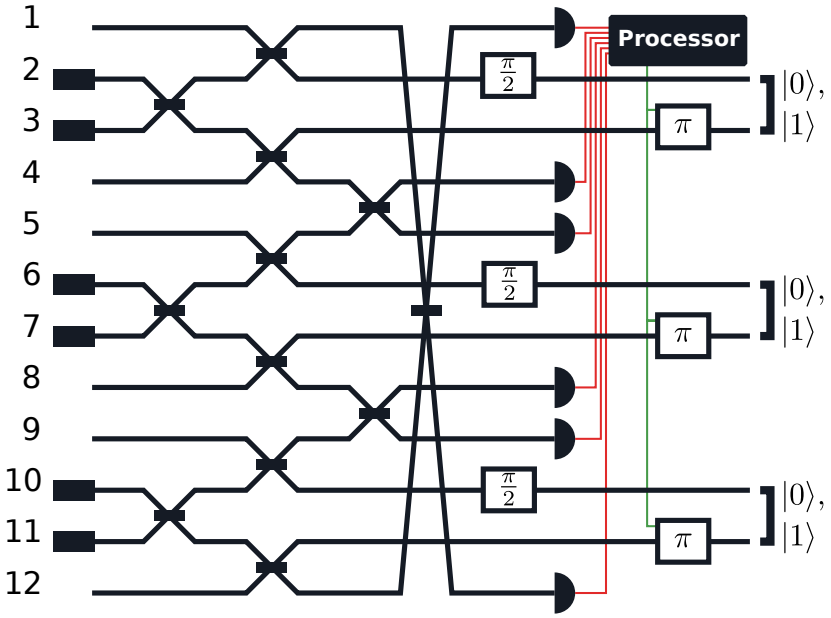

Figure 4.4: Improved version of scheme in Fig 4.1. We implement a dynamical phase-shift that activate or not a π-shift according to the heralding pattern. Depending on how fast the processing units is, one might need to add some delay lines. Moreover one would want to replace the π-shift by a $\pm\frac{\pi}{2}$ phase shift, allowing to remove the $\frac{\pi}{2}$ shift in channels {2,6,10}.

Making this demonstration allowed us to adapt the scheme for the design part as well as to propose a generalisation of the scheme to N-qubits GHZ state generation. Although not central for the development of our integrated photonic device, we consider such theoretical extension worth of explicit description, and it is reported in the following section.

4.3 Generalistion to N-photon GHZ generation

The 3-qubits GHZ state can be generalised to the N-qubit case by writing,

$$|\text{N-GHZ}\rangle = \frac{1}{\sqrt{2}}\left(|1\rangle_L^{\otimes N} + |0\rangle_L^{\otimes N}\right). \tag{4.28}$$

We want to show that under similar heralding condition than in sec. 4.1.3, an extended design can produce such N-qubits maximally entangled state.

4.3.1 Generic blending component

We start our discussion assuming we know the output state of a generic blending component. We consider a repetition of $N \geq 3$ blending components labeled $X_{k=1,\dots,N}$, where the extremities are connected. In other words we close the series to make it periodic, having $X_{N+1} \equiv X_1$ or equivalently $X_0 \equiv X_N$. The channels are now labeled with respect to their blending component. For instance the four channel of blending component X_k will be labeled: $1_k, 2_k, 3_k, 4_k$ from top to bottom. See Fig 4.5 for the notations.

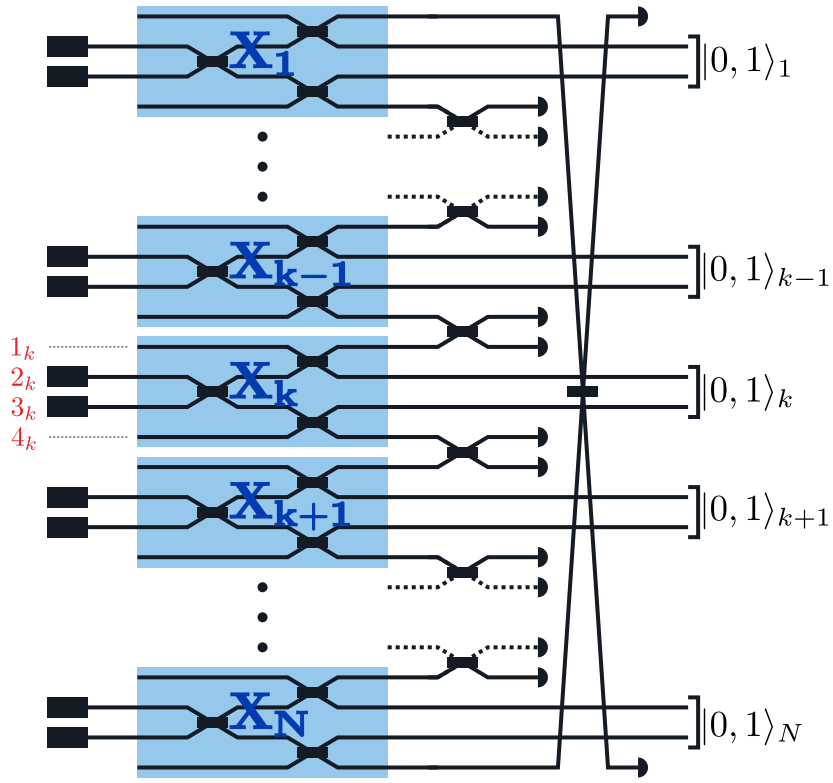

Figure 4.5: Extended version of our GHZ generator for N-qubits. We multiply the number of blending components and connect the extremities of the device. For each blending component X_k, the two central channels encode the photonic qubit $|0\rangle_{L,k}$, $|1\rangle_{L,k}$. Two adjacent blending components are connect with a beam splitter and we define the heralding qubit $|0,1\rangle_{L,k+1/2}$ for the components X_k and X_{k+1}.

Thus, one can compute the output of the blending component by expressing the input state with its creation oper-

ators:

$$|\text{in}\rangle_{X_k} = |0_{1_k} 1_{2_k} 1_{3_k} 0_{4_k}\rangle = |0110\rangle_k \tag{4.29}$$

$$\downarrow U_{bc}^t$$

$$|\text{out}\rangle_{X_k} = \frac{1}{4}\Big(-i\sqrt{2}\,|2000\rangle_k - 2\,|1100\rangle_k + i\sqrt{2}\,|0200\rangle_k \tag{4.30}$$

$$+i\sqrt{2}\,|0020\rangle_k - 2\,|0011\rangle_k - i\sqrt{2}\,|0002\rangle_k\Big).$$

4.3.2 Post-selection

We follow the same discussion of sec.4.2.3, in order to discard the state that would necessarily leads to wrong heralding. Our heralding condition states: the detection of one and only one photon in each subset $\{4_{k-1}, 1_k\}_{k=1,\ldots,N}$, leads to the generation of a N-qubits entangled state belonging to the GHZ state class.

Considering an arbitrary blending component X_k, the modes 1_k, 4_k will lead to a detection. Thus, we already see that the states $|2000\rangle_k$ and $|0002\rangle_k$ will not herald correctly. Now concerning the states $|0200\rangle_k$, $|0020\rangle_k$, it is not trivial that they will also lead to wrong heralding since one can think that the missing photons in modes 1_k, 4_k could be provided by the adjacent blending components. Let us consider the state $|0200\rangle_k$ and all the possible combination of its adjacent blending component X_{k+1}.

$$|0200\rangle_k\,|1100\rangle_{k+1}, \qquad |0200\rangle_k\,|0011\rangle_{k+1}, \tag{4.31}$$

$$|0200\rangle_k\,|0200\rangle_{k+1}, \qquad |0200\rangle_k\,|0020\rangle_{k+1}, \tag{4.32}$$

$$\tag{4.33}$$

The only combination of states that could lead to good heralding is given by the first term, $|0200\rangle_k\,|1100\rangle_{k+1}$, because one unique photon will be present in the detections channels $\{4_k, 1_{k+1}\}$. Now let assume this state is part of a good heralding global state. Because there is still a missing photons for the detection channels 4_{k+1}, for the heralding condition to be satisfied, the next neighbouring blending components state must be $|1100\rangle_{k+2}$. Thus we have one and only one photon in the detection channels $\{4_{k+1}, 1_{k+2}\}$. But then again, there is a missing photon in mode 4_{k+2}. Iterating the reasoning, we arrive at the point where the blending

components X_{k+N} state must also be $|0011\rangle_{k+N}$. Because our design is periodic, $X_{k+N} \equiv X_k$, meaning the state provided at blending component X_k must be $|0011\rangle_k \neq |0200\rangle_k$. We arrive at a contradiction. As a result, our assumption that $|0200\rangle_k |1100\rangle_{k+1}$ being part of a good heralding output state is false. Same discussion for the other neighbouring component, with the state $|0011\rangle_{k-1} |0200\rangle_k$. We also can repeat the discussion with the blending component state $|0020\rangle_k$.

In the end we can discard the states $|2000\rangle_k$, $|0002\rangle_k$, $|0200\rangle_k$, $|0020\rangle_k$, and the only valid output state for any blending component $X_{k=1,\dots,N}$ is,

$$|\text{out}\rangle_{X_k} = -\left(\frac{|1100\rangle_k + |0011\rangle_k}{2}\right) = -\left(\frac{|1100\rangle + |0011\rangle}{2}\right)_{X_k}. \tag{4.34}$$

4.3.3 Middle state

Again, we put together all the blending component output states leading to a superposition of many states. Not accounting for the global sign, the middle state is given by,

$$|\text{Middle}\rangle = \left(\frac{|1100\rangle + |0011\rangle}{2}\right)_{X_1} \otimes \cdots \otimes \left(\frac{|1100\rangle + |0011\rangle}{2}\right)_{X_N}, \tag{4.35}$$

$$= \bigotimes_{k=1}^{N} \left(\frac{|1100\rangle + |0011\rangle}{2}\right)_{X_k}. \tag{4.36}$$

We continue to use the periodic symmetry in order to discard combination of state between adjacent blending components. The discussion can thus be translated with respect to the indexation. Considering the three blending components X_k, X_{k+1}, we write the combined term up to a normalisation constant,

$$(|1100\rangle_k + |0011\rangle_k) \otimes (|1100\rangle_{k+1} + |0011\rangle_{k+1}). \tag{4.37}$$

We remember that the modes, 1_k, 4_k of the kth blending component lead to detection, where the modes 1_k, 4_k are the edges of the state $|\epsilon_1\epsilon_2\epsilon_3\epsilon_4\rangle_k$, with $\epsilon_i \in \{0, 1\}$ values of

the Fock state of mode i relative to the blending component X_k. We expand eq (4.37), and separate the result in four contributions:

$$|1100\rangle_k |1100\rangle_{k+1} + |0011\rangle_k |0011\rangle_{k+1}, \tag{4.38}$$
$$|1100\rangle_k |0011\rangle_{k+1} + |0011\rangle_k |1100\rangle_{k+1}. \tag{4.39}$$

We now observe that, except from the first contribution (eq 4.38), all other terms lead either to two photons in the heralding channels, or none. Incrementing the discussion of one, and accounting for the periodic symmetry, we find out that the middle state leading to good heralding is given by,

$$\mathcal{N} \cdot |\text{Middle}\rangle = \bigotimes_{k=1}^{N} |1100\rangle_k + \bigotimes_{k=1}^{N} |0011\rangle_k, \tag{4.40}$$

where $\mathcal{N} = 2^N$ is the normalisation constant.

4.3.4 N-photon heralding output states

We now apply the last stage of beam-splitters and recover the full heralding output state for the N-qubit GHZ generation scheme,

$$\begin{aligned}\mathcal{N} \cdot |\text{Out}\rangle &= \bigotimes_{k=1}^{N} |1_2 0_3\rangle_k \left[\frac{|0_{4_k} 1_{1_{k+1}}\rangle + i\,|1_{4_k} 0_{1_{k+1}}\rangle}{\sqrt{2}}\right] \\ &+ \bigotimes_{k=1}^{N} |0_2 1_3\rangle_k \left[\frac{|1_{4_k} 0_{1_{k+1}}\rangle + i\,|0_{4_k} 1_{1_{k+1}}\rangle}{\sqrt{2}}\right] \qquad (4.41)\\ &= \left(\bigotimes_{k=1}^{N} |1_2 0_3\rangle_k\right)\left(\bigotimes_{k=1}^{N}\left[\frac{|0_{4_k} 1_{1_{k+1}}\rangle + i\,|1_{4_k} 0_{1_{k+1}}\rangle}{\sqrt{2}}\right]\right) \\ &+ \left(\bigotimes_{k=1}^{N} |0_2 1_3\rangle_k\right)\left(\bigotimes_{k=1}^{N}\left[\frac{|1_{4_k} 0_{1_{k+1}}\rangle + i\,|0_{4_k} 1_{1_{k+1}}\rangle}{\sqrt{2}}\right]\right) \qquad (4.42)\end{aligned}$$

$$\begin{aligned}\sqrt{2}^{N-1}\mathcal{N} \cdot |\text{Out}\rangle &= \left(\sqrt{2}^{-1}\bigotimes_{k=1}^{N} |1\rangle_{L,k}\right)\left(\bigotimes_{k=1}^{N}\left[|0\rangle_{L,k+1/2} + i\,|1\rangle_{L,k+1/2}\right]\right) \\ &+ \left(\sqrt{2}^{-1}\bigotimes_{k=1}^{N} |0\rangle_{L,k}\right)\left(\bigotimes_{k=1}^{N}\left[|1\rangle_{L,k+1/2} + i\,|0\rangle_{L,k+1/2}\right]\right) \qquad (4.43)\end{aligned}$$

where in the last line we express the photon states in term of the blending component qubit state $|0\rangle_{L,k}$, $|1\rangle_{L,k}$. We also use the encoding of a *heralding qubit* from two adjacent blending components X_k, X_{k+1} which is written as $|0\rangle_{L,k+1/2}$, $|1\rangle_{L,k+1/2}$ and encoded as follow,

$$|0\rangle_{L,k+1/2} = \left|0_{4_k}1_{1_{k+1}}\right\rangle \qquad |1\rangle_{L,k+1/2} = \left|1_{4_k}1_{0_{k+1}}\right\rangle. \tag{4.44}$$

We reminding that $X_{N+1} \equiv X_1$. The following is a reorganisation of terms. Indeed developing the N-product of the square parenthesis we arrive to a sum of many permutations of the single photon state in two spatial modes. We make use of the heralding qubits to encode those states and facilitate the writing of the final expression. We define the heralding detection pattern state, as the combination of one heralding qubit resulting after a measurement. We write it,

$$|\mathrm{h}_{\boldsymbol{\epsilon}}\rangle = \bigotimes_{k=1}^{N} |\epsilon_k\rangle_{L,k+1/2} = |\boldsymbol{\epsilon}\rangle_L, \tag{4.45}$$

where $\boldsymbol{\epsilon} = (\epsilon_1, \ldots, \epsilon_N$, with $\epsilon_i \in \{0,1\}$ for $i = 1, \ldots, N$. Defining $\sigma_{\boldsymbol{\epsilon}} = \sum_{k=1}^{N} \epsilon_k$, we can regroup the terms in the final output sate with respect the heralding detection pattern,

$$\begin{aligned}\sqrt{2}^{N-1}\mathcal{N}\cdot|\mathrm{Out}\rangle = \sum_{\boldsymbol{\epsilon}} \Bigg[&\frac{1}{\sqrt{2}} |1\rangle_L^{\otimes N} i^{\sigma_{\boldsymbol{\epsilon}}} |\mathrm{h}_{\boldsymbol{\epsilon}}\rangle \\ &+ \frac{1}{\sqrt{2}} |0\rangle_L^{\otimes N} i^{N-\sigma_{\boldsymbol{\epsilon}}} |\mathrm{h}_{\boldsymbol{\epsilon}}\rangle \Bigg]\end{aligned} \tag{4.46}$$

$$\sqrt{2}^{N-1}\mathcal{N}\cdot|\mathrm{Out}\rangle = \sum_{\boldsymbol{\epsilon}} i^{\sigma_{\boldsymbol{\epsilon}}} \left(\frac{|1\rangle_L^{\otimes N} + (-1)^{\sigma_{\boldsymbol{\epsilon}}} i^N |0\rangle_L^{\otimes N}}{\sqrt{2}} \right) |\mathrm{h}_{\boldsymbol{\epsilon}}\rangle. \tag{4.47}$$

Defining the more general N-qubits GHZ state,

$$|\text{N-GHZ}(\Phi)\rangle = \sqrt{2}^{1} \left(|1\rangle_L^{\otimes N} + e^{i\Phi} |0\rangle_L^{\otimes N} \right), \tag{4.48}$$

the heralded output state of the extended device is then,

$$|\mathrm{Out}\rangle = \frac{1}{\sqrt{2}^{N-1}\mathcal{N}} \sum_{\boldsymbol{\epsilon}} i^{\sigma_{\boldsymbol{\epsilon}}} \left| \text{N-GHZ}\left(\frac{\pi}{2}(N - 2\sigma_{\boldsymbol{\epsilon}}) \right) \right\rangle |\mathrm{h}_{\boldsymbol{\epsilon}}\rangle, \tag{4.49}$$

where $\mathcal{N} = 2^N$, $\boldsymbol{\epsilon} = (\epsilon_1, \ldots, \epsilon_N)$, $\sigma_{\boldsymbol{\epsilon}} = ||\boldsymbol{\epsilon}||$, and $\epsilon_{i=1,\ldots,N} \in \{0,1\}$.

4.3.5 General results

Apart from predicting the intrinsic relative phase between $|1\rangle_L^{\otimes N}$ and $|0\rangle_L^{\otimes N}$ with respect to the heralding pattern, we can compute the theoretical efficiency of the GHZ factory. The number of good heralding detection event is 2^N. Thus the success rate is given by,

$$p_N = \frac{2^N}{(\sqrt{2}^{N-1}\mathcal{N})^2} = \frac{1}{2^{2N-1}}. \tag{4.50}$$

We see that the success rate of such protocol, is exponentially decreasing with the number of qubits,$p_N = 2^{-2N+1}$. Coming back to the value of N. Our scheme also works for $N = 1$ producing a diagonal state $|+\rangle$, and for $N = 2$, which gives a Bell state.

4.4 Phase shift sensitivity

Now let us consider the effect of random phases in the circuits. Indeed, the fabrication process holds some variabilities that can lead to spurious phase shifts in the optical circuit. In this discussion we turn back to the 3-qubit GHZ factory scheme. First we will focus on the output state of a blending component, and discuss the phase dependence of the state. In Fig 4.6 we introduce the different notation for the phases.

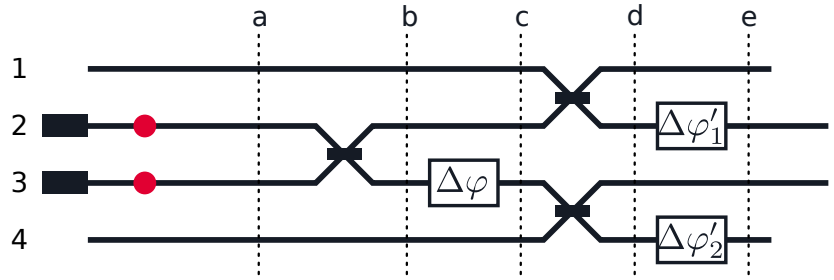

Figure 4.6: Schematic of the possible phase shifts in one blending component. The red dots are reminders of the input photons. The vertical dotted lines are the stages decomposition of the circuit in order to facilitates the study.

The scheme in Fig. 4.6, only takes into account phase differences that are relevant to our study. Indeed any phase before stage *a* will contribute to a global phase of the output state. Such global phases are not relevant to our study

as the detection for the heralding condition is only based on the photon number. Moreover, until stage d, channels 1 and 4 have no photons, thus they do not contribute to any phase difference. Finally, between stages b and c, we only consider the relative phase between the channel, since absolute phase shift are not measurable in this scheme. Likewise for stage d and e. Note that any phase difference between the channels {1,2} and channels {3,4} are absorbed in $\Delta\varphi$, the phase difference between the channels 2 and 3.

Then, following the same procedure than in sec. 4.2.2, we get the following transformation matrices for each stage,

$$P_{bc} = \begin{pmatrix} 1 & 0 & 0 & 0 \\ 0 & 1 & 0 & 0 \\ 0 & 0 & e^{i\Delta\varphi} & 0 \\ 0 & 0 & 0 & 1 \end{pmatrix}, \quad P_{de} = \begin{pmatrix} 1 & 0 & 0 & 0 \\ 0 & e^{i\Delta\varphi_1'} & 0 & 0 \\ 0 & 0 & 1 & 0 \\ 0 & 0 & 0 & e^{i\Delta\varphi_2'} \end{pmatrix}, \tag{4.51}$$

$$U_{ab} = \frac{1}{\sqrt{2}} \begin{pmatrix} \sqrt{2} & 0 & 0 & 0 \\ 0 & 1 & i & 0 \\ 0 & i & 1 & 0 \\ 0 & 0 & 0 & \sqrt{2} \end{pmatrix}, \quad U_{cd} = \frac{1}{\sqrt{2}} \begin{pmatrix} 1 & i & 0 & 0 \\ i & 1 & 0 & 0 \\ 0 & 0 & 1 & i \\ 0 & 0 & i & 1 \end{pmatrix}. \tag{4.52}$$

We now consider the transformation of the creation operators up to the stage d, as the final phase shift will be easier to implement after determining the output state. Reminding the convention $\hat{\mathbf{a}}^\dagger_{out} = U^t \hat{\mathbf{a}}^\dagger_{in}$, we get the final transformation matrix:

$$U^t = \frac{1}{2} \begin{pmatrix} \sqrt{2} & i\sqrt{2} & 0 & 0 \\ i & 1 & ie^{i\Delta\varphi} & -e^{i\Delta\varphi} \\ -1 & i & e^{i\Delta\varphi} & ie^{i\Delta\varphi} \\ 0 & 0 & i\sqrt{2} & \sqrt{2} \end{pmatrix}. \tag{4.53}$$

From the input state we get the output state by transforming the creation operators $\hat{a}_i^\dagger$ in the input to the creation operators $\hat{d}_i^\dagger$ of the output at stage d. We then obtain the output state of the blending component $X = A, B, C$ as written in eq (4.57).

$$|\text{In}\rangle_X = |0110\rangle = \hat{a}_2^\dagger \hat{a}_3^\dagger |0000\rangle\,, \tag{4.54}$$

$$|\text{Out}\rangle_X = \frac{1}{4}\left(i\hat{d}_1^\dagger + \hat{d}_2^\dagger + ie^{i\Delta\varphi}\hat{d}_3^\dagger - e^{i\Delta\varphi}\hat{d}_4^\dagger\right) \tag{4.55}$$

$$\otimes \left(-\hat{d}_1^\dagger + i\hat{d}_2^\dagger + e^{i\Delta\varphi}\hat{d}_3^\dagger + ie^{i\Delta\varphi}\hat{d}_4^\dagger\right)|0000\rangle \tag{4.56}$$

$$= \frac{i\sqrt{2}}{4}\Big(-|2000\rangle + |0200\rangle + e^{2i\Delta\varphi}|0020\rangle - e^{2i\Delta\varphi}|0002\rangle\Big) - \frac{1}{2}\left(|1100\rangle + e^{2i\Delta\varphi}|0011\rangle\right), \tag{4.57}$$

Before considering the last stage of phase shifts, we can discard the states that will not satisfy the heralding condition. Indeed, the heralding condition does not depends on the phase since the number of photon is conserved whatever the phase difference between the states. Thus, we conserve the last two states with at most one photon in each channel.

Now applying the last stage of phase shifts, *i.e.* stage $d \to e$, we get to the output state of the blending component $X = A, B, C$,

$$|\text{Out}\rangle_X = -\frac{1}{2}\left(e^{i\Delta\varphi_1'}|1100\rangle + e^{i(2\Delta\varphi+\Delta\varphi_2')}|0011\rangle\right), \tag{4.58}$$

$$= -\frac{e^{i\Theta_X}}{2}\left(|1100\rangle + e^{i(2\Delta\varphi+\Delta\varphi_2'-\Delta\varphi_1')}|0011\rangle\right), \tag{4.59}$$

where $\Theta_X = \Delta\varphi_1'$. For getting more clarity, we will denote, $\Delta\varphi_X = \Delta\varphi$, $\Delta\varphi'_{X,1} = \Delta\varphi_1'$, $\Delta\varphi'_{X,2} = \Delta\varphi_2'$ and finally, we define

$$|\overline{\text{Out}}\rangle_X = \frac{1}{2}\left(|1100\rangle + e^{i(\Delta\varphi_X - \Delta\varphi'_{X,1} + \Delta\varphi'_{X,2})}|0011\rangle\right). \tag{4.60}$$

Thus, the output state is written as,

$$|\text{Out}\rangle_X = e^{i\Theta_X}|\overline{\text{Out}}\rangle_X\,. \tag{4.61}$$

Putting together the output states of each blending component we get,

$$|\text{Middle}\rangle = e^{i(\Theta_A+\Theta_B+\Theta_C)}|\overline{\text{Out}}\rangle_A|\overline{\text{Out}}\rangle_B|\overline{\text{Out}}\rangle_C\,. \tag{4.62}$$

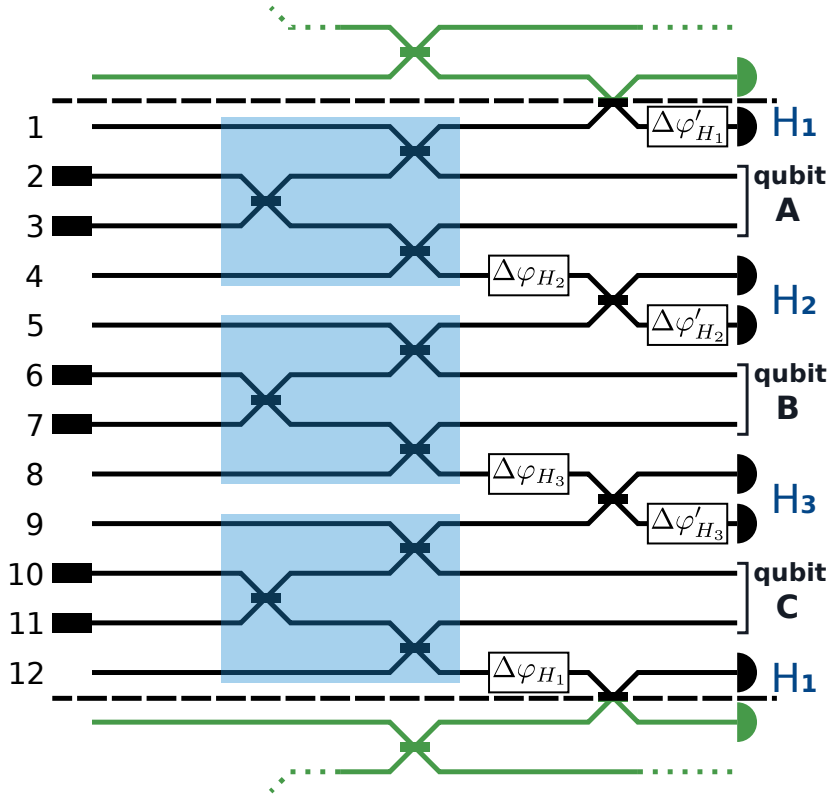

Figure 4.7: Phase shift definition for the last stage of beam splitters.

Again, we can discard the non-heralding state like in the previous discussions. Moreover since the measurements are not sensitive to any global phase of a quantum state, we will omit it in the following. We then write the middle state that satisfy the heralding condition,

$$|\text{Middle}\rangle = \frac{1}{8}\left(|110011001100\rangle + e^{i\Phi_0}|001100110011\rangle\right), \tag{4.63}$$

with $\Phi_0 = 2\Delta\varphi_A - \Delta\varphi'_{A,1} + \Delta\varphi_{A,2} + 2\Delta\varphi_B - \Delta\varphi'_{B,1} + \Delta\varphi_{B,2} + 2\Delta\varphi_C - \Delta\varphi'_{C,1} + \Delta\varphi_{C,2}$. This middle state will lead to the output state of the device after passing through the last stage of beam splitter.

In Fig 4.7, we add phase shifts in channels 1,5,9 to separate the action of the relative phase between the channels for the heralding, and the action of phase shifts in the blending components. Indeed, those phase shifts could have been absorbed in the $\Delta\varphi'_{X,2}$. However, we want to explicit the separate action of those phase shifting. Doing so, we see that any relative phase $\Delta\varphi_{H_i}$ with $i = 1,2,3$, only adds up to the total relative phase between the two

terms of the Middle state. In other words, to Φ_0 we add the phase $\Phi_H = \Delta\varphi_{H_1} + \Delta\varphi_{H_2} + \Delta\varphi_{H_3}$. The total relative phase between the two surviving states in the Middle state is: $\Phi = \Phi_0 + \Phi_H$.

We now look for the transformation of the detection pattern states when we add relative phase in the measurement channels. The heralding states without phase shift have already been defined in sec. 4.1.3. From those definitions, we can directly apply the accumulated phase shift to each heralding states, where only the $\Delta\varphi'_{H_i}$, with $i = 1, 2, 3$, will act.

$$|h_1\rangle \rightarrow \left|\overline{h_1}\right\rangle = |h_1\rangle\,, \tag{4.64}$$

$$|h_2\rangle \rightarrow \left|\overline{h_2}\right\rangle = e^{i\Delta\varphi'_{H_2}}\,|h_2\rangle\,, \tag{4.65}$$

$$|h_3\rangle \rightarrow \left|\overline{h_3}\right\rangle = e^{i\Delta\varphi'_{H_3}}\,|h_3\rangle\,, \tag{4.66}$$

$$|h_4\rangle \rightarrow \left|\overline{h_4}\right\rangle = e^{i(\Delta\varphi'_{H_2}+\Delta\varphi'_{H_3})}\,|h_4\rangle\,, \tag{4.67}$$

$$|h_5\rangle \rightarrow \left|\overline{h_5}\right\rangle = e^{i\Delta\varphi'_{H_1}}\,|h_5\rangle\,, \tag{4.68}$$

$$|h_6\rangle \rightarrow \left|\overline{h_6}\right\rangle = e^{i(\Delta\varphi'_{H_1}+\Delta\varphi'_{H_2})}\,|h_6\rangle\,, \tag{4.69}$$

$$|h_7\rangle \rightarrow \left|\overline{h_7}\right\rangle = e^{i(\Delta\varphi'_{H_1}+\Delta\varphi'_{H_3})}\,|h_7\rangle\,, \tag{4.70}$$

$$|h_8\rangle \rightarrow \left|\overline{h_8}\right\rangle = e^{i(\Delta\varphi'_{H_1}+\Delta\varphi'_{H_2}+\Delta\varphi'_{H_3})}\,|h_8\rangle\,. \tag{4.71}$$

We can write more compactly the transformation as: $\left|\overline{h_i}\right\rangle = e^{i\theta_i}\,|h_i\rangle$, with θ_i the total random phase difference. The action of the phase shifts in the heralding channels, only adds a global phase to the heralding states. Such global phase being not relevant in our case, we can set it to zero, and use again the notation $|h_i\rangle$ in the following.

After factoring the $|h_i\rangle$ in the output state, we consider the implementation of a $\frac{\pi}{2}$ phase shifter on the even qubit channel to express and write the output state in terms of GHZ states,

$$\begin{aligned}|\text{Out}\rangle = \frac{1}{16}\Big(&- \left|\text{GHZ}^-(\Phi)\right\rangle|h_1\rangle + \left|\text{GHZ}^-(\Phi)\right\rangle\Big[\,|h_4\rangle + |h_6\rangle + |h_7\rangle\Big) \\ &-i\left|\text{GHZ}^+(\Phi)\right\rangle|h_8\rangle + i\left|\text{GHZ}^+(\Phi)\right\rangle\Big[\,|h_2\rangle + |h_3\rangle + |h_5\rangle\Big]\Big)\,.\end{aligned} \tag{4.72}$$

We use the notation $\left|\mathrm{GHZ}^{\pm}(\Phi)\right\rangle = (\sqrt{2})^{-1}(|111\rangle \pm e^{i\Phi}|000\rangle)$.

All in all, the output state will still produce entangled states that fall into the GHZ class. However there will be an internal phase shift that should be corrected after characterisation. As already mentioned, we can also set to zero the phase shifts before the last beam splitter, $\Phi_H = 0$, by absorbing it in the blending component phase shifts.

In the end, and more importantly, the internal phase shift of the GHZ states is independent from the heralding pattern.

Chapter 5

Implementation of the photonic circuit

Contents

Introduction

After demonstrating the theoretical functioning of the circuit, we want to implement the scheme using femtosecond laser micromachining. In this chapter we will present the step of optimisation of the irradiation parameters leading to the design of the actual geometry of the optical circuit.

5.1 Optimisation of the irradiation parameters

5.1.1 Propagation loss and coupling losses

As a first step, we start by finding the range of parameters that allows *single mode* propagation at the wavelength of choice (904 nm). Within this range, we look for the parameter that minimises the propagation losses, see Fig 5.3. Note that over all the parameter to optimize (speed, depth below the surface, power of writing, number of scans, annealing, repetition rate), some are actually fixed by the laser source (femtosecond laser wavelength, repetition rate). Indeed, the repetition rate is set at 1 MHz, and the laser sends pulse of 350 fs at a wavelength of 1030 nm. The same objective, 50x with 0.6 NA, has been used for all fabrication and the beam was constantly centered at the lens to reduce the tilt of the focal spot (as opposed to what is done in Fig. 2.11a). In our optimisation, we varied the average power of irradiation, the depth of the focal spot in the substrate, the speed of the writing and the number of time we wrote on the same waveguide (number of scan).

As explained in chapter 2, the characterisation setup only allows for a direct measure of the insertion losses, see Fig 5.1.

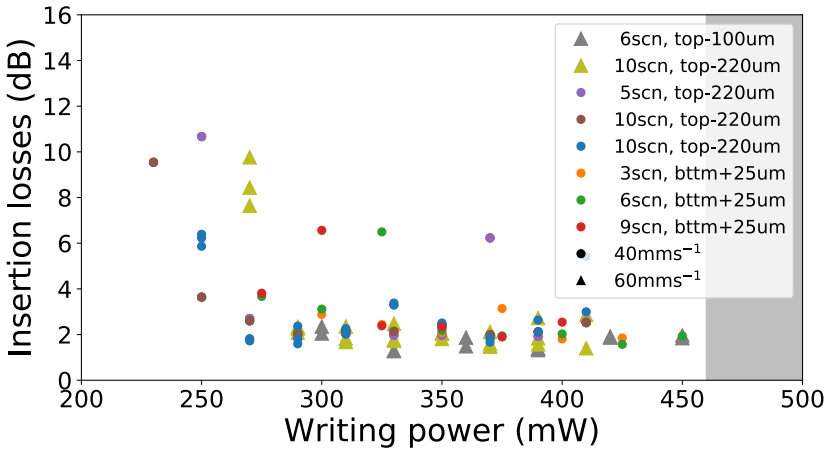

Figure 5.1: Figure showing the insertion losses as a function of the writing power for different set of parameters. Not all the data are shown to increase readability. The grey region correspond to a threshold where the propagation is no-longer single mode.

To retrieve the propagation losses, we estimate the coupling losses with the measurement of the mode profile, see

Fig 5.2a. Computing the overlap between the coupling fiber single mode and the characterised waveguide mode, we can estimate the coupling losses, see Fig 5.2b.

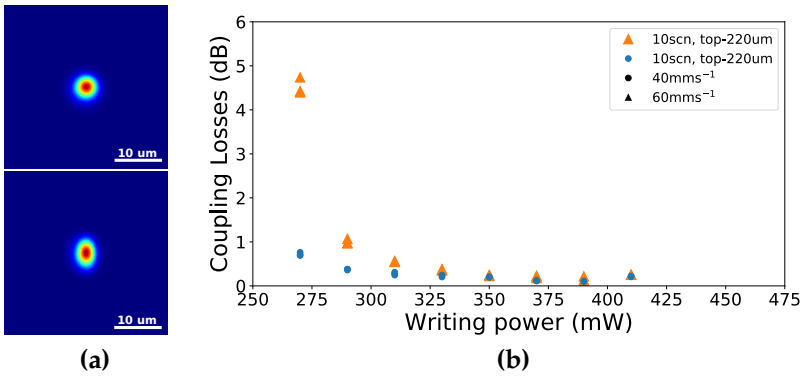

Figure 5.2: In (a) the picture of the fiber mode profile (top) and a waveguide one (bottom). We plot in (b) the evolution of the coupling losses with respect to the writing power for at a given set of parameters.

We finally remove the contribution of the coupling losses and the Fresnel losses from the insertion losses and compute the propagation losses of the fabricated waveguides in the sample of well known length, see Fig 5.3.

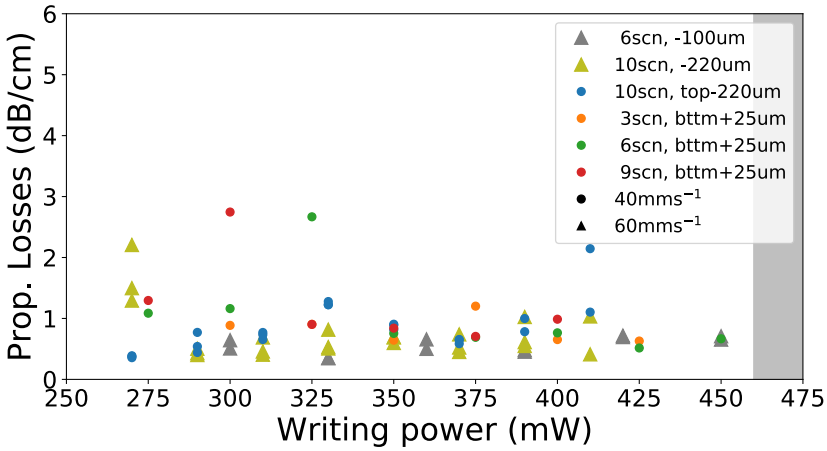

Figure 5.3: The figure shows the retrieved propagation losses of the different fabricated waveguides.

We also verify that the propagation in the waveguides is not polarization dependent. Looking at our results, we choose to keep the parameters for $PL_{min} = 0.6 \pm 0.2$dB/cm, which correspond to waveguides writing at 290 mW at -220 μm below the surface with a number of scan of 10. There is still an indetermination on the writing speed.

5.1.2 Bending losses

Given those optimum waveguides, the geometry of the design is then constrained by the bending losses, *i.e.* how much we can bend the waveguides without too much losses.

Bending losses are radiation losses due to curvatures in the propagating axe. In the curved section, the mode profile of a single mode fiber is deformed and the field is pushed toward the outer region, as in a centrifugal force effect. Consequently it increases the coupling of the guided mode with outside and introduce losses by radiation away from the core of the waveguide [28, 52, 66, 67].

For circular curvature, the losses are exponentially decreasing with the increasing radius. We choose to characterise the bending losses with this type of curvature as it is a good approximation when dealing with waveguide written in FLM.

We proceed by writing several waveguide having two identical successive circular arcs put in the form of a 'S', that we call *S-bend*. Fixing the irradiation parameters, we vary the radius of curvature, but keep the same total curved length for every S-bends. We then use the same characterisation setup than for propagation loss characterisation, and we retrieve the bending losses by discarding the propagation losses with a witness straight waveguide (as in eq (3.6)).

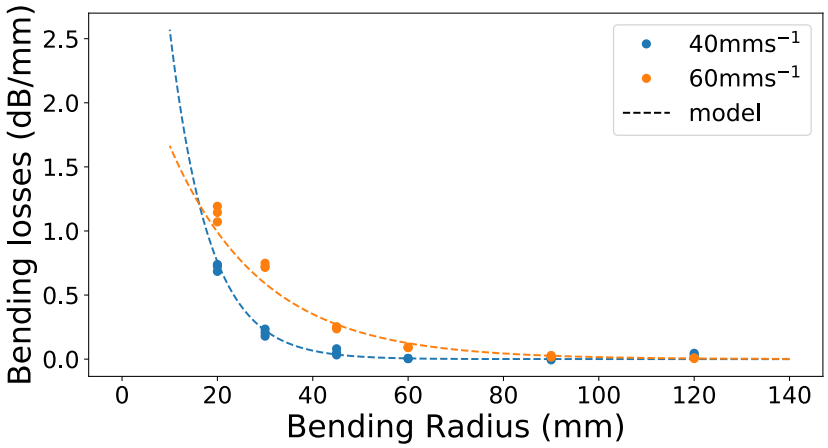

Figure 5.4: Bending losses for waveguides at -220um below surface, with 10 scan. Two writing speeds had been kept, since it was not clear which was the best set of parameter from only the propagation losses. We then choose to keep 40 mm.s^{-1}.

From our measurement, see Fig 5.4, we can discriminate

the best writing speed and keep 40 mm.s^{-1} as it allows to achieve negligible bending losses with a smaller radius. As a result, we fix the minimal radius of curvature of the design to be $R_{min} = 60$ mm.

5.1.3 Chosen parameters

In the end, we choose to write our waveguides at 220μ m under the top surface with a beam power of 290 mW, at constant writing speed of 40 mm.s^{-1}, and passing 10 times over the same waveguide (number of scan). Those numbers are summarised in Table 5.1. Moreover, we choose to anneal our sample after fabrication.

Power (mW)	depth (um)	number of scan	speed (mm/s)
290	-220	10	40

Table 5.1: Writing parameters used during the FLM.

5.2 Geometry of the implemented circuit

5.2.1 Design of the circuit geometry

Considering the 3D capability of the femtosecond laser micromachining technology, we explored different geometries with the aim of maintaining an elevated degree of footprint compactness. We came to the conclusion that having all channels input and output in the same plane was optimum for our design. The main constrain comes from a fiber array that will be use for coupling the inputs and outputs of the final design, so that the device would be usable by our collaborators. Moreover, choosing to have the directional couplers on the same plane reduces the variability and the set of parameter to optimize since the depth is fixed. Nevertheless, it is still necessary to have crossings in order to bring the outer modes together, channels 1 and 12 in Fig 4.1. We thus define a safe distance at crossings to avoid any unsought coupling. Concerning the bending shape, we decided to keep the circular S-bend when designing the directional couplers as it is more practical to implement and theoretical profile optimisation do not improve greatly the losses [73]. On the other hand, we use

optimised cubic-spline curves for bends in the Z-direction. They are optimise to keep a given safe distance while minimising the radius of curvature for each channel.

Accounting for all of those constrains, we modified the theoretical scheme in order to minimize the total length of the device. The first modification from the scheme is to keep the outer channels in the middle after the coupling. Consequently, we need to displace all other channels. The second modification is to switch the role of channels 1 and 2, as well as channels 11 and 12 after the second stage of beam-splitters allowing us to further reduce the length of the device (the numbering refers to Fig 4.1). The modification does not change the behaviour of the device. We can convince ourself about the validity of this fact by considering the middle state, $|\text{Middle}\rangle$, in the theoretical description. At this point in the theory, switching the role of the mode (1,2) or (11,12), leads to the same discussion regarding the post selection of the output state as the photon are still assumed indistinguishable.

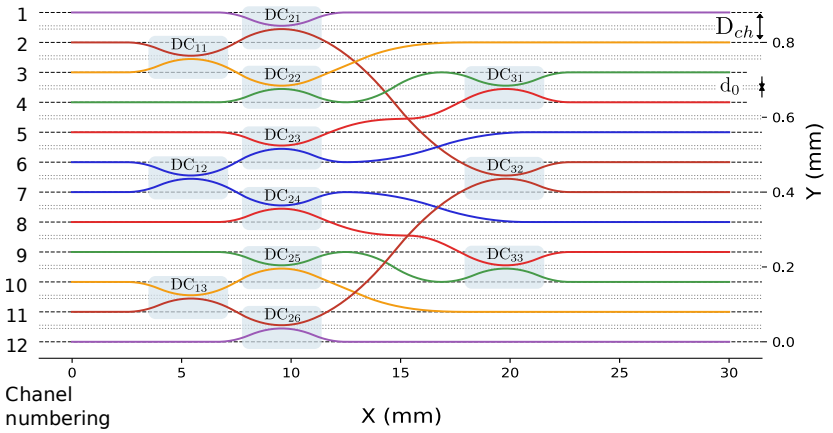

Figure 5.5: Top view of the chosen geometry for the GHZ factory circuit. The optical network is symmetric with respect to a horizontal plane between channel 6 and 7.

5.2.2 Time delays

When we design the geometrical path of the circuit, we must consider the effect of time delays between photons that do not travel the same path before interfering in the beam splitters. Although we maximized the symmetry of the circuit, the fabrication constrains lead to unbalanced channel length. Thus in order to estimate the quality of the interactions in the device, we aim to check the coincidence

time at the beam splitters.

To do so, we compute the path length of each channels as well as their minimal radius of curvature, see Table 5.2. We choose $R_{\min} = 60.0$mm as a results of optimisation in the process of fabrication.

Channel	Length (mm)	$R_{\min}$ (mm)	Channel	Length (mm)	$R_{\min}$ (mm)
CH 1	30.0006	60.0	CH 7	30.0020	60.0
CH 2	30.0111	60.0	CH 8	30.0019	60.0
CH 3	30.0023	60.0	CH 9	30.0021	60.0
CH 4	30.0021	60.0	CH10	30.0023	60.0
CH 5	30.0019	60.0	CH11	30.0111	60.0
CH 6	30.0020	60.0	CH12	30.0006	60.0.

Table 5.2: Geometric properties of the channels in the GHZ factory implementation.

Considering Fig 5.10, from the inputs to the second stage of beam splitters all the input photons will travel the same length. Likewise if we consider the straight paths after the last stage of beam-splitters. As a result, all the relevant path differences correspond to the paths between the second and last stage of beam splitters.

Looking at the channels 2 and 11, for symmetry reasons, the photons will travel the same distance before interfering at the beam splitter DC_{32}. The main consideration being for interference between channels 4 and 5, and between channels 8 and 9. When looking at Table 5.3a, the difference in length is of order of $\Delta l \simeq 0.2\mu$m, which gives a time delay of $\Delta\tau = \frac{\Delta l\, n}{c} \simeq 1.0$fs.

Now we consider the time delay between the photons from each qubit channels, *i.e.* between the pair of channels {1,3,6,7,10,12}. We get $\Delta l_{3,6} = \Delta l_{7,10} = 0.3\mu$m, $\Delta l_{1,3} = \Delta l_{10,12} = 0.9\mu$m , $\Delta l_{1,6} = \Delta l_{7,12} = 0.6\mu$m, see Table 5.3b. The maximum time spreading is thus: $\Delta T \simeq 4.5$fs.

In conclusion, the wave packet will spread over a time scale of several femtosecond. Considering the initial input wave packet of six identical photons, for which each photons have a lifetime $\tau_{lt} = 0.1$ns in the worst case (see Ref [97]), we can stay confident on the quality of the quantum interference occurring throughout the device, as the spreading is three order of magnitude below the photon wave packet size.

	$BS_{3,1}$	$BS_{3,2}$	$BS_{3,3}$
Δl (μm)	0.2	0.0	0.2

(a) Beam-splitter relative input path difference.

Δl (μm)	CH 1	CH 3	CH 6
CH 1	0.0	0.9	0.6
CH 3	0.9	0.0	0.3
CH 6	0.6	0.3	0.0

(b) Qubit channels path difference.

Table 5.3: Path difference between two input photons of the considered beam splitters, (a). We use the notation, $BS_{i,j}$, where i is the stage, *i.e.* the column, and j the line from top to bottom in Fig 5.10. In (b) the path difference between the qubit channels. For symmetry reasons, values for the channels {7, 10, 12} are identical.

5.3 Optimisation of the directional couplers

5.3.1 General optimisation

In integrated photonics, beam splitters are implemented with directional couplers. The next step of the optimization protocol is then to find the parameters that will lead to a 50:50 splitting ratio, also called 3dB directional couplers. Moreover, all the couplings have to be identical. To have similar directional couplers, we then need a safe distance that accounts for pre-coupling and let the splitting unchanged whatever the waveguide geometry before or after. Fig 5.6a shows the chosen geometry of the directional couplers. In this design, all the curved path are circular arcs of 60mm radius. The only degrees of freedom we have are the minimal coupling distance d_0 and the coupling length l. Fabricating several directional couplers with three different minimal coupling distance, we can retrieve the splitting ratio as a function of the coupling length by the theoretical $\sin^2$ evolution, see Fig 5.6b. Inputting light in mode 1, we define the differential transmission for identical waveguides is given by,

$$P_{\text{diff}} = \frac{P_{\text{out},1}}{P_{\text{out},1} + P_{\text{out},2}} = \sin^2(k(l + l_0)), \tag{5.1}$$

where $P_{\text{out},j}$ is the output power of the mode $j = 1, 2$, k is the *coupling coefficient*, and the constant l_0 account for pre-coupling effect while the waveguides come closer one to another. The differential transmission is identical to the splitting ratio.

5.3.2 Optimisation on the coupling distance

Since we want to minimise the device footprint propagation losses, we decide to optimize the directional coupler by varying the coupling distance d_0, fixing the interaction length to zero. The downside of this method is the exponential dependency of the coupling strength with respect to the distance between waveguides d. This renders the splitting ratio more sensitive to the variability of the fabrication

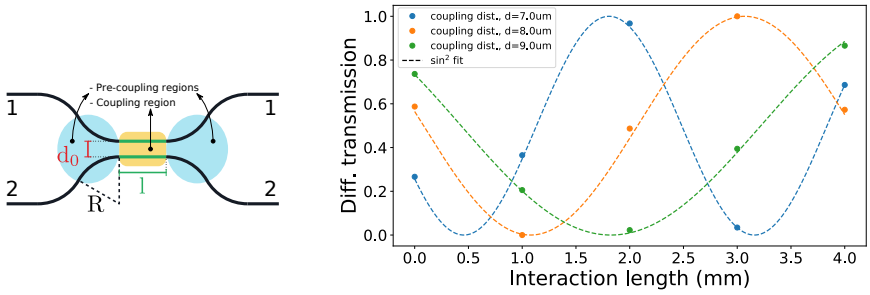

(a) (b)

Figure 5.6: The directional coupler parameters of our design are display in (a). In (b) we show the differential transmission as a function of the interaction length l for three different minimal coupling distance d_0. All the directional couplers are written at -220 um below surface, with the same radius $R = 60$ mm and a scan number of 10. We fitted the data with the theoretical expression from coupled waveguide theory.

process. However after several fabrications we can estimate the stability of the process and find out it is sufficient to obtain a reliable fabrication. The data fit the theoretical model of an exponentially dependent coupling coefficient, and it can be back simulated to recover the value of the parameters in the coupling coefficient. Fig 5.7 shows the fitted splitting ration as a function of the minimal coupling distance d_0. A better detailed explanation on the backward simulation is given in the next section.

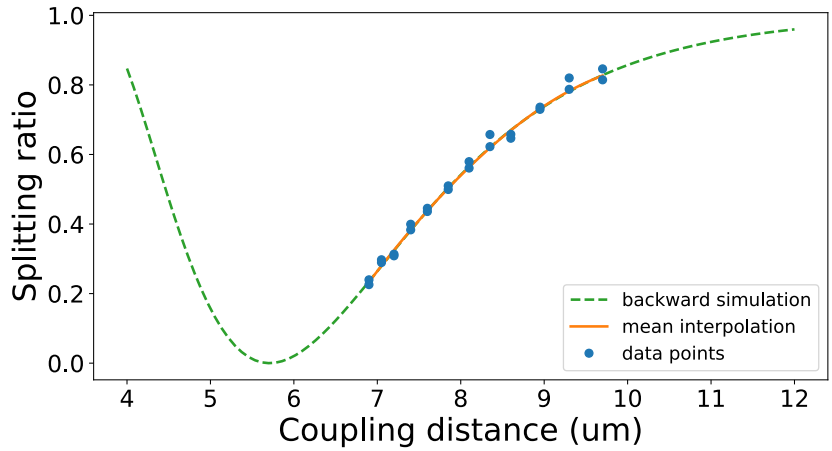

Figure 5.7: Backward simulation with data from one sample. The figure shows the how the differential transmission evolves with the minimal coupling distance. We fit the differential transmission with a simulation based on the coupled equation in the waveguide coupling theory. It was assumed that the coupling coefficient was exponentially depend on the coupling distance.

5.3.3 Coupling theory and backward simulation

Considering the coupled mode theory of waveguides, the overall mode for light propagating in the z-direction is,

$$\Psi(x,y,z) = A_1(z)\psi_1(x,y)e^{-i\beta_1 z} + A_2(z)\psi_2(x,y)e^{-i\beta_2 z}. \tag{5.2}$$

Inserting the mode in the propagation equation of light in a dielectric with refractive index $n(x,y)$, we get a set of coupled differential equations on the amplitudes A_1 and A_2, which translate into a vector equation on $\mathbf{A}(z) = [A_1(z), A_2(z)]$. The equation of the coupled modes to solve is then,

$$\frac{d\mathbf{A}}{dz} = -iM(z)\,\mathbf{A}(z), \tag{5.3}$$

where the 2×2 matrix M is the coupling matrix. For general consideration, we write the coupling matrix,

$$M(z) = \begin{pmatrix} k_{11}(z) & k_{12}(z)e^{2i\delta z} \\ k_{21}(z)e^{-2i\delta z} & k_{22}(z) \end{pmatrix}, \tag{5.4}$$

where k_{ij} are the different coupling coefficients. If we consider identical waveguides, $\delta = 0$ and $k_{12} = k_{21} = k$. Thus we get,

$$M(z) = \begin{pmatrix} 0 & k(z) \\ k(z) & 0 \end{pmatrix} \tag{5.5}$$

where in our case the distance between the waveguides is not constant along z. This will have an effect on the coupling coefficient k, as it is related to the superposition of the individual waveguide modes.

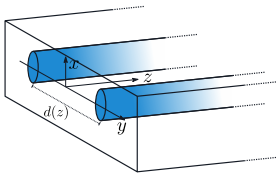

Figure 5.8: Schematic of two identical waveguide separated by a distance $d(z)$, where the propagation direction is along z-axis.

To retrieve the differential transmission, we then have to solve the above equation and compute the power intensity for each mode at z, $P_i(z) \propto |A_i(z)|^2$. We make use of Lagrange formula, which states: if $M(z)$ and $\int_{z_0}^{z} M(s)ds$ commute, then the general solution of the linear differential equation (5.3) is,

$$\mathbf{A}(z) = e^{-i\int_{z_0}^{z} M(s)ds}\mathbf{A}(z_0). \tag{5.6}$$

In our case, the two matrices commute as they are assumed to be symmetric. Otherwise we would have to use the step by step solving method, which is more computational consuming.

To retrieve the coupling coefficient of the directional coupler, we assume that k to be exponentially dependent on the distance between the two waveguides, that is $k = \alpha e^{-\beta d(z)}$ with α, β two positive constants. The geometry of the directional coupler is included in $d(z)$ and parametrized by the minimal distance between the waveguides, d_0, see Fig5.6a.

Then, given a fixed distance d_0, we fit α and β from the measured data. The exponential decay constant β is of more relevance, as it is the driving force for the splitting ratio in the directional couplers. It is moreover the main indicator of the fabrication variability. From the small set of four fabrications, the mean decay constant is $\langle\beta\rangle = 326 \pm 31\text{mm}^{-1}$, see Fig 5.9d.

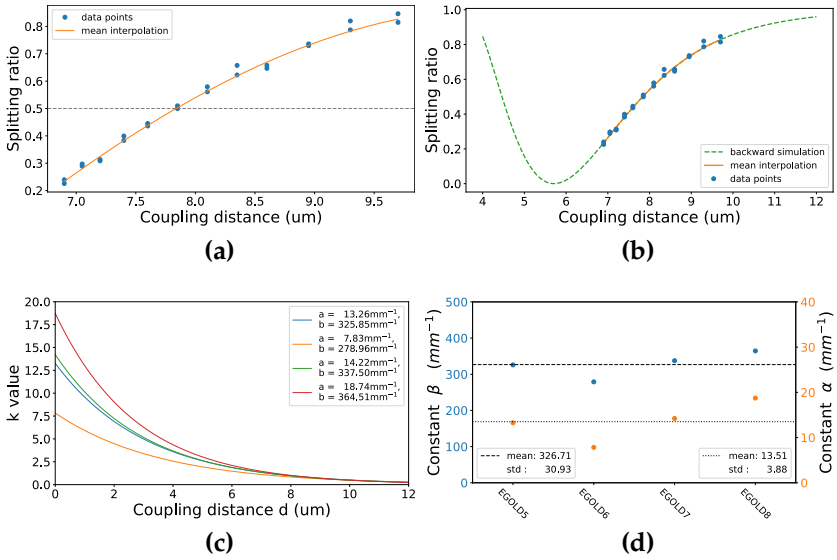

Figure 5.9: (a) Measurement of the splitting ratio of the directional couplers in one sample. The continuous line is a mean interpolation. In (b) the fitted data using the backward simulation. In (c) we display the different coupling coefficients for the different fabrications, and we report the decay constants in figure (d).

5.4 Fabrication of the device

In the end, the final geometry of the design is presented in Fig 5.10.a and Fig 5.10.b. Over all the channels, the minimal radius is chosen to be 60 mm, and the minimal safe distance at each crossing is 20 μm. Considering the distance between channels, if it is too big the circuit will be too long, but if it is too short we might have small coupling between the spatial modes. We thus choose the distance D_{ch} between

the channel to match the fiber array we plan to use. All the geometrical parameters are presented in Table 5.4.

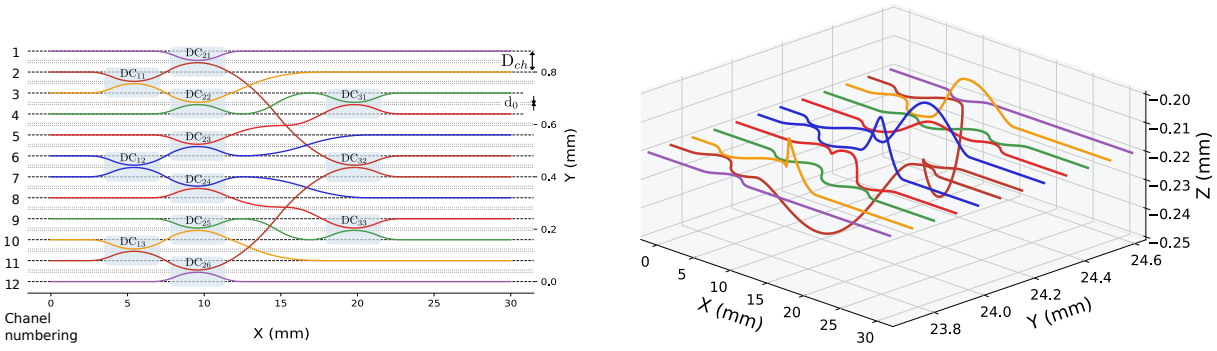

(a) **(b)**

Figure 5.10: Actual implementation of GHZ factory scheme: Top view of the implemented GHZ factory circuit (a) and 3D representation of the actual implemented GHZ factory (b).

After choosing the parameters and the geometry for the implementation of the scheme, we fabricate the photonic circuit. In practice, we still have some variability in the fabrication process, hence we write many copies of the device in parallel, sweeping the minimal coupling distance value of the directional couplers with each copy. Doing so we hope to target the 50:50 splitting ratio in one of the copies. Since the variability is not too strong, it allows us to target a small range of minimal coupling distance with small increment. Each copy has an isolated directional coupler and a straight waveguide in order to check more easily the process performance.

Table 5.4: Parameter for the geometry of the circuits.

Parameter	Symbol	Value (mm)
Distance channel	D_{ch}	0.080
Coupling distance	d_0	0.007
Distance at crossings	$d_{textcross}$	0.020
Minimal radius of curvature	R_{min}	60.000

Chapter 6

Characterisation of the prototype

Contents

Introduction

After several prototyping, we obtain a functioning optical circuit. We now aim to characterise the GHZ factory using coherent beam from laser. Indeed, the circuit aim to operate a unitary transformation on the six initial identical photons. We first estimate the losses introduced in the device. Then we retrieve the splitting ratio of each individual directional couplers before computing the amplitude of the equivalent network matrix coefficients. Finally, since we

deal with quantum operation and optical network, we address the issue of measuring the phase of those coefficients, which are complex-valued.

6.1 Characterisation of the losses

6.1.1 Optical network insertion losses

Contrary to individual waveguides, each inputs of our circuit is connected to several output modes. We then define the insertion losses of each input channel as the ratio between the input power, and the sum of the output power of all channels. The results are presented in Fig 6.1.

Compared to a reference straight waveguide, $\mathrm{IL}_{SWG,ref} = 2.3$ dB, the insertion losses of the device are greater with a mean value of $IL_{Ch} = 3.1 \pm 0.2$ dB, which is expected from the longer path of each individual channel. In addition, there can be some losses due to bending losses.

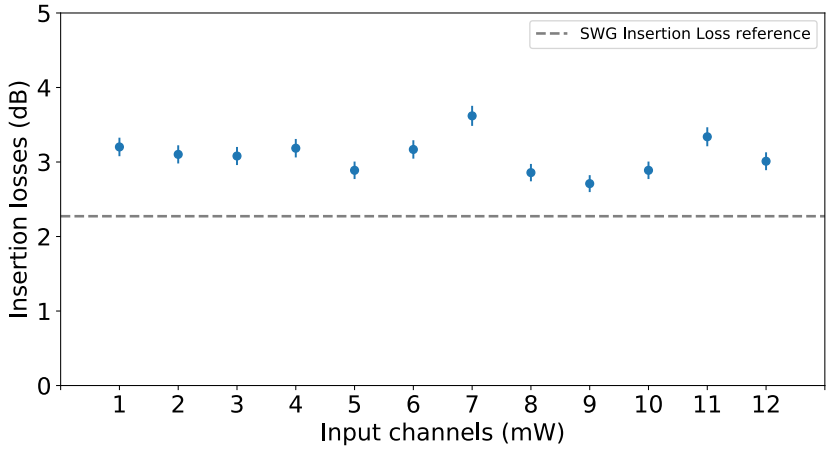

Figure 6.1: Insertion losses of the device for different input channels. The measurement was carried out by coupling the input modes with a fiber waveguide while focusing the output intensity of each output modes with a collection objective on a power meter.

If we want to measure the propagation losses of each individual waveguide, other than cut the sample and isolate portion of the waveguide, there is no practical non-destructive methods because all the channels are coupled one with an other.

6.1.2 Importance of Losses

In the generation of the GHZ state, the consequence of photon losses is that of decreasing the rate of success. Indeed we already mentioned that we can post-select the output state that altogether satisfy the heralding condition and conserve the photon number.

The advantage of the cluster based quantum computing architecture, is that the growth of the cluster is made ahead of computation. Consequently, everything is allowed, every tricks are permitted, as long as they lead to efficient cluster state generation. Moreover, although photon loss disrupts greatly the computation capability, it can be easily detected, contrary to phase errors. On the theoretical side, there have been many suggestions to achieve fault-tolerance in the one-way computer scheme, such as using surface code [89] or exploiting topological quantum computing [90]. However, the robustness against photon losses have an heavy resource cost, as the complexity of the cluster state and the number of constitutive elements per logical qubit, increase with the loss-rate.

In addition we should not forget that our circuit is in principle part of a bigger scheme. Coupled with the source efficiency as well as the detectors one, if we add the statistical success in the theoretical scheme, we should be careful not to reduce the success rate to unpractical low value. Indeed, the generation rate of the building block elements should be high enough to avoid the use of quantum memory. Even as a proof of concept, high losses in the GHZ factory sample jeopardize the detection and manipulation of the GHZ output states for experimental application. In the literature, a reasonable loss-rate of 10^{-3} per component, is commonly advanced for feasible implementation [13, 61, 94]. A component is commonly define as a set of elements that implement an operation, a measurement or the full generation of a quantum state in our case.

In this regard, how our device performs? Not very well. Let us estimate the generation success rate of one GHZ state. Concerning the probabilistic success rate, there are eight heralding detection patterns that lead to a GHZ-class state. The normalisation constant of the total output state being $\mathcal{N} = 16$, we have a success probability of good heralding given by, $p_h = \frac{8}{16^2} = 0.03125$. Now turning to the loss rate. Assuming an overall 3dB of attenuation per

channel, it gives a success probability of keeping six photon along the circuit, $p_c = (10^{-0.3})^6 \simeq 10^{-1.8}$. Accounting for the source efficiency, we can estimate the generation rate of six identical photon as $p_s = (0.6)^6 = 0.04666$ at worst (Table 1 from Ref [97]). We took the *brightness* of the source, defined as the probability of each pulse being single photon. Now accounting for detection efficiency per SSPDs (Superconducting single-photon detector), which can be estimated to be $p_d = 0.75$; as well as the generic losses for the fiber connection and travel between the source, the device and the detector, $p_t = 0.9$. As a result, the success rate of the whole scheme is estimated by: $p_{tot} = p_h p_c p_s p_d^6 p_t^6 \simeq 2.2 \times 10^{-6}$ This value is indeed very low. If we consider the source rate in the order of GHz, it would mean we have a positive result at a rate of $\simeq$ 1kHz. Altough acceptable for proof of concept experiment, the success rate is still far below the wanted value of 10^{-3}/components.

On the other hand, standard values of propagation loss achieved in the group, revolve around 0.1 dB/cm, at 1550 nm. Moreover, there are no indication that the bulk borosilicate subtrate absorbs more in the 900 nm than in the 1550nm. Therefore, we look forward to further investigate and optimise the loss figure of our waveguide.

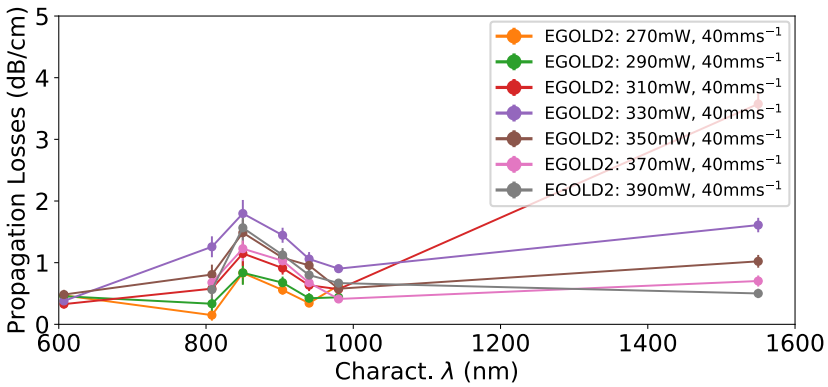

Figure 6.2: Evolution of the propagation losses with respect to the wavelength of the propagating light, for different fabrication average power while keeping the parameter of the optimised waveguides.

We already characterised the same optimised straight waveguides for 904 nm with different wavelengths. The striking result is that there seems to be a peak of losses around the 880 nm wavelength whatever the fabrication average power, see Fig 6.2.

6.2 Lossless Optical Network Matrix characterisation

To further characterise the optical network, we can retrieve information on the functioning of the circuit by normalising the measured output power with the total output power for each input. Consequently, we consider the network as if it was lossless. Theoretically it is equivalent to consider that we post select the output that conserve the photon number.

6.2.1 Theory behind the characterisation

Instead of using resource costing techniques, such as single photon characterisation, we chose to use the method explained in Ref [86]. In this approach, coherent light is also used, but the complex-valued network matrix is determined, which allows to predict the output of any given state following the method in Ref [85], presented below.

The GHZ factory theoretical network matrix

The optical network is then represented by a square matrix, U, with complex coefficient, $u_{i,j} = r_{i,j}e^{i\theta_{i,j}}$, such that $r_{i,j}$ is a positive scalar and $\theta_{i,j} \in [0, 2\pi[$. We constructed the theoretical network matrix, U_{th} in eq 6.1, from the theoretical scheme while accounting for the channel switching.

$$U_{th} = \begin{bmatrix}
\frac{\sqrt{2}}{2} & 0 & 0 & 0 & 0 & \frac{i}{2} & -\frac{1}{2} & 0 & 0 & 0 & 0 & 0 \\
\frac{i}{2} & \frac{i}{2} & -\frac{\sqrt{2}}{4} & -\frac{\sqrt{2}i}{4} & 0 & \frac{\sqrt{2}}{4} & \frac{\sqrt{2}i}{4} & 0 & 0 & 0 & 0 & 0 \\
-\frac{1}{2} & \frac{1}{2} & \frac{\sqrt{2}i}{4} & -\frac{\sqrt{2}}{4} & 0 & \frac{\sqrt{2}i}{4} & -\frac{\sqrt{2}}{4} & 0 & 0 & 0 & 0 & 0 \\
0 & \frac{\sqrt{2}i}{2} & \frac{1}{2} & \frac{i}{2} & 0 & 0 & 0 & 0 & 0 & 0 & 0 & 0 \\
0 & 0 & \frac{i}{2} & \frac{1}{2} & \frac{\sqrt{2}i}{2} & 0 & 0 & 0 & 0 & 0 & 0 & 0 \\
0 & 0 & -\frac{\sqrt{2}}{4} & \frac{\sqrt{2}i}{4} & \frac{1}{2} & 0 & 0 & \frac{i}{2} & -\frac{\sqrt{2}}{4} & -\frac{\sqrt{2}i}{4} & 0 & 0 \\
0 & 0 & -\frac{\sqrt{2}i}{4} & -\frac{\sqrt{2}}{4} & \frac{i}{2} & 0 & 0 & \frac{1}{2} & \frac{\sqrt{2}i}{4} & -\frac{\sqrt{2}}{4} & 0 & 0 \\
0 & 0 & 0 & 0 & 0 & 0 & 0 & \frac{\sqrt{2}i}{2} & \frac{1}{2} & \frac{i}{2} & 0 & 0 \\
0 & 0 & 0 & 0 & 0 & 0 & 0 & 0 & \frac{i}{2} & \frac{1}{2} & \frac{\sqrt{2}i}{2} & 0 \\
0 & 0 & 0 & 0 & 0 & -\frac{\sqrt{2}}{4} & \frac{\sqrt{2}i}{4} & 0 & -\frac{\sqrt{2}}{4} & \frac{\sqrt{2}i}{4} & \frac{1}{2} & -\frac{1}{2} \\
0 & 0 & 0 & 0 & 0 & \frac{\sqrt{2}i}{4} & \frac{\sqrt{2}}{4} & 0 & -\frac{\sqrt{2}i}{4} & -\frac{\sqrt{2}}{4} & \frac{i}{2} & \frac{i}{2} \\
0 & 0 & 0 & 0 & 0 & -\frac{1}{2} & \frac{i}{2} & 0 & 0 & 0 & 0 & \frac{\sqrt{2}}{2}
\end{bmatrix} \tag{6.1}$$

Amplitude coefficient

The amplitude of the optical network matrix coefficients are given by the ratio of the input and output powers,

$$r_{i,j} = \sqrt{\frac{P_{\text{out},j}}{P_{\text{in},i}}}. \tag{6.2}$$

The experimental setup for the amplitude characterisation is identical than for waveguide characterisation.

However, as explained previously, we choose to post-select the state that conserve the energy. We thus substitute the input power by the total output power resulting from input i: $P_{\text{in},i} \rightarrow P^{\text{tot}}_{\text{out},i} = \sum_{k=1}^{N} P_{\text{out},k}$. As a result, the amplitude of the lossless network matrix coefficients are given by,

$$r_{i,j} = \sqrt{\frac{P_{\text{out},j}}{P^{\text{tot}}_{\text{out},i}}} \tag{6.3}$$

Measuring the phase

In order to measure the phase of the complex-valued network matrix coefficients, we adopt an interferometric approach, since phases are always measured with respect to a reference. To do so, we input the device with two coherent beams having a given relative phase $\phi(t)$. In practice, this is done by splitting a laser beam in two while introducing a tunable delay for one of them.

Let i, i_0 be the two input ports. We suppose to have equally split the incoming beam, so we write the input powers,

$$P_i = P_0, \qquad P_{i_0} = P_0 e^{i\phi(t)}. \tag{6.4}$$

The measured powers of two output ports j, j_0 are given by,

$$P_j = P_0 |u_{i,j} + u_{i_0,j} e^{i\phi(t)}|^2, \tag{6.5}$$

$$P_{j_0} = P_0 |u_{i,j_0} + u_{i_0,j_0} e^{i\phi(t)}|^2. \tag{6.6}$$

Expending the relations (6.5), (6.6), we obtain the interfer-

ence equations,

$$P_j = P_0 \left[r_{i,j}^2 + r_{i_0,j}^2 + 2 r_{i,j} r_{i_0,j} \cos\left(\phi(t) + \theta_{i,j} - \theta_{i_0,j}\right) \right], \quad (6.7)$$

$$P_{j_0} = P_0 \left[r_{i,j_0}^2 + r_{i_0,j_0}^2 + 2 r_{i,j_0} r_{i_0,j_0} \cos\left(\phi(t) + \theta_{i,j_0} - \theta_{i_0,j_0}\right) \right]. \quad (6.8)$$

This is the very general expression of the output powers of port j, j_0, with respect of the split input power in ports i, i_0. The core idea is then to sweep the input relative phase $\phi(t)$, in order to retrieve the dephasing between the output powers: $\Delta\Theta = (\theta_{i,j} - \theta_{i_0,j}) - (\theta_{i,j_0} - \theta_{i_0,j_0})$, related to the network matrix coefficients. However, to determine $\theta_{i,j}$ alone, we need to already know $\theta_{i_0,j}, \theta_{i,j_0}, \theta_{i_0,j_0}$ in this measurement.

It has been shown that for a $N \times N$ unitary matrix, $2N-1$ phases are not physically relevant [81]. They are actually not accessible by this kind of measurement, in the same manner than global phase terms are not measurable in a quantum state. As a consequence, any unitary matrices U has an equivalent matrix U', that differs by a change of the phases of the basis vector: $U = D(\boldsymbol{\mu}) U' D(\boldsymbol{\nu})$, where $\boldsymbol{\mu}$ is a vector of N phases and $D(\boldsymbol{\mu}) = \mathrm{diag}(e^{i\mu_1}, \ldots, e^{i\mu_N})$. Those two matrices represent for our purposes the same physical operation.

Since it is convenient to choose null reference phases, we refer to the set of 2N-1 zero phases as the *border of zeros*. In Ref [86], they choose an arbitrary input, $i_0 = 1$, and an output port, $j_0 = 1$, as their references. Hence choosing the border of zeros as: $\theta_{1,k} = \theta_{k,1} = 0$ for $k = 1, \ldots, N$. This choice leads to the expression,

$$P_1 = P_0 \left[r_{i,1}^2 + r_{1,1}^2 + 2 r_{i,1} r_{1,1} \cos(\phi(t)) \right], \quad (6.9)$$

$$P_j = P_0 \left[r_{i,j}^2 + r_{1,j}^2 + 2 r_{i,j} r_{1,j} \cos\left(\phi(t) + \theta_{i,j}\right) \right], \quad (6.10)$$

thus giving for any $i \neq 1, j \neq 1$, a measure of $\theta_{i,j}$.

In this protocol, it is important to control the dephasing between the input beams. However using bulk optics, the stability of relative phase between two beam is difficult to achieve without active stabilization techniques. A cunning trick to circumvent the issue of imprecise phase tuning for the input beam is to use the Lissajous representation, *e.g.* explained in Ref [42]. For this purpose, we

introduce the bare oscillation powers, which we will refer as the *reduced powers* $p_k(t)$:

$$p_k(t) = \frac{\tilde{P}_k(t) - \Sigma_k}{\Lambda_k}, \tag{6.11}$$

$$\tilde{P}_k(t) = \frac{P_k(t)}{I_{\text{tot}(t)}}, \tag{6.12}$$

$$\Sigma_k = \frac{1}{2}\left(\max_t(\tilde{P}_k(t)) + \min_t(\tilde{P}_k(t))\right), \tag{6.13}$$

$$\Lambda_k = \frac{1}{2}\left(\max_t(\tilde{P}_k(t)) - \min_t(\tilde{P}_k(t))\right). \tag{6.14}$$

As a result, plot $p_k(t)$ versus $p_{l\neq k}(t)$ assumes the shape of an ellipse, whose tilt and axis ratio represent the value of the relative phase $\theta_{k,l}$. Consequently, We can retrieve the dephasing $\theta_{k,l}$ between the two oscillators, by performing a numerical fitting of the shape of the ellipse, also called Lissajous diagram. Doing so, the precision on the phase measurement is no longer depend on the precision of the detuning between the two input beam, as long as the values of $\phi(t)$ span over a 2π phase interval. The full process is displayed in Fig 6.3.

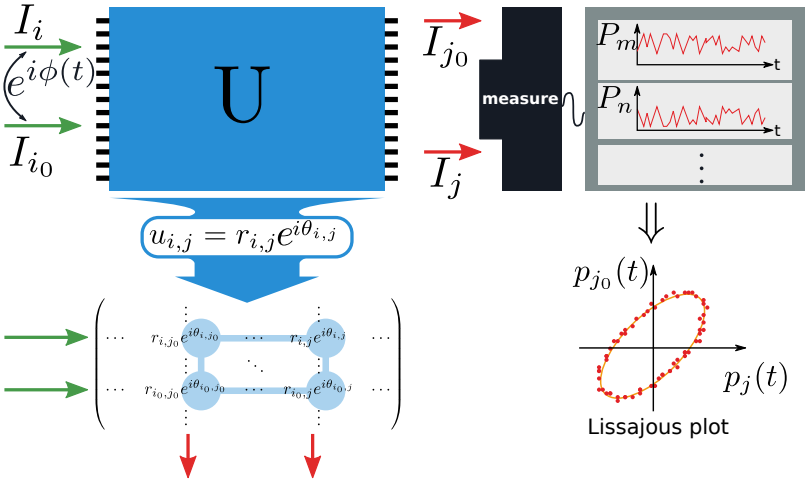

Figure 6.3: Phase measurement: theoretical scheme. We couple the device in inputs i, i_0, with two beams having a phase delay. We measure all the output powers, and choose to consider the outputs j, j_0. It is equivalent to chose a square of coefficient in the matrix representation. We can then plot the reduced intensity, $i_k(t)$, of outputs $k = j, j_0$ to retrieve the dephasing between $p_j(t)$, $p_{j_0}(t)$.

6.2.2 Amplitude characterisation

From the measurement of the output power of one channel and the total output power, we can represent the amplitude matrix as in Fig 6.4a, which can be compared to the theoretical one in Fig 6.4b by taking the modulus of each coefficient in eq (6.1). For better comparison, we flatten the representation so that we display all the coefficient in a 1D chart, as shown in Fig 6.4c. The figures show that we have good agreement between the measured data and the expected non zeros values when we consider the lossless network.

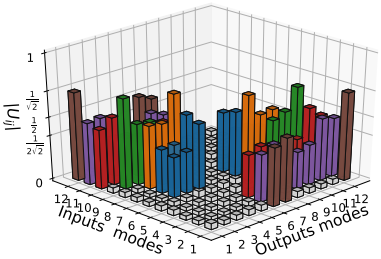

(a) Measured amplitude matrix

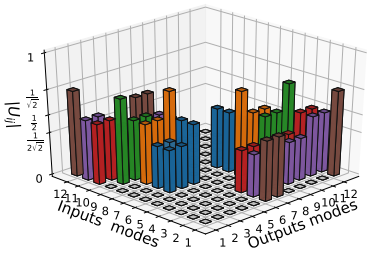

(b) Theoretical amplitude matrix

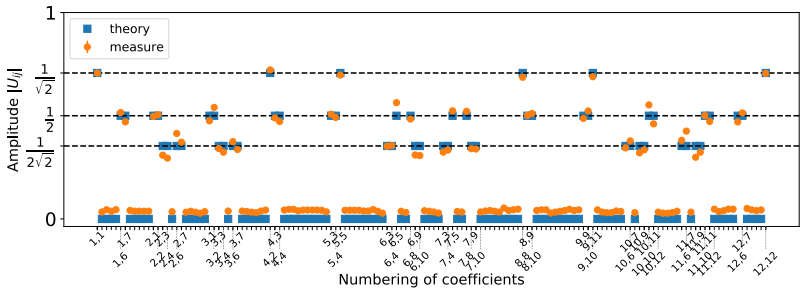

(c) Flatten representation

Figure 6.4: Matrix representation of the amplitude coefficient of the quantum optical network. In (a) the measured amplitude coefficients, in (b) the amplitude of the theoretical matrix, U_{th}. In (c) the 1D representation of the amplitude coefficients of the matrix network. Instead of zero, we have a background intensity. The camera being very sensitive and the collection objective having a high numerical aperture.

Since the amplitude matrix is a real-valued matrice, we aim to compare our result to the theory by considering the similarity, $\mathcal{S}$, of two classical matrices. We define the simi-

larity as,

$$\mathcal{S} = \frac{\left[\mathrm{Tr}(\bar{\mathrm{U}}_{\mathrm{exp}} \cdot \bar{\mathrm{U}}^{t}_{\mathrm{th}})\right]^{2}}{\mathrm{Tr}(\bar{\mathrm{U}}_{\mathrm{exp}} \cdot \bar{\mathrm{U}}^{t}_{\mathrm{exp}})\,\mathrm{Tr}(\bar{\mathrm{U}}_{\mathrm{th}} \cdot \bar{\mathrm{U}}^{t}_{\mathrm{th}})}, \tag{6.15}$$

where M^t is the transpose of the matrix M and $\bar{\mathrm{U}}_{\mathrm{exp}}, \bar{\mathrm{U}}_{\mathrm{th}}$ are the experimental and theoretical amplitude matrices respectively. We calculated that our device have a similarity of $\mathcal{S} = 0.997 \pm 0.032$, to the theoretical circuit.

From the amplitude measurement, we can retrieve the splitting ratio of each individual directional coupler. For instance, looking at Fig 5.10.a, when we couple light in input port 1 it allows us to access the splitting ratio of DC_{32} by measuring the relative output power of port 6 and 7. The transmission and reflection coefficients are displayed in Fig 6.5.

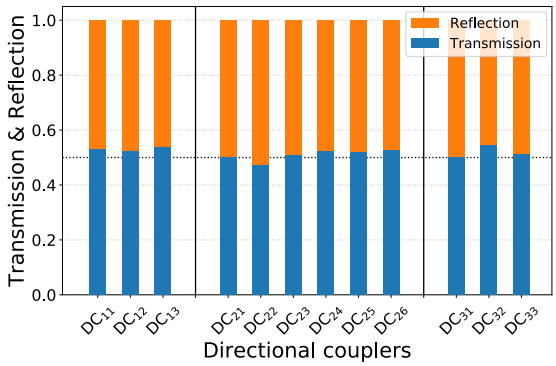

Figure 6.5: Normalised splitting ratios for each individual directional couplers. From the raw transmission and reflection, t, r respectively, we computed the normalised ones, $\bar{t} = t/(r+t)$ and $\bar{r} = r/(t+r)$.

The splitting ratios are close the 50:50, with an average value of, $\langle t \rangle = 0.499$ and $\langle r \rangle = 0.501$, with both a standard deviation of $\sigma = 0.019$. Over all, the directional couplers show consistent and similar ratio. It confirms the similarity of the measured amplitude coefficients in a lossless configuration with respect to the theory. This result emphasize the robustness of the fabrication technology.

6.2.3 Toward phase characterisation

In the following we will introduce the work that has been done to implement the scheme described in Ref [86].

Experimental setup for phase characterisation

In order to implement the measurement, we use a Michelson setup to separate the laser beam and have control over the phase delay in each input. On top of that, we can characterise the fringe visibility of free space propagation interference of the input apparatus, see Fig 6.6. To be able to couple different inputs, we choose to employ the end-fire coupling configuration.

The measurement setup scheme and the actual setup are presented in Fig 6.7. For the measurement of the phase we need to record the evolution of the output powers in time. We thus interfaced the camera with a python-written GUI to visualise the Lissajous plot in real time, see Fig 6.9.

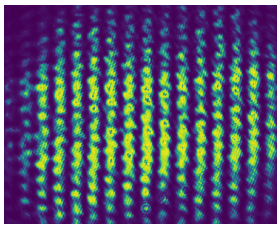

Figure 6.6: Picture of the fringe pattern in the tilted mirror configuration of the Michelson interferometer. The general visibility of the fringe is calculated by taking the mean visibility of several horizontal slices. The value constant with the translation of one mirror at the increment of 0.05mm: visibility is 0.762 ± 0.007.

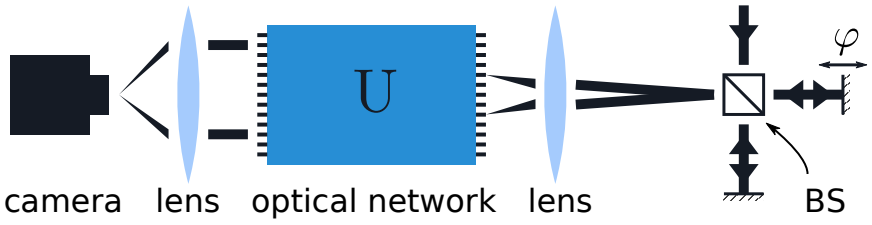

(a) Scheme of the setup

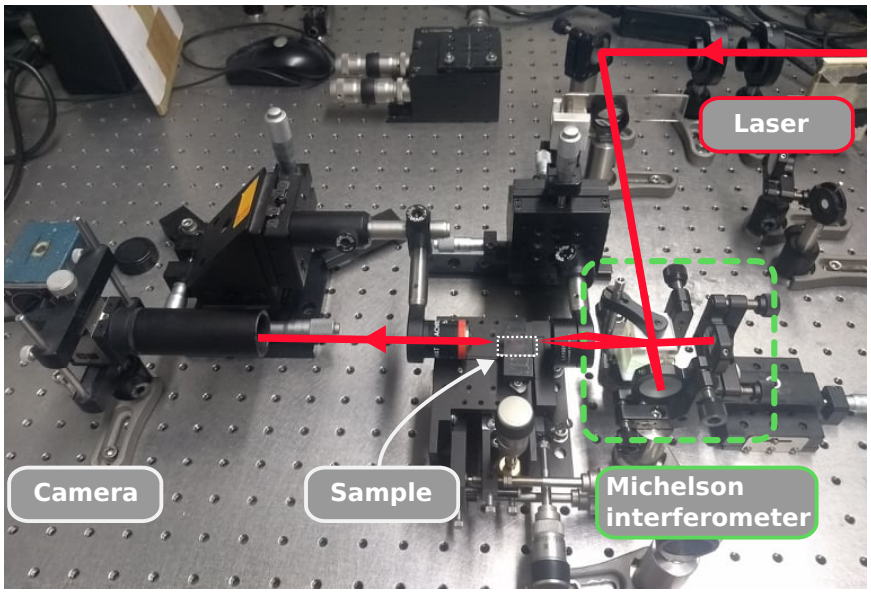

(b) Actual setup

Figure 6.7: (a) shows the scheme of the phase measurement setup. The laser source input from the top of the beam-splitter. Each arm is used to couple different input of the optical network, placed at the focal point of a lens. One arm is used to introduce a tunnable dephasing between the two beams. In (b) a picture of the actual setup, with the red line representing the laser beam.

Test of the setup with a beam-splitter

To test our experimental setup, we employ the method on an arbitrary beam splitter. The most general expression of a lossless beam splitter with arbitrary transmissivity is,

$$BS = \begin{pmatrix} t & ie^{+i\theta}r \\ ie^{-i\theta}r & t \end{pmatrix}, \tag{6.16}$$

with r, t real scalar and $t^2 + r^2 = 1$, while $ie^{i\pm\theta}$ ensures that the operator is unitary.

We now introduce random phase shifts in the input and output ports of the beam splitter, as illustrated in Fig 6.8a. The final expression is,

$$BS' = \begin{pmatrix} te^{i(\phi_1+\phi_2)} & re^{i(\phi_1+\phi_3+\frac{\pi}{2}+\theta)} \\ re^{i(\phi_2+\frac{\pi}{2}-\theta)} & te^{i\phi_3} \end{pmatrix}. \tag{6.17}$$

We define the border of zeros such that the coefficients $u_{1,1}, u_{1,2}, u_{2,1}$ have zero phase. We thus solve the equation on the external phases $\mu_1, \mu_2, \nu_1, \nu_2$ such that,

$$D(\boldsymbol{\mu})BS'D(\boldsymbol{\nu}) = \begin{pmatrix} te^0 & re^0 \\ re^0 & te^{i\Phi} \end{pmatrix}, \tag{6.18}$$

with Φ the unknown phase. We find the solutions of the system of coupled linear equation to be,

$$\mu_2 = -\nu_2 - \phi_3 - \pi, \tag{6.19}$$
$$\nu_1 = +\nu_2 - \phi_2 + \phi_3 + \theta + \pi/2, \tag{6.20}$$
$$\mu_1 = -\nu_2 - \phi_1 - \phi_3 - \theta - \pi/2. \tag{6.21}$$

The bordered matrix is then,

$$BS_{\text{bordered}} = \begin{pmatrix} te^0 & re^0 \\ re^0 & te^{i\pi} \end{pmatrix}, \tag{6.22}$$

where all the relative phases $\phi_{k=1,2,3}$ have completely disappeared. In our case it is very interesting because any beam-splitter can thus serves as a standard to calibrate the setup.

When carrying out the measurement, we indeed recover the π-shift as shown in Fig 6.8b. The working of the experimental setup and the interfacing of the camera, open new

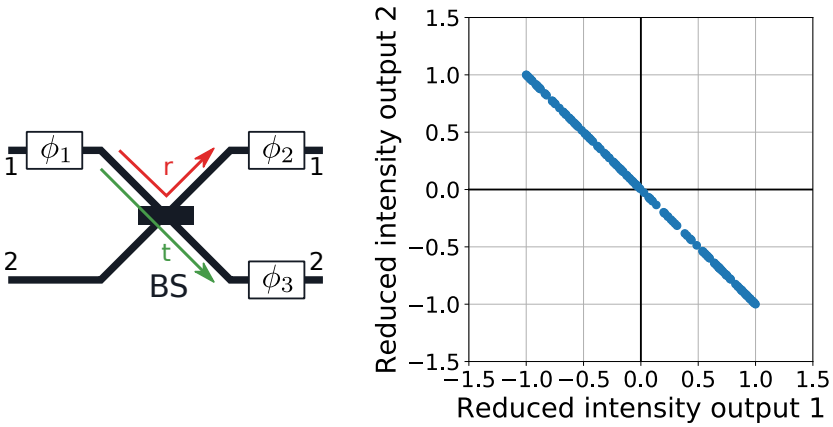

(a) **(b)**

Figure 6.8: (a) Drawing representing the several phases at each port of an arbitrary lossless beam-splitter.(b) Lissajous plot of the two output reduced intensity from a 50:50 directional coupler. We observe the two intensities to oscillate in opposition, thus having a π relative phase.

perspective for phase characterisation after fabrication. Indeed, until now, phase measurements were carried out by collaborators, using two single photons quantum process tomography (QPT). We hope to proceed with the phase characterisation of the photonic circuit, although there are still some theoretical understanding that has to be deepened. The sparsity of the network matrix complicates the study, as further developed in the following sections.

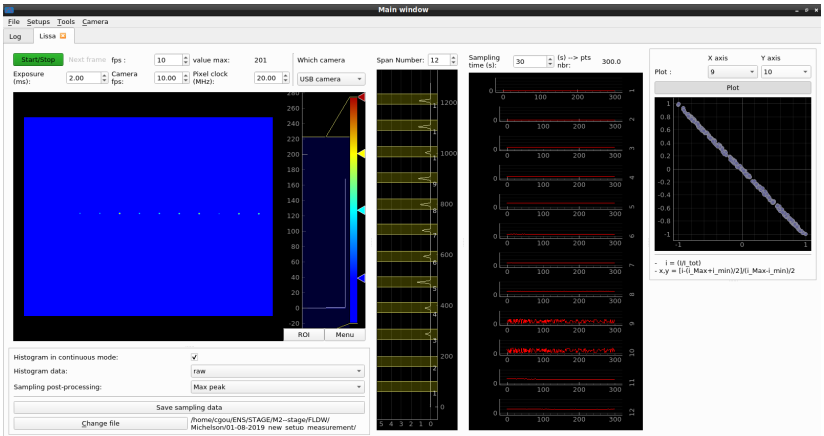

camera image histogram multi-plots Lissajous plot

Figure 6.9: Screen-shot of the camera interface. On the left is the colored image of the camera power measurement. A histogram along the vertical axis of the image is used to plot the power evolution in multi-plot window for in each yellow regions on the histogram window. At last on the far right, we plot a Lissajous figure of the chosen power.

6.3 Multi-photon interference

In this section we will discuss multi-photon interference and how it is related to our device and the measurement setup we use. Indeed as explained previously, there are phases that are not relevant in a given measurement setup, since they can not be measured. The phase characterisation setup with coherent light we use is a classical method to measure second-order correlation between two photons. However, not all optical circuits have 2nd order correlation sensitive to internal spurious phases. The main example being the beam splitter, as demonstrated in sec. 6.2.3. Let us show this property by applying the characterisation protocol on more and more complex circuits.

6.3.1 2-ports circuit

First, we turn back to the example of a Mach-Zehnder interferometer, see Fig 6.10. It can be described as a 2-ports interferometer with the network matrix U,

Figure 6.10: Schematic of a two port interferometric device. It is a well known Mach-Zehnder interferometer.

$$U = \frac{1}{2}\begin{bmatrix} 1-e^{i\Delta\phi} & -ie^{i\Delta\phi}-i \\ -ie^{i\Delta\phi}-i & -1+e^{i\Delta\phi} \end{bmatrix}. \tag{6.23}$$

To measure the 2nd-order correlation of two photon interference, one should look at the coincidence detection of the photon at the two output port. The probability of measuring an output photon in port 1 and port 2 while inputting one photon in port 1 and in port 2, $P_{1,2}^{1,2}$, is given by the modulus square of the permanent of U,

$$\begin{aligned} P_{1,2}^{1,2} &= |\mathrm{perm}(U)|^2 && (6.24)\\ &= \left|\frac{1}{4}\left[-\left(e^{i\Delta\phi}-1\right)^2+\left(ie^{i\Delta\phi}+i\right)^2\right]\right|^2 && (6.25)\\ &= \left|\frac{1}{2}\left[e^{i2\Delta\phi}+1\right]\right|^2 && (6.26)\\ &= \cos(\Delta\phi)^2. && (6.27) \end{aligned}$$

The measure of $P_{1,2}^{1,2}$ is directly related to $\Delta\phi$.

6.3.2 4-ports circuit

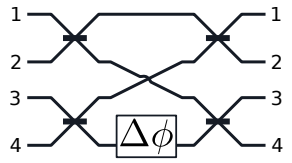

Figure 6.11: Schematic of a four port interferometric device.

Similarly, if we consider a more complicated network, as in Fig 6.11, we look for a measurement that allows to characterise a spurious phase.

The network matrix in this case is given by,

$$U = \frac{1}{2}\begin{bmatrix} e^{-\frac{i\Delta\phi}{2}} & -ie^{-\frac{i\Delta\phi}{2}} & -ie^{-\frac{i\Delta\phi}{2}} & -e^{-\frac{i\Delta\phi}{2}} \\ -ie^{-\frac{i\Delta\phi}{2}} & -e^{-\frac{i\Delta\phi}{2}} & e^{-\frac{i\Delta\phi}{2}} & -ie^{-\frac{i\Delta\phi}{2}} \\ -ie^{-\frac{i\Delta\phi}{2}} & e^{-\frac{i\Delta\phi}{2}} & -e^{\frac{i\Delta\phi}{2}} & -ie^{\frac{i\Delta\phi}{2}} \\ -e^{-\frac{i\Delta\phi}{2}} & -ie^{-\frac{i\Delta\phi}{2}} & -ie^{\frac{i\Delta\phi}{2}} & e^{\frac{i\Delta\phi}{2}} \end{bmatrix} \tag{6.28}$$

Like above, we measure the coincidence detection of output port 1 and 3 when inputting one photon in port 1 and 3: $P_{1,3}^{1,3}$. Now, this quantity is given by the permanent of the sub-matrix,

$$U_{1,3}^{1,3} = \begin{bmatrix} u_{11} & u_{13} \\ u_{31} & u_{33} \end{bmatrix} = \frac{1}{2}\begin{bmatrix} e^{-\frac{i\Delta\phi}{2}} & -ie^{-\frac{i\Delta\phi}{2}} \\ -ie^{-\frac{i\Delta\phi}{2}} & -e^{\frac{i\Delta\phi}{2}} \end{bmatrix}, \tag{6.29}$$

obtain by the intersection between line $1,3$ and columns $1,3$ of matrix U. We thus have,

$$P_{1,3}^{1,3} = |\text{perm}(U_{1,3}^{1,3})|^2 \tag{6.30}$$

$$= \frac{1}{4}\cos\left(\frac{\Delta\phi}{2}\right)^2. \tag{6.31}$$

Again, the coincidence detection depends from the phase $\Delta\phi$. Now if we consider the coherent light measurement protocol, the sub-matrix matrix can be equivalently written,

$$U_{1,3}^{1,3} = \begin{bmatrix} e^{-\frac{i\Delta\phi}{2}} & 0 \\ 0 & e^{-\frac{i\Delta\phi}{2}-\frac{\pi}{2}} \end{bmatrix}\frac{1}{2}\begin{bmatrix} 1 & 1 \\ 1 & e^{i\theta} \end{bmatrix}\begin{bmatrix} 1 & 0 \\ 0 & e^{0} \end{bmatrix} \tag{6.32}$$

where we set the border of zeros for u_{11}, u_{13}, u_{31}. As a result $\theta \equiv \Delta\phi[2\pi]$. Contrary to the beam splitter case, the phase $\Delta\phi$ survives and can thus be measured by the two coherent beam interference.

6.3.3 6-ports circuit

We now move to a different case, where we consider a 6-ports optical interferometer, see Fig 6.12. The network ma-

trix of the circuit is given by,

$$U = \frac{1}{2}\begin{bmatrix} 1 & i & 0 & 0 & -e^{i\gamma} & ie^{i\gamma} \\ ie^{i\alpha} & e^{i\alpha} & i & -1 & 0 & 0 \\ -e^{i\alpha} & ie^{i\alpha} & 1 & 1i & 0 & 0 \\ 0 & 0 & ie^{i\beta} & e^{i\beta} & i & -1 \\ 0 & 0 & -e^{i\beta} & ie^{i\beta} & 1 & i \\ i & -1 & 0 & 0 & ie^{i\gamma} & e^{i\gamma} \end{bmatrix}. \tag{6.33}$$

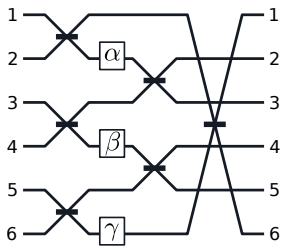

Figure 6.12: Schematic of a six ports interferometric device.

However, with this circuit, their are no correlation measurements that are sensitive to any of the three internal phases α, β or γ.

Indeed, whatever the submatrix $U^{k,l}_{i,j}$, it can be shown that it is always equivalent to a matrix with no dependence on the spurious phases,

$$U^{k,l}_{i,j} = D(\boldsymbol{\mu})\begin{bmatrix} |u_{ik}| & |u_{il}| \\ |u_{jk}| & \pm|u_{jl}| \end{bmatrix} D(\boldsymbol{\nu}), \tag{6.34}$$

following the notation in sec. 6.2.2. In other words, the circuit operation in a two photons experiment does not present any dependency on internal phases. The remarkable feature is when we consider three photons. Indeed, if we want to measure the correlation when three photons are involved, we can choose to input the device in channels {1,3,5} and measure the coincidence detection in output channels {1,3,5}. The probability is given by the squared amplitude of the submatrix $U^{1,3,5}_{1,3,5}$ permanent. We find that,

$$P^{1,3,5}_{1,3,5} = |\frac{1}{8}\left(1 - e^{i(\alpha+\beta+\gamma)}\right)|^2 \tag{6.35}$$

$$= \frac{1}{16}\sin^2(\frac{\alpha+\beta+\gamma}{2}). \tag{6.36}$$

Here the probability depends on the sum of the internal phases. We thus show a configuration of optical circuit that does not display two-photon correlation, but of superior order.

6.3.4 GHZ factory circuit

We conclude stating that the GHZ factory falls into the same case of the 6-ports network, displayed above. The

measurement protocol of Ref [86] does not address this issue. One can find in the literature several studies on more than two photon interference [1, 56]. We then aim to improve the actual experimental setup to perform measurement that can be sensitive to such 3rd-order correlation.

Conclusion & perspectives

In this thesis, we presented the work performed toward the fabrication and characterisation of a photonic integrated circuit that aims to produce three-photon GHZ states. We made use of the femtosecond laser micromachining technology that allows us to write waveguides in a 3D topology.

We successfully demonstrated the functioning of the theoretical scheme by adapting the already existing protocol devised for the polarization encoding. Not only it allowed us to have an acute understanding of the device, but it also allowed us to present an extended version in order to produce an arbitrary N-qubit GHZ states. In the meantime, we developed the steps needed to fabricate the circuit and adapted the geometry of the device to account for the practical constraints. Finally we characterised the device in terms of losses and energy repartition, while developing a setup to characterise the internal phases.

However, we encountered an optimisation issue has the propagation losses increase in the region around the working wavelength. This issue will lead to further investigation in order to determine what could be the cause. Characterisation of bulk borosilicate properties [21] does not explain alone the observed behaviour. Nonetheless, this loss problem can be related to the absorption properties of the modified glass, as it endures structural changes during femtosecond laser writing. In addition, even if annealing the sample helps to reduce the apparition of color center after laser treatment, a through observation of the waveguide might help to determine if this hypothesis is valid. Furthermore we do not discard the possibility of the generation of micro-structure during fabrication that could resonate

at the working wavelength, as nano-grating in fused silica even if it was never observed in borosilicate. Concerning the characterisation of the internal phases in the circuit, we aim to improve the current setup. More than two coherent beam interference could help resolve the three photon interference we observe in such device.

Finally, in a further development, we look forward to integrate within the same photonic chip an opportune set of tunable Mach-Zehnder interferometers cascaded to the GHZ factory device, in order to perform quantum state tomography. Doing so, we can directly characterise if the quantum state at the output of the device, conditioned by the heralding, belongs indeed in the GHZ class. We will still have to integrate in the final version of our device a mean to render the photonic chip compatible with detection devices and the six identical photon source in development by our collaborators in Paris.

Acknowledgement

As science is more of a social enterprise than the application of a rigorous method, I would like to acknowledge all the persons who demonstrated that a fulfilling and enjoyable workplace goes along with accuracy, rigorousness and sincerity.

This is why, I would like to profoundly acknowledge Roberto Osellame for his bliss and support, and without whom none of this would have happened. I am grateful you entrusted me with this project even in this shorter period than usual. You provided me with an exquisite subject I had the pleasure to explore.

I deeply thank my co-supervisors, Andrea Crespi and Giacomo Corrielli, who were very supportive towards me. You taught me a lot concerning how to approach new problems and overcome others. I shall remember those important lessons. Among them, I learn a great deal regarding the importance of cleaning samples before fabricating as well as how to enjoy long characterisation and laborious fiber coupling. It goes without saying that rooftop pizzas really was a good idea.

Special thanks for Simone Piacentini who helped me more than once in moments of total despair. Not accounting for the beautiful figures you let me used in this report, as far as you know ... In the same spirit, I am acutely grateful to Andrea Adami, Micheale Spagnolo, Riccardo Motta, Francesco Pellegatta and Francesco Ceccarelli who largely participate in making the everyday life as funny as a conversation can get. Particularly, I wish good luck to Federico Sala with the MatLab Gcode-simulator, although I have to admit, a necessary feature for every micromachining group. Let's not forget to thank Petra Paie for introducing me to "les incompétents" which reveal to be a great scapegoat gate

away to excuse my mistakes. To Zhen-Nan Tien I hope you won't get despaired too quickly with your use of Linux-Ubuntu. We all have to start somewhere.

At last but not least, I truly thank the whole team for their support and sympathy. It was a really great pleasure to come working. It has to said, the tea party also really add to it.

Finally, still in the spirit of this open-hearted section, I would like to adress my gratitude to the community of the open-source python programming language. I believe we tend to forget what open-access information can bring to the scientific community. Equivalently, I acknowledge the work of the technicians who help to create and sustain a comfortable work space.

Bibliography

[1] Sascha Agne, Thomas Kauten, Jeongwan Jin, Evan Meyer-Scott, Jeff Z Salvail, Deny R Hamel, Kevin J Resch, Gregor Weihs, and Thomas Jennewein. Observation of genuine three-photon interference. *Physical review letters*, 118(15):153602, 2017. 105

[2] Thomas Allsop, Mykhaylo Dubov, Vladimir Mezentsev, and Ian Bennion. Inscription and characterization of waveguides written into borosilicate glass by a high-repetition-rate femtosecond laser at 800 nm. *Applied optics*, 49(10):1938–1950, 2010. 35

[3] Alexander Arriola, Simon Gross, Nemanja Jovanovic, Ned Charles, Peter G Tuthill, Santiago M Olaizola, Alexander Fuerbach, and Michael J Withford. Low bend loss waveguides enable compact, efficient 3d photonic chips. *Optics express*, 21(3):2978–2986, 2013. 36, 37

[4] Frank Arute, Kunal Arya, Ryan Babbush, Dave Bacon, Joseph C Bardin, Rami Barends, Rupak Biswas, Sergio Boixo, Fernando GSL Brandao, David A Buell, et al. Quantum supremacy using a programmable superconducting processor. *Nature*, 574(7779):505–510, 2019. 2

[5] Adriano Barenco, Charles H. Bennett, Richard Cleve, David P. DiVincenzo, Norman Margolus, Peter Shor, Tycho Sleator, John A. Smolin, and Harald Weinfurter. Elementary gates for quantum computation. *Phys. Rev. A*, 52:3457–3467, Nov 1995. doi: 10.1103/PhysRevA.52.3457. URL https://link.aps.org/doi/10.1103/PhysRevA.52.3457. 2, 6

[6] Sean D Barrett and Pieter Kok. Efficient high-fidelity

quantum computation using matter qubits and linear optics. *Physical Review A*, 71(6):060310, 2005. 10

[7] Charles H Bennett and Gilles Brassard. Quantum cryptography: public key distribution and coin tossing. *Theor. Comput. Sci.*, 560(12):7–11, 2014. 2

[8] Charles H Bennett, Sandu Popescu, Daniel Rohrlich, John A Smolin, and Ashish V Thapliyal. Exact and asymptotic measures of multipartite pure-state entanglement. *Physical Review A*, 63(1):012307, 2000. 22

[9] N Bergamasco, M Menotti, JE Sipe, and M Liscidini. Generation of path-encoded greenberger-horne-zeilinger states. *Physical Review Applied*, 8(5):054014, 2017. 24

[10] Massoud Borhani and Daniel Loss. Cluster states from heisenberg interactions. *Physical Review A*, 71 (3):034308, 2005. 13

[11] H-J Briegel, Wolfgang Dür, Juan I Cirac, and Peter Zoller. Quantum repeaters: the role of imperfect local operations in quantum communication. *Physical Review Letters*, 81(26):5932, 1998. 22

[12] Hans J. Briegel and Robert Raussendorf. Persistent entanglement in arrays of interacting particles. *Phys. Rev. Lett.*, 86:910–913, Jan 2001. doi: 10.1103/PhysRevLett.86.910. URL https://link.aps.org/doi/10.1103/PhysRevLett.86.910. 8

[13] Hans J Briegel, David E Browne, Wolfgang Dür, Robert Raussendorf, and Maarten Van den Nest. Measurement-based quantum computation. *Nature Physics*, 5(1):19, 2009. 12, 13, 91

[14] Daniel E Browne and Terry Rudolph. Resource-efficient linear optical quantum computation. *Physical Review Letters*, 95(1):010501, 2005. 11

[15] Colin D Bruzewicz, John Chiaverini, Robert McConnell, and Jeremy M Sage. Trapped-ion quantum computing: Progress and challenges. *Applied Physics Reviews*, 6(2):021314, 2019. 2

[16] Iulia Buluta and Franco Nori. Quantum simulators. *Science*, 326(5949):108–111, 2009. 1

[17] Francesco Ceccarelli, Simone Atzeni, Alessandro Prencipe, Raffaele Farinaro, and Roberto Osellame. Thermal phase shifters for femtosecond laser written photonic integrated circuits. *Journal of Lightwave Technology*, 2019. 39

[18] G Cerullo, Roberto Osellame, Stefano Taccheo, M Marangoni, Dario Polli, Roberta Ramponi, Paolo Laporta, and Sandro De Silvestri. Femtosecond micromachining of symmetric waveguides at 1.5 μm by astigmatic beam focusing. *Optics letters*, 27(21):1938–1940, 2002. 33

[19] Giacomo Corrielli, Andrea Crespi, Riccardo Geremia, Roberta Ramponi, Linda Sansoni, Andrea Santinelli, Paolo Mataloni, Fabio Sciarrino, and Roberto Osellame. Rotated waveplates in integrated waveguide optics. *Nature communications*, 5:4249, 2014. 38

[20] Andrea Crespi, Roberta Ramponi, Roberto Osellame, Linda Sansoni, Irene Bongioanni, Fabio Sciarrino, Giuseppe Vallone, and Paolo Mataloni. Integrated photonic quantum gates for polarization qubits. *Nature communications*, 2:566, 2011. 40, 44

[21] Cody V Cushman, Brian I Johnson, Andrew Martin, Barry M Lunt, Nicholas J Smith, and Matthew R Linford. Eagle xg® glass: Optical constants from 196 to 1688 nm (0.735–6.33 ev) by spectroscopic ellipsometry. *Surface Science Spectra*, 24(2):026001, 2017. 107

[22] K Miura Davis, Kiyotaka Miura, Naoki Sugimoto, and Kazuyuki Hirao. Writing waveguides in glass with a femtosecond laser. *Optics letters*, 21(21):1729–1731, 1996. 25

[23] Wolfgang Dr, Guifre Vidal, and J Ignacio Cirac. Three qubits can be entangled in two inequivalent ways. *Physical Review A*, 62(6):062314, 2000. 56

[24] W Dür, H-J Briegel, JI Cirac, and P Zoller. Quantum repeaters based on entanglement purification. *Physical Review A*, 59(1):169, 1999. 22

[25] Shane M Eaton, Haibin Zhang, Peter R Herman, Fumiyo Yoshino, Lawrence Shah, James Bovatsek, and Alan Y Arai. Heat accumulation effects in femtosecond laser-written waveguides with variable repetition rate. *Optics Express*, 13(12):4708–4716, 2005. 31

[26] Shane M Eaton, Haibin Zhang, Mi Li Ng, Jianzhao Li, Wei-Jen Chen, Stephen Ho, and Peter R Herman. Transition from thermal diffusion to heat accumulation in high repetition rate femtosecond laser writing of buried optical waveguides. *Optics express*, 16(13): 9443–9458, 2008. 30

[27] Shane M Eaton, Wei-Jen Chen, Haibin Zhang, Rajiv Iyer, Jianzhao Li, Mi Li Ng, Stephen Ho, J Stewart Aitchison, and Peter R Herman. Spectral loss characterization of femtosecond laser written waveguides in glass with application to demultiplexing of 1300 and 1550 nm wavelengths. *Journal of Lightwave Technology*, 27(9):1079–1085, 2009. 40

[28] Luca Faustini and Giuseppe Martini. Bend loss in single-mode fibers. *Journal of lightwave technology*, 15 (4):671–679, 1997. 80

[29] Fulvio Flamini, Lorenzo Magrini, Adil S Rab, Nicolò Spagnolo, Vincenzo D'ambrosio, Paolo Mataloni, Fabio Sciarrino, Tommaso Zandrini, Andrea Crespi, Roberta Ramponi, et al. Thermally reconfigurable quantum photonic circuits at telecom wavelength by femtosecond laser micromachining. *Light: Science & Applications*, 4(11):e354, 2015. 42

[30] Austin G Fowler, Ashley M Stephens, and Peter Groszkowski. High-threshold universal quantum computation on the surface code. *Physical Review A*, 80(5):052312, 2009. 9

[31] Nicolas Gisin and Helle Bechmann-Pasquinucci. Bell inequality, bell states and maximally entangled states for n qubits. *Physics Letters A*, 246(1-2):1–6, 1998. 22

[32] Nicolas Gisin and Rob Thew. Quantum communication. *Nature photonics*, 1(3):165, 2007. 3

[33] Nicolas Gisin, Grégoire Ribordy, Wolfgang Tittel, and Hugo Zbinden. Quantum cryptography. *Reviews of modern physics*, 74(1):145, 2002. 22

[34] EN Glezer, M Milosavljevic, L Huang, RJ Finlay, T-H Her, J Paul Callan, and Eric Mazur. Three-dimensional optical storage inside transparent materials. *Optics letters*, 21(24):2023–2025, 1996. 30

[35] D Gloge. Bending loss in multimode fibers with graded and ungraded core index. *Applied optics*, 11 (11):2506–2513, 1972. 53

[36] Daniel Gottesman and Isaac L Chuang. Demonstrating the viability of universal quantum computation using teleportation and single-qubit operations. *Nature*, 402(6760):390, 1999. 14

[37] Daniel M Greenberger, Michael A Horne, and Anton Zeilinger. Bell's theorem, quantum theory, and conceptions of the universe, 1989. 22

[38] Daniel M Greenberger, Michael A Horne, and Anton Zeilinger. Going beyond bell's theorem. In *Bell's theorem, quantum theory and conceptions of the universe*, pages 69–72. Springer, 1989. 22

[39] Lov K Grover. Quantum mechanics helps in searching for a needle in a haystack. *Physical review letters*, 79(2):325, 1997. 2

[40] Deny R Hamel, Lynden K Shalm, Hannes Hübel, Aaron J Miller, Francesco Marsili, Varun B Verma, Richard P Mirin, Sae Woo Nam, Kevin J Resch, and Thomas Jennewein. Direct generation of three-photon polarization entanglement. *Nature Photonics*, 8(10): 801, 2014. 23

[41] René Heilmann, Markus Gräfe, Stefan Nolte, and Alexander Szameit. Arbitrary photonic wave plate operations on chip: realizing hadamard, pauli-x, and rotation gates for polarisation qubits. *Scientific reports*, 4:4118, 2014. 38

[42] René Heilmann, Markus Gräfe, Stefan Nolte, and Alexander Szameit. A novel integrated quantum circuit for high-order w-state generation and its highly precise characterization. *Science bulletin*, 60(1):96–100, 2015. 95

[43] M. Hein, J. Eisert, and H. J. Briegel. Multiparty entanglement in graph states. *Phys. Rev. A*, 69:062311, Jun 2004. doi: 10.1103/PhysRevA.69.062311. URL https://link.aps.org/doi/10.1103/PhysRevA.69.062311. 9

[44] C Hnatovsky, RS Taylor, E Simova, VR Bhardwaj, DM Rayner, and PB Corkum. High-resolution study

of photoinduced modification in fused silica produced by a tightly focused femtosecond laser beam in the presence of aberrations. *Journal of applied physics*, 98(1):013517, 2005. 32

[45] C Hnatovsky, RS Taylor, E Simova, PP Rajeev, DM Rayner, VR Bhardwaj, and PB Corkum. Fabrication of microchannels in glass using focused femtosecond laser radiation and selective chemical etching. *Applied Physics A*, 84(1-2):47–61, 2006. 30

[46] Chong-Ki Hong, Zhe-Yu Ou, and Leonard Mandel. Measurement of subpicosecond time intervals between two photons by interference. *Physical review letters*, 59(18):2044, 1987. 20, 21

[47] Yun-Feng Huang, Bi-Heng Liu, Liang Peng, Yu-Hu Li, Li Li, Chuan-Feng Li, and Guang-Can Guo. Experimental generation of an eight-photon greenberger–horne–zeilinger state. *Nature communications*, 2:546, 2011. 23

[48] Hannes Hübel, Deny R Hamel, Alessandro Fedrizzi, Sven Ramelow, Kevin J Resch, and Thomas Jennewein. Direct generation of photon triplets using cascaded photon-pair sources. *Nature*, 466(7306):601, 2010. 23

[49] Hannes Hübel, Deny R Hamel, Kevin J Resch, and Thomas Jennewein. Generation of various tri-partite entangled states using cascaded spontaneous down-conversion. In *AIP Conference Proceedings*, volume 1363, pages 331–334. AIP, 2011. 23

[50] M. A. Nielsen Isaac L. Chuang. Prescription for experimental determination ofthe dynamics of a quantum black box. *Journal of Modern Optics*, 44(11-12): 2455–2467, 1997. 17

[51] S Juodkazis, Shigeki Matsuo, H Misawa, V Mizeikis, A Marcinkevicius, H-B Sun, Y Tokuda, M Takahashi, T Yoko, and J Nishii. Application of femtosecond laser pulses for microfabrication of transparent media. *Applied surface science*, 197:705–709, 2002. 30

[52] FP Kapron, Donald B Keck, and Robert D Maurer. Radiation losses in glass optical waveguides. *Applied Physics Letters*, 17(10):423–425, 1970. 80

[53] LV Keldysh et al. Ionization in the field of a strong electromagnetic wave. *Sov. Phys. JETP*, 20(5):1307–1314, 1965. 27

[54] Nikolai Kiesel, Christian Schmid, Ulrich Weber, Géza Tóth, Otfried Gühne, Rupert Ursin, and Harald Weinfurter. Experimental analysis of a four-qubit photon cluster state. *Physical Review Letters*, 95(21):210502, 2005. 14

[55] Alexander Killi, Andy Steinmann, Jochen Dörring, Uwe Morgner, Max J Lederer, Daniel Kopf, and Carsten Fallnich. High-peak-power pulses from a cavity-dumped yb: Ky (wo 4) 2 oscillator. *Optics letters*, 30(14):1891–1893, 2005. 46

[56] DN Klyshko. The bell and ghz theorems: a possible three-photon interference experiment and the question of nonlocality. *Physics Letters A*, 172(6):399–403, 1993. 105

[57] Emanuel Knill, Raymond Laflamme, and Gerald J Milburn. A scheme for efficient quantum computation with linear optics. *nature*, 409(6816):46, 2001. 14

[58] Pieter Kok, William J Munro, Kae Nemoto, Timothy C Ralph, Jonathan P Dowling, and Gerard J Milburn. Linear optical quantum computing with photonic qubits. *Reviews of Modern Physics*, 79(1):135, 2007. 2, 5, 16

[59] Philip Krantz, Morten Kjaergaard, Fei Yan, Terry P Orlando, Simon Gustavsson, and William D Oliver. A quantum engineer's guide to superconducting qubits. *Applied Physics Reviews*, 6(2):021318, 2019. 2

[60] David Kribs, Raymond Laflamme, and David Poulin. Unified and generalized approach to quantum error correction. *Physical review letters*, 94(18):180501, 2005. 2

[61] Ying Li, Peter C Humphreys, Gabriel J Mendoza, and Simon C Benjamin. Resource costs for fault-tolerant linear optical quantum computing. *Physical Review X*, 5(4):041007, 2015. 10, 11, 24, 91

[62] Feng Liang, Réal Vallée, and See Leang Chin. Mechanism of nanograting formation on the surface of fused silica. *Optics express*, 20(4):4389–4396, 2012. 30

[63] D Liu, Y Li, R An, Y Dou, H Yang, and Q Gong. Influence of focusing depth on the microfabrication of waveguides inside silica glass by femtosecond laser direct writing. *Applied Physics A*, 84(3):257–260, 2006. 26

[64] Chao-Yang Lu, Xiao-Qi Zhou, Otfried Gühne, Wei-Bo Gao, Jin Zhang, Zhen-Sheng Yuan, Alexander Goebel, Tao Yang, and Jian-Wei Pan. Experimental entanglement of six photons in graph states. *Nature physics*, 3(2):91, 2007. 14

[65] Andrius Marcinkevičius, Saulius Juodkazis, Mitsuru Watanabe, Masafumi Miwa, Shigeki Matsuo, Hiroaki Misawa, and Junji Nishii. Femtosecond laser-assisted three-dimensional microfabrication in silica. *Optics Letters*, 26(5):277–279, 2001. 26

[66] Dietrich Marcuse. Curvature loss formula for optical fibers. *JOSA*, 66(3):216–220, 1976. 80

[67] Dietrich Marcuse. Field deformation and loss caused by curvature of optical fibers. *JOSA*, 66(4):311–320, 1976. 80

[68] Graham D Marshall, Alberto Politi, Jonathan CF Matthews, Peter Dekker, Martin Ams, Michael J Withford, and Jeremy L O'Brien. Laser written waveguide photonic quantum circuits. *Optics express*, 17(15):12546–12554, 2009. 40

[69] Thomas Meany, Markus Gräfe, René Heilmann, Armando Perez-Leija, Simon Gross, Michael J Steel, Michael J Withford, and Alexander Szameit. Laser written circuits for quantum photonics. *Laser & Photonics Reviews*, 9(4):363–384, 2015. 25

[70] Thomas Meany, Devon N Biggerstaff, Matthew A Broome, Alessandro Fedrizzi, Michael Delanty, MJ Steel, Alexei Gilchrist, Graham D Marshall, Andrew G White, and Michael J Withford. Engineering integrated photonics for heralded quantum gates. *Scientific reports*, 6:25126, 2016. 44

[71] Gerard J Milburn. Quantum optical fredkin gate. *Physical Review Letters*, 62(18):2124, 1989. 6

[72] Ashley Montanaro. Quantum algorithms: an overview. *npj Quantum Information*, 2:15023, 2016. 2

[73] FJ Mustieles, E Ballesteros, and P Baquero. Theoretical s-bend profile for optimization of optical waveguide radiation losses. *IEEE Photonics Technology Letters*, 5(5):551–553, 1993. 81

[74] Michael A Nielsen. Cluster-state quantum computation. *Reports on Mathematical Physics*, 57(1):147–161, 2006. 10

[75] Michael A Nielsen and Isaac Chuang. Quantum computation and quantum information, 2002. 3

[76] Michael A Nielsen and Christopher M Dawson. Fault-tolerant quantum computation with cluster states. *Physical Review A*, 71(4):042323, 2005. 10

[77] Roberto Osellame, Nicola Chiodo, Giuseppe Della Valle, Stefano Taccheo, Roberta Ramponi, Giulio Cerullo, Alexander Killi, Uwe Morgner, Max Lederer, and Daniel Kopf. Optical waveguide writing with a diode-pumped femtosecond oscillator. *Optics letters*, 29(16):1900–1902, 2004. 31

[78] Roberto Osellame, V Maselli, Nicola Chiodo, Dario Polli, R Martinez Vazquez, Roberta Ramponi, and G Cerullo. Fabrication of 3d photonic devices at 1.55/spl mu/m wavelength by femtosecond ti: Sapphire oscillator. *Electronics Letters*, 41(6):315–317, 2005. 41

[79] Roberto Osellame, Giulio Cerullo, and Roberta Ramponi. *Femtosecond laser micromachining: photonic and microfluidic devices in transparent materials*, volume 123. Springer Science & Business Media, 2012. 29, 30, 35

[80] Jian-Wei Pan, Dik Bouwmeester, Harald Weinfurter, and Anton Zeilinger. Experimental entanglement swapping: entangling photons that never interacted. *Physical Review Letters*, 80(18):3891, 1998. 22

[81] Asher Peres. Construction of unitary matrices from observable transition probabilities. *Nuclear Physics B-Proceedings Supplements*, 6:243–245, 1989. 95

[82] Simone Piacentini. Femtosecond laser writing of polarization insensitive photonic circuits for quantum optics and astrophotonics applications. 49

[83] Ioannis Pitsios, Leonardo Banchi, Adil S Rab, Marco Bentivegna, Debora Caprara, Andrea Crespi, Nicolò Spagnolo, Sougato Bose, Paolo Mataloni, Roberto Osellame, et al. Photonic simulation of entanglement growth and engineering after a spin chain quench. *Nature Communications*, 8(1):1569, 2017. 33

[84] JF Poyatos, J Ignacio Cirac, and Peter Zoller. Complete characterization of a quantum process: the two-bit quantum gate. *Physical Review Letters*, 78(2):390, 1997. 17

[85] Saleh Rahimi-Keshari, Artur Scherer, Ady Mann, Ali T Rezakhani, AI Lvovsky, and Barry C Sanders. Quantum process tomography with coherent states. *New Journal of Physics*, 13(1):013006, 2011. 93

[86] Saleh Rahimi-Keshari, Matthew A Broome, Robert Fickler, Alessandro Fedrizzi, Timothy C Ralph, and Andrew G White. Direct characterization of linear-optical networks. *Optics express*, 21(11):13450–13458, 2013. 18, 93, 95, 98, 105

[87] Robert Raussendorf and Hans Briegel. Computational model underlying the one-way quantum computer. *arXiv preprint quant-ph/0108067*, 2001. 8, 12

[88] Robert Raussendorf and Hans J. Briegel. A one-way quantum computer. *Phys. Rev. Lett.*, 86:5188–5191, May 2001. doi: 10.1103/PhysRevLett.86.5188. URL https://link.aps.org/doi/10.1103/PhysRevLett.86.5188. 8, 12

[89] Robert Raussendorf, Jim Harrington, and Kovid Goyal. A fault-tolerant one-way quantum computer. *Annals of physics*, 321(9):2242–2270, 2006. 9, 91

[90] Robert Raussendorf, Jim Harrington, and Kovid Goyal. Topological fault-tolerance in cluster state quantum computation. *New Journal of Physics*, 9(6):199, 2007. 10, 91

[91] Michael Reck, Anton Zeilinger, Herbert J Bernstein, and Philip Bertani. Experimental realization of any discrete unitary operator. *Physical review letters*, 73(1):58, 1994. 17, 39

[92] Sören Richter, Matthias Heinrich, Sven Döring, Andreas Tünnermann, Stefan Nolte, and Ulf Peschel.

Nanogratings in fused silica: Formation, control, and applications. *Journal of Laser Applications*, 24(4): 042008, 2012. 30

[93] Magali Rossi, Olivier Vidal, Bernd Wunder, and François Renard. Influence of time, temperature, confining pressure and fluid content on the experimental compaction of spherical grains. *Tectonophysics*, 441(1-4):47–65, 2007. 36

[94] Terry Rudolph. Why i am optimistic about the silicon-photonic route to quantum computing. *APL Photonics*, 2(3):030901, 2017. 91

[95] Linda Sansoni, Fabio Sciarrino, Giuseppe Vallone, Paolo Mataloni, Andrea Crespi, Roberta Ramponi, and Roberto Osellame. Two-particle bosonic-fermionic quantum walk via integrated photonics. *Physical review letters*, 108(1):010502, 2012. 41

[96] Dirk Schlingemann and Reinhard F Werner. Quantum error-correcting codes associated with graphs. *Physical Review A*, 65(1):012308, 2001. 9

[97] Pascale Senellart, Glenn Solomon, and Andrew White. High-performance semiconductor quantum-dot single-photon sources. *Nature nanotechnology*, 12 (11):1026, 2017. 56, 83, 92

[98] Lawrence Shah, Alan Y Arai, Shane M Eaton, and Peter R Herman. Waveguide writing in fused silica with a femtosecond fiber laser at 522 nm and 1 mhz repetition rate. *Optics express*, 13(6):1999–2006, 2005. 30

[99] Peter W Shor. Polynomial-time algorithms for prime factorization and discrete logarithms on a quantum computer. *SIAM review*, 41(2):303–332, 1999. 2

[100] Joshua W Silverstone, Raffaele Santagati, Damien Bonneau, Michael J Strain, Marc Sorel, Jeremy L O'Brien, and Mark G Thompson. Qubit entanglement between ring-resonator photon-pair sources on a silicon chip. *Nature communications*, 6:7948, 2015. 44

[101] AW Snyder and JD Love. Optical waveguide theory chapman and hall. *New York*, 1983. 33

[102] Nicolò Spagnolo, Chiara Vitelli, Lorenzo Aparo, Paolo Mataloni, Fabio Sciarrino, Andrea Crespi, Roberta Ramponi, and Roberto Osellame. Three-photon bosonic coalescence in an integrated tritter. *Nature communications*, 4:1606, 2013. 41

[103] Alexander M Streltsov and Nicholas F Borrelli. Fabrication and analysis of a directional coupler written in glass by nanojoule femtosecond laser pulses. *Optics Letters*, 26(1):42–43, 2001. 40

[104] Tetsufumi Tanamoto, Yu-xi Liu, Shinobu Fujita, Xuedong Hu, and Franco Nori. Producing cluster states in charge qubits and flux qubits. *Physical review letters*, 97(23):230501, 2006. 13

[105] Robert R Thomson, Henry T Bookey, Nicholas Psaila, Stuart Campbell, Derryck T Reid, Shaoxiong Shen, Animesh Jha, and Ajoy K Kar. Internal gain from an erbium-doped oxyfluoride-silicate glass waveguide fabricated using femtosecond waveguide inscription. *IEEE Photonics Technology Letters*, 18(14):1515–1517, 2006. 33

[106] Arthur Q Tool. Relaxation of stresses in annealing glass. *J. Res. Natl. Bur. Stand.(US)*, 34(2):199–211, 1945. 36

[107] Yoshiaki Tsujimoto, Motoki Tanaka, Nobuo Iwasaki, Rikizo Ikuta, Shigehito Miki, Taro Yamashita, Hirotaka Terai, Takashi Yamamoto, Masato Koashi, and Nobuyuki Imoto. High-fidelity entanglement swapping and generation of three-qubit ghz state using asynchronous telecom photon pair sources. *Scientific reports*, 8(1):1446, 2018. 24

[108] Michael Varnava, Daniel E Browne, and Terry Rudolph. Loss tolerance in one-way quantum computation via counterfactual error correction. *Physical review letters*, 97(12):120501, 2006. 8

[109] Michael Varnava, Daniel E Browne, and Terry Rudolph. How good must single photon sources and detectors be for efficient linear optical quantum computation? *Physical review letters*, 100(6):060502, 2008. iii, v, 24, 55

[110] Rebeca Martinez Vazquez, Roberto Osellame, Marina Cretich, Marcella Chiari, Chaitanya Dongre, Hugo JWM Hoekstra, Markus Pollnau, Hans van den Vlekkert, Roberta Ramponi, and Giulio Cerullo. Optical sensing in microfluidic lab-on-a-chip by femtosecond-laser-written waveguides. *Analytical and bioanalytical chemistry*, 393(4):1209, 2009. 26

[111] Werner Vogel. Glass chemistry, springer-verlag, 1994. 36

[112] Daniel F Walls and Gerard J Milburn. *Quantum optics*. Springer Science & Business Media, 2007. 14

[113] Philip Walther, Kevin J Resch, Terry Rudolph, Emmanuel Schenck, Harald Weinfurter, Vlatko Vedral, Markus Aspelmeyer, and Anton Zeilinger. Experimental one-way quantum computing. *Nature*, 434 (7030):169, 2005. 14

[114] Xi-Lin Wang, Luo-Kan Chen, Wei Li, H-L Huang, Chang Liu, Chao Chen, Y-H Luo, Z-E Su, Dian Wu, Z-D Li, et al. Experimental ten-photon entanglement. *Physical review letters*, 117(21):210502, 2016. 23

[115] Wataru Watanabe, Taishi Asano, Kazuhiro Yamada, Kazuyoshi Itoh, and Junji Nishii. Wavelength division with three-dimensional couplers fabricated by filamentation of femtosecond laser pulses. *Optics letters*, 28(24):2491–2493, 2003. 41

[116] Yaakov S Weinstein, C Stephen Hellberg, and Jeremy Levy. Quantum-dot cluster-state computing with encoded qubits. *Physical Review A*, 72(2):020304, 2005. 13

[117] Zheng-Yuan Xue and ZD Wang. Simple unconventional geometric scenario of one-way quantum computation with superconducting qubits inside a cavity. *Physical Review A*, 75(6):064303, 2007. 13

[118] DA Yashunin, Yu A Malkov, LA Mochalov, and AN Stepanov. Fabrication of microchannels in fused silica using femtosecond bessel beams. *Journal of Applied Physics*, 118(9):093106, 2015. 26

[119] Anton Zeilinger. General properties of lossless beam splitters in interferometry. *Am. J. Phys*, 49(9):882–883, 1981. 16

[120] Jonas Zeuner, Aditya N Sharma, Max Tillmann, René Heilmann, Markus Gräfe, Amir Moqanaki, Alexander Szameit, and Philip Walther. Integrated-optics heralded controlled-not gate for polarization-encoded qubits. *npj Quantum Information*, 4(1):13, 2018. 40